Novel Axisymmetric Diffusion Bonded Recuperator for Gas Turbines

by

Felipe Rodrigues de Castro

Mechanical engineer
Federal Center of Technological Education - MG, Brazil, 2013
M.S. Mechanical Engineering
Federal University of Santa Catarina, Brazil, 2018

SUBMITTED TO THE DEPARTMENT OF MECHANICAL ENGINEERING IN
PARTIAL FULFILLMENT OF THE REQUIREMENTS FOR THE DEGREE OF
DOCTOR OF PHILOSOPHY IN MECHANICAL ENGINEERING
AT THE
UNIVERSITÀ DEGLI STUDI DI GENOVA, ITALY
DECEMBER 2022

Author ....
Department of Mechanical Engineering
December 06, 2022

Certified by...
Pietro Zunino, PhD
Associate Professor of Mechanical Engineering - UNIGE
Thesis Supervisor

Certified by...
Dario Barsi, PhD
Associate Professor of Mechanical Engineering - UNIGE
Thesis Co-supervisor

Certified by...
Luis H. R. Cisterna, PhD
Associate Professor of Mechanical Engineering - University of Tarapacá (Chile)
Thesis Co-supervisor

Certified by...
Marcia B. H. Mantelli, PhD
Associate Professor of Mechanical Engineering – UFSC (Brazil)
Thesis Co-supervisor

Novel Axisymmetric Diffusion Bonded Recuperator for Gas Turbines

by

Felipe Rodrigues de Castro

Submitted to the Department of Mechanical Engineering
on Dec 06, 2022 in partial fulfillment of the
requirements for the degree of
Doctor of Philosophy in Mechanical Engineering

Abstract

The small gas turbines systems, arbitrary categorized as microturbines (5-200 kW) and miniturbines (200-500 kW) are the current most economical solution for the distributed power generation market. The thermal efficiency of such microturbines without and with a recuperator is about 20 and 40% respectively, thus a recuperator is mandatory to reach higher cycle efficiencies. However, the recuperator accounts for about 25-30% of the turbine total cost and its temperature and pressure are constrained depending on the material and construction method, being the bottleneck of the improvement and advancement of this kind of power generation plant. Thus, the actual focus is to develop high performance recuperators able to withstand high temperatures and pressure at minimum cost. There are several different recuperators present on the market, each with their own heat transfer surface and manufacturing method, but all present drawbacks and are relatively old compared to the actual manufacturing methods. For instance, the rectangular offset strip fin geometry, which is one of the highest performance surfaces, is expensive to manufacture and weak to withstand temperature and pressure due to brazing requirements. Hence, in this thesis, a completely novel modular axisymmetric recuperator concept is proposed, joined by diffusion bonding technique, one of the current most advanced heat exchanger manufacturing methods. For the recuperator core, a novel heat transfer surface is proposed based in the rectangular offset strip fins, the thermal and hydraulic characteristics of which were determined experimentally. The devised heat transfer and pressure drop correlations show 85% agreement with the experimental data in the range of 500<Re<3000. A code for the recuperator design, using entropy generation minimization, was developed to predict the recuperator performance and size the optimum recuperator core dimensions. The design code was validated with CFD which in turn was validated with experimental data. The heat transfer and pressure drop CFD results agreed the experimental data with deviation within 3.2% and 27.7%, respectively, and the design code agreed the CFD results with deviation within 0.9% and 11.9%, respectively. Four recuperator study cases for different turbine sizes, 100kW, 100kW_beta, 1250kW and 5000kW, were designed using the design code. The results show the proposed concept can achieve high effectiveness (~90%) with low pressure drop (<4%) with a volume compatible with the current recuperators. Furthermore, the novel recuperator concept has a list of advantages, which makes attractive its application on the future gas turbines, encouraging the research continuity of the proposed concept.

Thesis Supervisor: Pietro Zunino

Title: Associate Professor of Mechanical Engineering

Acknowledgments

Table of contents

List of figures

List of tables

1. Outline of thesis

The research is described in the next three chapters. In the next chapter, a complete experimental method to characterize unknown heat transfer surfaces for heat exchanger core application is described. In sequence, a novel heat transfer surface, based on the rectangular offset strip fins is proposed, where its thermal and friction characteristics are determined in terms of a heat transfer and pressure drop correlations. Finally, in the last chapter, a novel concept of recuperator for micro gas turbines is suggested using the novel heat transfer surface in its core. Four recuperators as study cases were designed, and their thermal and hydraulic performance were compared with the current recuperators in the market. The content of each chapter is summarized in sequence.

In Chapter 2 of the thesis, the thermal and friction characteristics of newly launched heat exchangers to be used in the market, must be acknowledged, usually by experimental methods. Steady-state Kays and London procedure is considered the classical experimental technique. In this setup, one of the heat exchanger streams is usually vapor, to provide controlled known heat transfer and temperature conditions, while the other stream is subjected to different flow rates, for the determination of the equipment thermal and pressure drop behaviors. Large expensive industrial boilers are usually used to provide steam, resulting in difficulties in stabilizing and controlling vapor temperatures. In the present work, a new experimental setup, based on the above-mentioned technique, is proposed for determining the heat transfer characteristics of compact heat exchangers. The boiler vapor flow is substituted by the working fluid (water in vapor state) of a two-phase thermosyphon. Being smaller and much more flexible, this technology allows for easy control of the vapor temperature, while providing uniform temperature distribution along one of the heat exchanger streams, which is difficult to obtain with the classical procedure. In the proposed apparatus, the "known side" of the heat exchanger takes the role of the condenser of the thermosyphon. Two well-known heat exchanger cores, composed of circular and square cross section channels, were used to validate the proposed arrangement, considering the ranges: 2200<Re<8000 and 850<Re<2800, respectively. The wall temperatures were tested in the range 120°C to 220°C with a precision of ±0.5°C in steady state. In addition, the resulting Nusselt number (Nu) and the Fanning friction factor (f) data were compared with consolidated literature correlations showing an average discrepancy of 15% for both geometries and parameters. Therefore, the use of thermosyphons results in smaller, simpler, and more precise test benches to be used for the evaluation of heat exchangers, as it provides the desired constant wall temperature conditions for the characterization of core geometries, substituting, with advantages, the use of large and expensive steam boilers.

Chapter 3 deals with one of the most common and efficient heat transfer geometries used in the core of plate fins compact heat exchanger (PFHE) which is the rectangular offset strip fins surface (rOSF). In this chapter, a novel and similar heat transfer geometry is proposed, the only difference is that the flow passages are circular instead of rectangular. An experimental study was conducted with five different exchanger cores containing the novel circular offset strip fins (cOSF) with variate dimensions (passage diameter, passage length and passage obstruction degree) for a Reynolds number range of 500-3000 under different core wall temperatures. The heat transfer experimental data was treated using the data reduction method of Kays and London for steady state steam-to-air technique to obtain the empirical Colburn j-factor characteristics. In addition, the empirical Fanning friction factor f was also assessed. The asymptotic behavior of both curves allowed to suggest rational design correlations of j and f in

terms of Reynolds and dimensionless geometric parameters δ and γ. The correlations for j and f factors can predict 90% of the experimental data within an error of ±15%. The combinations of these dimensionless numbers such as area goodness factor (j/f), volume goodness factor (j/f^1/3) and JF number related with the volume goodness factor are discussed in terms of overall performance criteria. The effects of the cOFS geometrical dimensions variation on the performance of heat transfer and pressure drop were also examined individually. The results shown an both similarity on both heat transfer and friction factor with the rOSF reference geometry.

In Chapter 4, to achieve high thermal efficiencies for gas turbines (up to 30%) a recuperator is mandatory. The actual recuperator represents a high percentage of the overall machine cost (25 – 30 percent), where the greater part of the actual recuperators is primarily of surface type, with their costs related mainly to its manufacturing complexity. To propose an alternative for the current fin-fold recuperators, the present study suggests a novel concept of wrap-around axisymmetric recuperator. The component is formed by modules manufactured by a stack of machined plates joined by diffusion bonding. The modules contain air and gas cells with circular offset strip fins (cOSF) heat transfer geometry in counter-flow configuration. A mathematical model to access the component thermal and hydraulic performance is proposed. In addition, using the mathematical model a recuperator design code was developed including the entropy generation minimization to design the "optimal" dimensional structure of the novel concept for four different turbine sizes (100kW, 100kW_beta, 1250kW and 5000kW). The design code was validated with a numerical study using the software Fluent, which in turn was calibrated with experimental data to provide reliable results. The CFD agreed with the experimental data with an average error of 27.7% for the pressure and 3.2% for heat transfer and the design code with the CFD with an average error of 11.9% for pressure drop and 0.9% for heat transfer. The results show the present recuperator concept can achieve high effectiveness $\left(\varepsilon \approx 0.9 \right)$ with contained pressure drop $\left(\Delta p_a \leq 1.5\% ; \Delta p_g \leq 4.0\% \right)$ at a volume similar to the current recuperators present in the market. Furthermore, several advantages associated to the novel recuperator concept encourage its development as; easy assembly, easy maintenance, no clogging, no need of manifold structure to distribute the flow, allow the use of bi-metallic approach, withstand high pressure ratio, thermal cycling resistant, compact volume, low pressure drop and high effectiveness, simplified manufacturing. Thus, the proposed alternative recuperator concept has great potential for use in the future microturbines.

2. Novel thermosyphon-assisted setup for determining heat exchanger thermal characteristics

Nomenclature

A	=	total heat transfer surface area, [m²]
A_{ff}	=	minimum free-flow area on the exchanger air side, [m²]
A_w	=	total wall area for transverse heat conduction, [m²]
C	=	flow stream heat capacity rate, [W/K]
c_p	=	specific heat of fluid at constant pressure, [J/kg]
D_h	=	hydraulic diameter of flow passages, [m]
D_{ext}	=	external diameter, [m]
D_{int}	=	internal diameter, [m]
D_s	=	square channel side length, [m]
d_{pi}	=	distance from the test section to the inlet pressure measurement plane, [m]
d_{po}	=	distance from the test section to the outlet pressure measurement plane, [m]
d_{Ti}	=	distance from the test section to the inlet temperature measurement plane, [m]
d_{To}	=	distance from the test section to the outlet temperature measurement plane, [m]
e	=	surface roughness size of the channel, [m]
f	=	Fanning friction factor, [dimensionless]
g	=	gravitational acceleration, [m²/s]
G	=	mass velocity based on the minimum free area, [kg/m²]
H	=	height of the frontal area of the heat exchanger core, [m]
h_{lv}	=	specific enthalpy of phase change, [J/kg]
h	=	heat transfer coefficient, [W/m²]
j	=	Colburn factor, [dimensionless]
k	=	fluid thermal conductivity, [W/m.K]
K_e	=	contraction loss coefficient for flow at heat exchanger entrance, [dimensionless]
K_c	=	expansion loss coefficient for flow at heat exchanger exit, [dimensionless]
L	=	heat exchanger core length, [m]
$L_{duct,i}$	=	air flow inlet duct length, [m]
$L_{duct,o}$	=	air flow outlet duct length, [m]
l_y	=	vertical distances between centers of the adjacent channels, [m]
l_z	=	horizontal distances between centers of the adjacent channels, [m]
$\dot{m}_a$	=	air mass flow rate, [kg/s]
n°_{ch}	=	number of channels in the heat exchanger core, [dimensionless]
n°_{col}	=	number of channel columns in the heat exchanger core, [dimensionless]
n°_{lin}	=	number of channel lines in the heat exchanger core, [dimensionless]
Nu_D	=	Nusselt number based on the hydraulic diameter, [dimensionless]
$Nu_{\sqrt{A}}$	=	Nusselt number based on the area square root, [dimensionless]
NTU	=	number of exchanger heat transfer units, [dimensionless]
P	=	wetted perimeter of exchanger passages on the air side, [m]
$p_{a,i}$	=	air pressure at the inlet test section, [Pa]

$P_{a,o}$	=	air pressure at the outlet test section, [Pa]
Pr	=	Prandtl number, [dimensionless]
Δp	=	differential pressure between the test section inlet and outlet, [Pa]
q	=	heat transfer rate, [W]
q''	=	heat flux, [W/m²]
r_h	=	hydraulic radius, [m]
$\tilde{R}$	=	gas constant, [J/kg.K]
R_a	=	air side convection thermal resistance, [W/K]
$R_{c,eq}$	=	thermosyphon condenser equivalent thermal resistance, [W/K]
R_v	=	vapor side thermal resistance, [W/K]
R_w	=	wall conduction thermal resistance, [W/K]
Re_D	=	Reynolds Number based on the hydraulic diameter, [dimensionless]
Re_f	=	Reynolds number based on the condensation film, [dimensioless]
$Re_{\sqrt{A}}$	=	Reynolds number based on the area square root, [dimensioless]
R_1	=	thermal conduction resistance of the thermosyphon evaporator wall, [W/K]
R_2	=	simplified nucleate poll boiling thermal resistance, [W/K]
s_{duct}	=	duct internal side length, [m]
$T_{a,i}$	=	air flow temperature at the test section inlet, [°C]
$T_{a,lm}$	=	air flow log-mean temperature, [°C]
$T_{a,o}$	=	air flow temperature at the test section outlet, [°C]
T_{ad}	=	temperature at the adiabatic section of the thermosyphon, [°C]
T_e	=	temperature at the evaporator of the thermosyphon, [°C]
T_m	=	fluid bulk mean temperature, [°C]
T_t	=	temperature at the top of the thermosyphon, [°C]
T_v	=	thermosyphon vapor temperature, [°C]
T_w	=	temperature at the thermosyphon condenser walls (core wall temperature), [°C]
ΔT_{in}	=	local temperature difference between the air inlet and the core walls, [°C]
ΔT_{lm}	=	log-mean temperature difference, [°C]
ΔT_{out}	=	local temperature difference between the air outlet and the core walls, [°C]
U	=	overall heat transfer coefficient, [W/m²]
δ_w	=	wall thickness, [m]
ε	=	channel aspect ratio, [dimensionless]
η_0	=	extended surface efficiency on one fluid side, [dimensionless]
μ	=	fluid dynamic viscosity, [Pa . s]
ρ	=	fluid density, [kg/m³]
σ	=	ratio of free flow area to frontal area, [dimensionless]
Subscripts		
a	=	air side
avg	=	average
cp	=	constant properties
i	=	inlet
l	=	liquid phase
L	=	laminar
m	=	mean
max	=	maximum

min	=	minimum
o	=	outlet
TR	=	turbulent rough
TS	=	turbulent smooth
tur	=	turbulent
v	=	vapor side
w	=	wall

2.1 Introduction and literature review

Although being considered well known components for many applications in the industry, the heat exchangers are still the subject of research studies around the world, usually with the objective of enhancing their heat transfer capacity, while keeping the pressure drops at the lowest levels possible. The evolution of the manufacturing process and the use of advanced materials enabled the creation of heat exchangers with new fluid flow channel geometries, improving compactness and the heat transfer capacity, with controlled pressure drops.

To assess the potential of new complex core geometries, models and correlations for the heat transfer and pressure drop are required, usually given in terms of the following dimensionless parameters: Colburn factor (j), Nusselt number (Nu), Fanning friction factor (f) and Reynolds number (Re_D). For flows with intricate channel geometries, analytical modeling becomes impractical, while computer simulation results are suspicious due to the high level of turbulence that are usually associated with them [1]. Therefore, the experimental evaluation of thermal and friction performances of devices with complex flows is still the most reliable way to characterize new core geometries for heat exchangers.

In some cases, the determination of accurate heat transfer coefficients using experimental facilities may not be straightforward and requires some special techniques. The literature presents several experimental methodologies that include setup and data reduction methods, which choice depends on the fluid heat capacities and on the test setup constraints. Three of the most used techniques are briefly discussed in sequence.

The first technique is the Wilson plot [2] and its modifications [3], generally applied when the heat transfer coefficients must be determined for both streams. This method, based on energy balance and statistical data treatment, appears to be very useful when the heat transfer correlations for both flows in a heat exchanger are unknown, or when the thermal resistance for both fluids are of the same order of magnitude [4]. Several works [5] – [7] apply this technique, which, although very used, can be quite complex and uncertain, as the results depend on the statistical models used, so that different outcomes can be obtained by these methods [8] – [9].

The second is the transient test technique [10], which can be considered relatively simple in terms of experiment complexity. Also known as single-blow transient testing technique [10], its utilization is indicated to characterize the heat transfer coefficient of flows in matrix type or high-NTU heat exchangers. In this case, a fluid stream (generally air) flows steadily through the core to be tested. Initially, both stream and core walls are at the same constant and uniform temperature. Then, a transient perturbation on the inlet fluid temperature is induced in this flow and the outlet temperature is continuously recorded. The resulting transient data is then compared with a theoretical model and the corresponding heat transfer coefficient between the test core and the fluid is obtained. Although simple, the single-blow transient technique requires more assumptions than the other techniques and its accuracy is very

dependent upon how accurately the mathematical model describes the experiment [11]. Experimental and numerical evaluations of the channel characteristics, using this technique, are available mainly for very complex geometry channels, such as those found in non-uniform porous media [11] – [12].

Finally, the third, and probably the most accurate technique, was proposed by Kays and London [13] and can be employed for determining the Colburn factor (j), as a function of the Reynolds number (Re_D) of one side of the heat exchanger. A crossflow heat exchanger, in steady state conditions, is usually employed as the test section, for which a stream, from one side, has known fluid flow conditions and, another stream, in the other side, has the parameters to be determined. The idea behind the procedure is to provide, on the known side, a stream that promotes uniform wall temperatures, with high heat capacity. This condition can be achieved by the combination of large heat transfer areas with high coefficients of heat transfer, this last obtained by high mass flow rates or by using fluids with: high specific heats or undergoing phase-change. On the "unknown" side of the exchanger, a controlled mass flow rate of the fluid under investigation is forced (or induced) through the channel to be characterized. The inlet and outlet flow temperatures, the wall temperatures, as well as the inlet and outlet static pressures are monitored during the test. The resulting experimental data are treated using a simplified mathematical model, which usually neglects the thermal resistance associated with the known side, removing it from the overall thermal circuit, as it can be orders of magnitude lower than the other resistances. This approach is commonly used in numerical studies, in which constant wall temperature is set as boundary conditions [14] – [15]. Actually, most of the literature studies regarding the heat transfer coefficients for plate-fin (PFHE) and print circuit heat exchangers (PCHE) are based on this procedure [16] – [18].

A schematic illustration of the steam-to-air steady-state heat transfer test rig used by Kays and London [13] is shown in Figure 2.1. The air mass flow rate, temperatures and pressures are measured along the air duct, before and after the test section, as indicated. The known side of the test section is major constraint of this facility, from an experimental point of view (dashed red line region). Normally, saturated steam is used, generally supplied by large boilers or similar devices in which the fine control of temperature distributions and/or levels, are difficult, especially due the pressure limitations of the test ducts. Moreover, the steam flow requires piping and valves making the assembly complex and expensive.
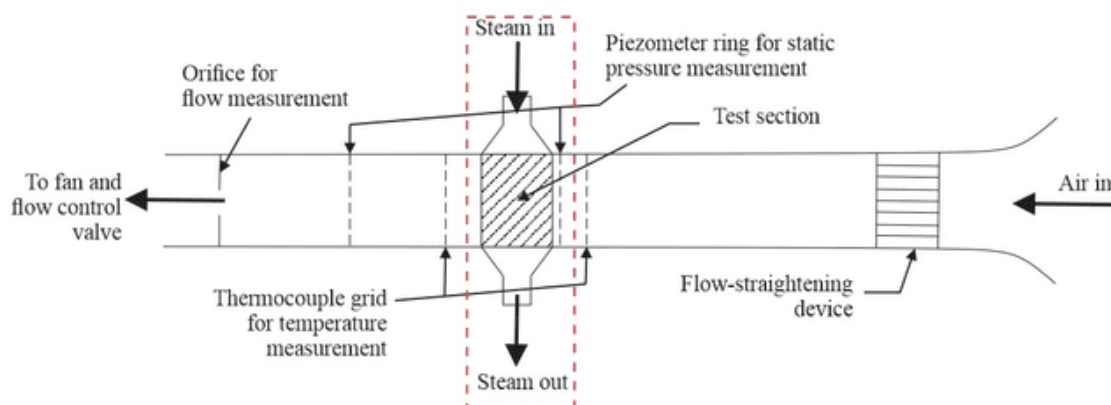
Figure 2.1 - Schematic of a steam-to-air steady-state heat transfer test rig. (Adapted from Shah, [1])

Two-phase thermosyphons [19] are simple and effective heat transfer devices, basically composed of a hermetically closed casing partially filled with a controlled volume of a working fluid. The device can be divided into three distinct regions: evaporator, adiabatic section and condenser. The heat supplied to the evaporator, necessarily located at a lower height in

reference to the other sections, evaporates the working fluid accumulated in this region. The saturated vapor, due to pressure differences, flows to the condenser direction, where heat is transferred to the condenser walls, causing the vapor condensation. The condensate is pushed back to the evaporator by gravity. Therefore, liquid-vapor latent heat absorbed in the evaporator is released in the condenser by vapor-liquid phase change. Actually, the phase change phenomena in the condenser provides conditions of close to uniform temperature distribution along the condenser walls. This condition will be further discussed in Section 2.4.

Actually, two-phase thermosyphons are being used in heat exchangers for many applications, due to their characteristic of effectively transfer the heat from the hot to the cold sources [20-25]. However, it is not available in the literature an application of two-phase thermosyphons the main purpose of which is to provide constant temperature condition on one side of the heat exchanger. This work suggests the introduction of the test core into the condenser section of a two-phase thermosyphon, which actually substitutes all the apparatuses necessary to generate steam, by a simple evacuated tube with working fluid (water) inside. Besides, this setup allows fine temperature tuning over the condenser walls, by controlling the heat source power input in the evaporator section. The dispositive can work at basically any temperature, as different working fluids can be used, depending on the desired temperature levels. Also, the phase change is a very heat intensive phenomenon, so that the device can be quite small, resulting in a test apparatus with the overall dimensions significantly reduced, with consequent reduction of costs.

Besides the heat transfer characteristics, the pressure drop, especially in compact heat exchangers is important to be depicted, using well-known procedures. In this work, the dimensionless Fanning friction factor is determined using straightforward methods under steady fluid flow rates. The technique used to determine these factors can be considered independent of the heat transfer rate and of the heat exchanger geometry. Therefore, no improvement related to the friction factor heat exchanger core characterization is proposed.

Data from compact heat exchangers with well-known square and circular cross section channels are used to validate the proposed heat transfer characterization methodology, by comparing results with literature correlations.

It should be highlighted that the use of vapor, delivered by a thermosyphon, to promote the constant wall temperature for the heat transfer characterization of compact heat exchangers, is actually the major contribution of this work. The apparatus setup here proposed, which is simple, low cost and precise, takes advantage of the large experience that the author's research group has in the development of thermosyphon equipment for the industry. The authors are not aware of any similar device reported in the literature.

2.2 Test setup and experimental procedure

In this work, an experimental setup is proposed for precise measurement of the heat transfer and pressure drop characteristics of streams in unknown heat exchanger core geometries. In the experiment, one compact heat exchanger side is subjected to a vapor flow, working as a condenser of a closed two-phase thermosyphon, while the other is subjected to the stream to be characterized. Due to the saturated vapor to liquid phase change, very uniform wall conditions (constant wall temperature) can be obtained. Basically, any heat power input can be achieved by controlling the power supplied to the evaporator, at any temperature level, which depends on the working fluid.

To validate the experimental setup, typical core geometries, with square and round cross section channels, were tested in a vapor-to-air compact heat exchanger experiment, in steady

state regime. The Nusselt number and Fanning friction factor data for different flow regimes are compared with consolidated correlations available in the literature.

2.2.1 Experimental facility

The present workbench was designed to reproduce the steady state steam-to-air Kays and London Technique [1], which uses, at a known side, the high heat capacity inertia of a stream to keep constant the heat exchanger core wall temperatures. In the other side of the core, a lower heat capacity fluid, generally air, is forced through the channels, the heat transfer of which characteristic streams are to be determined, at different flow regimes. As for the present work, these authors also used steam in the known side due to its high heat capacity rate, in order to keep the wall temperature constant. As mentioned, in the present test setup, saturated water vapor from a two-phase thermosyphon, for which condenser plays the role of the known side of the heat exchanger core, is used, with air stream on the unknown side.

The experimental facility is shown in Figures 2.1 and 2.3. Starting from the left-hand side of Figure 2.2, a centrifugal fan, with power controlled by a frequency inverter, is used to provide the airflow at different constant mass flow rates. In sequence, an adjustable electric heater is used to increase the air temperature to pre-established temperature levels $T_{a,i}$, defined as standard for all tests. A flexible hose, used to eliminate the fan vibration, connects the heated airflow to a Coriolis mass-flow meter, where the mass-flow readings $\dot{m}_a$ are recorded by a data acquisition system. After the Coriolis, the air flows through a square cross section inlet duct of edge S_{duct} and length $L_{duct,i}$, within which the air flow fully develops before it reaches the test section. After the passage through the test section, an outlet duct with the same internal cross-section dimensions S_{duct} but with another length $L_{duct,o}$ is used to drive the air flow to the ambient. The pressures $p_{a,i}$ and Δp_a are measured by means of an absolute and a differential pressure transducer respectively, installed at pressure taps, located at distances d_{pi} and d_{po}, before and after the test section, respectively (see Figure 2.2). The temperatures $T_{a,i}$ and $T_{a,o}$ are the average temperature readings, measured by four thermocouples type K, each, at distances of d_{Ti} from the inlet and d_{To} from the outlet faces of the test section (Figure 2.2). In the flow direction, the thermocouples are positioned always after the pressure taps, to not create pressure perturbations. The test facility is well thermally insulated with a ceramic fiber blanket. The important dimensions, instruments characteristics and components are described in Table 2.1. In Figure 2.2, a photography of the experimental setup, without the thermal insulations, is presented.
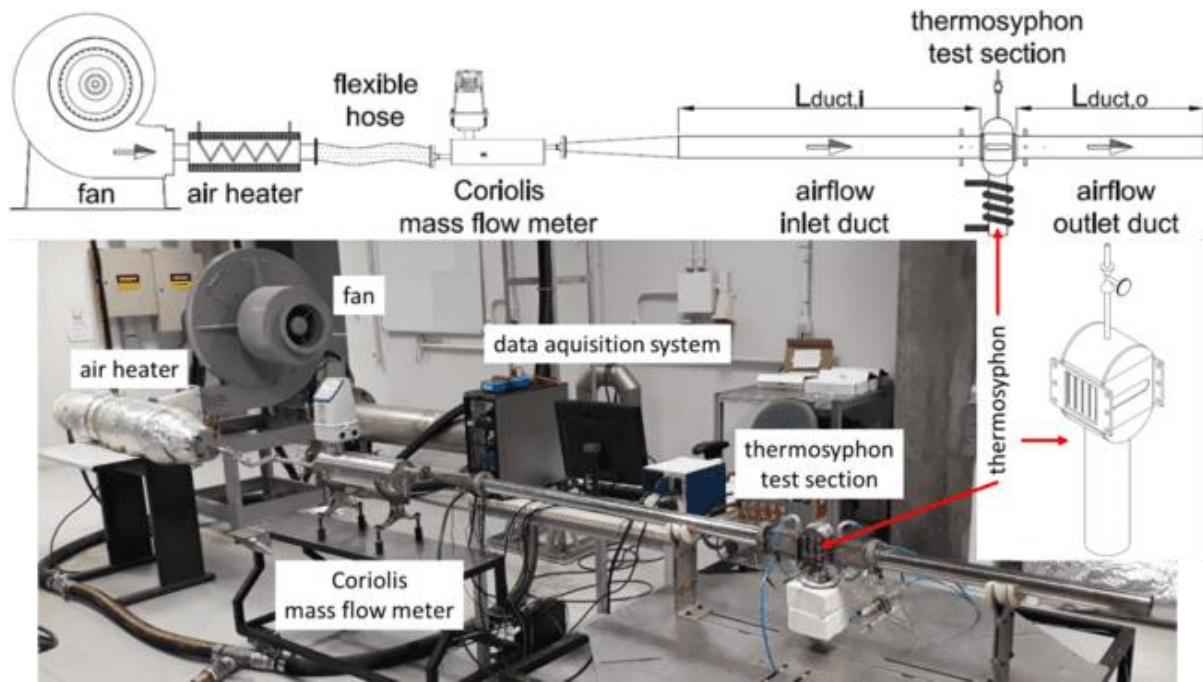
Figure 2.2 - Schematic (above) and picture (bottom) of the steam-to-air steady-state heat transfer test rig.

The thermosyphon, shown in Figure 2.2, is coupled to the ducts by flanges and is sealed by a Polytetrafluoroethylene (PTFE) joint. Figure 2.3 shows details of the test section assembly within the test rig. Heat is provided by an independent controllable electric resistance, called heat supply, to the evaporator of the thermosyphon, located bellow the test section (actually the condenser of the thermosyphon). Fourteen thermocouples are positioned in the thermosyphon walls, monitoring their temperatures, according to the scheme in Figure 2.3a: two in the top of the condenser section T_t, six in the condenser walls T_w (Figure 2.3a shows the side view, where only three thermocouples can be seen), two in the adiabatic section T_{ad} and four at the evaporator T_e. Basically, any heat exchanger geometry can be tested with this technique, with the proper design of the thermosyphon condenser. A photograph of the thermosyphon, without the thermal insulations, is presented (see Figure 2.3b) to illustrate the test section assembled in the experimental setup, with its main dimensions in millimeters present in the side draw.
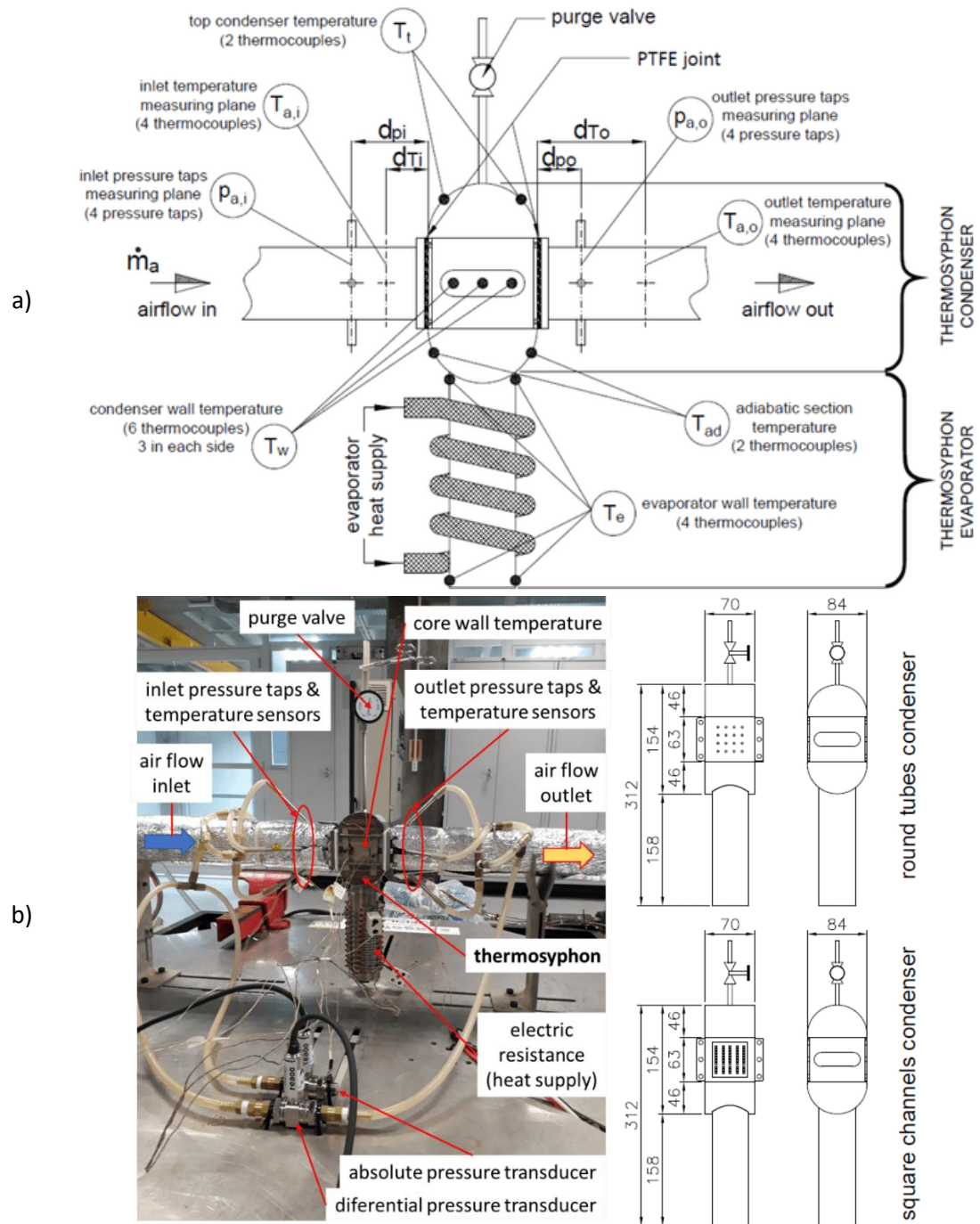
Figure 2.3 – Thermosyphon test section experiment; assembly and measuring points.

Table 2.1 - Experimental facility main dimensions and instruments.

	$L_{duct,i}$	$L_{duct,o}$	d_{pi}	d_{Ti}	d_{po}	d_{To}	S_{duct}
Dimensions [mm]	800	500	50	23.5	25	75	50
Centrifugal fan	SolerPalau RR710						
Electric air heater	5000 W						
Coriolis mass flow meter	Siemens - Sitrans FC mass 2100/6000						
Pressure transducer	Omega – PX409 series						
Data aquisition system	NI SCXI-1000						
Thermosyphon test section	stainless steel 316L						

In the present work, two heat exchangers, with channels with different geometries were evaluated: the square cross section channel and round tubes. In the first, an air stream was forced through a compact heat exchanger with in-line parallel square channels, the details of which are shown in Figure 2.4. The channels were formed by a "sandwich" of plates joined by diffusion bonding, for which the extremities were blind plates "pl" and the fill is formed by a plate with machined channels in comb shape, the comb plate "cb" (sequence is indicated as "pl", "cb" and "pl" in detail 3 in Figure 2.4). Two thicker spacers, named as "sp" were placed in sequence to form a gap for the vapor passage. In the same figure, l_y and l_z are the vertical and horizontal distances between centers of the adjacent square channels, respectively, while D_s is the square channel side length. The condenser tested had five "sandwiches" of plates in columns, each sandwich containing 10 channels. The column height is indicated by H, while the channel length by L. The core was closed with two seal plates, named as "sl", one in each side of the thermosyphon condenser. The thermocouples were installed over the external face of both seal plates "sl", in slots (see detail 2 in Figure 2.4) made to adjust the thicknesses of these plates to the same thicknesses of the blind plates "pl". As the vapor that comes from the thermosyphon evaporator keeps all surfaces at the same thermal conditions, these wall temperature readings would be very close to those over which the air flows within the channels.

A schematic of the expected fluid temperature distribution in the first heat exchanger core, for both fluid sides, is shown in the graph located on the upper-left of the same of Figure 2.4 (detail 4), with ΔT_{in} and ΔT_{out} calculated as $\Delta T_{in} = T_w - T_{a,i}$ and $\Delta T_{out} = T_w - T_{a,o}$ considering that the walls are at higher temperatures than the fluid. The condenser wall temperature is considered uniform, corresponding to the average of the six condenser side wall thermocouples readings T_w. In this plot, $x = 0$ represents the position in which the air flow enters the test section, with channels of length L. The arrows toward the evaporator section illustrate the heat flux provided by the electric resistance to the thermosyphon (detail 1 in Figure 2.4).
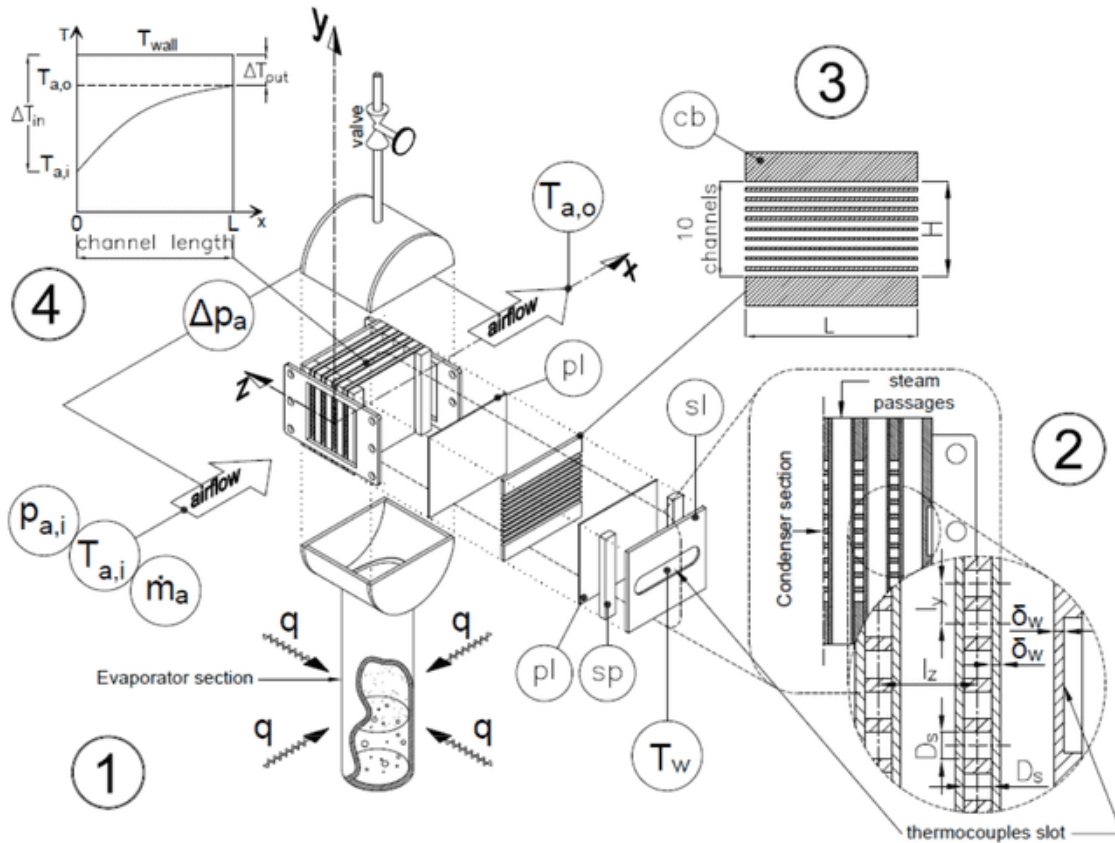
Figure 2.4 - Thermosyphon test section with an in-line square channels bank heat exchanger core inserted in its condenser section.

The second heat exchanger core geometry tested consisted of a bank of in-line tubes. The thermosyphon test section has the same dimensions of the square channels, with the condenser rearranged to accommodate the round tubes array, as observed in Figure 2.5. The vertical and horizontal distances l_y and l_z of the tube rows and columns are indicated in the shown zoom view (detail 1 in Figure 2.5). Slots on the lateral seal plates ("sl") where the thermocouples were installed were also milled, to approach their thickness to the round tube walls thickness (δ_w), for the same reason as explained for the square channel core, in order to guarantee similar conduction thermal resistances. The tubes inner (D_{int}) and external (D_{ext}) diameters are also indicated in the figure. Detail 2 of the schematic plot of Figure 2.5, shows the fluid temperature distribution in the core for both fluids, with an analogous behavior to that expected for the square channel test section. The main dimensions of the test section and the setup are presented in Table 2.2.
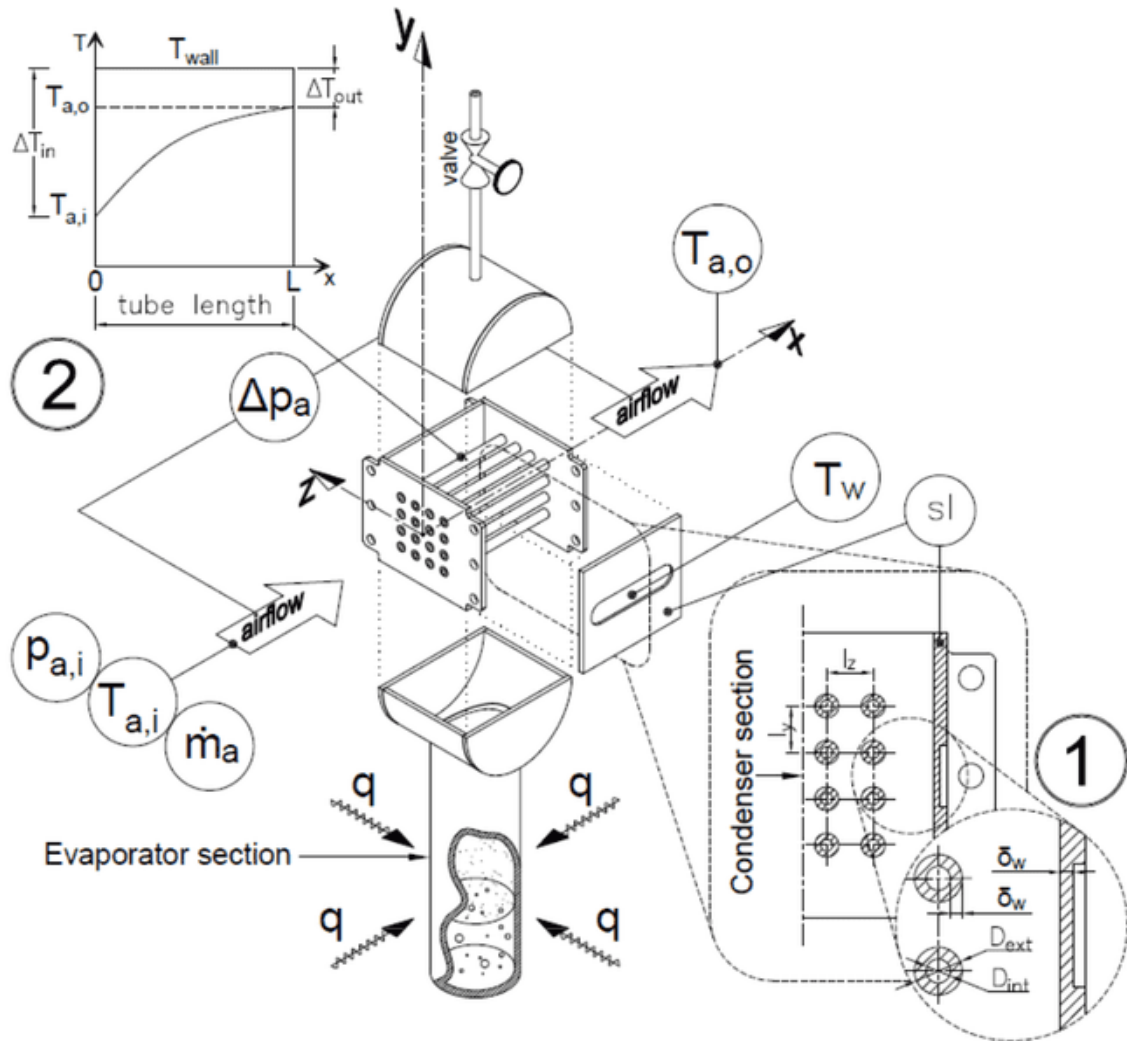
Figure 2.5 – Thermosyphon test section with an in-line tubes bank heat exchanger core inserted in its condenser section.

Table 2.2 – Heat exchanger core main dimensions.

Dimensions in [mm]	D_{int}	D_{ext}	D_s	l_y	l_z	δ_w	L	$\overset{\circ}{n}_{ch}$	$\overset{\circ}{n}_{col}$	$\overset{\circ}{n}_{lin}$
Square channels	-	-	3	4.5	6.35	1	78	50	5	10
Round tubes	2.8	5.8	-	11.4	11.4	1.5	84	16	4	4

The thermosyphon working fluid used was distilled water with a filling ratio of 90%, defined as the ratio between the working fluid and the total evaporator volumes. This filling ratio was selected in order to guarantee the evaporator walls were always wetted by the working fluid, allowing high heat flux over the section walls without creation of hot spots. The evaporator was manufactured from a 316L stainless steel tube, with outer diameter, wall thickness and total length of 50.8, 3 and 158 mm, respectively. The thermosyphon charging procedures were carried out according to the methodology proposed by Mantelli [19].

In order to guarantee the pure vapor conditions inside of the thermosyphon, a purge procedure was adopted just before the tests. For that, the thermosyphon was heated until the vapor pressure became superior the atmosphere pressure. At this point, the valve positioned on the top of the thermosyphon was opened during a short period until water vapor was visually released to the atmosphere. The vapor, before escaping, sweeps out the non-condensable

gases, naturally accumulated at the upper regions of the thermosyphon, where the valve is located. This procedure, which must be quick to avoid considerable working fluid losses, guarantees that only working fluid (water in this case) remains inside the device, which affects directly the thermosyphon operating temperature level and distribution. An analysis of the purge procedure is presented in the Results section. It is important to note that purging to atmosphere is doable only for non-toxic working fluids, such as water.

2.2.2 Experimental methodology

Experimental tests were performed following the procedure here described. First, the airflow rate and its inlet temperature are set at a predetermined (calibrated) value. At the same time, the evaporator heat supply is adjusted to the power level in which the wall of the thermosyphon condenser reaches the desired value. The steady-state conditions are then established, characterized when the air flow temperature upstream and downstream of the test section reach constant values and the condenser wall temperature is stabilized. In this work, the steady state condition was assumed when during a period of 10 minutes the temperature average difference was less than 1%. After that, the data acquisition is started, and data is recorded during a pre-determined period of time (5 minutes). Simultaneously, the mass flow rate, as well as the upstream absolute pressure and the pressure drop across the core of the unknown side is recorded to determine the hot friction factors. The tests are repeated at different air flow rates at the unknown side, to cover the desired range of Reynolds number. At each different mass flow rate, a steady state was expected to be reached before starting a new test.

The test matrix adopted in the present work is shown in Table 2.3. Each heat exchanger configuration was tested at each condenser wall temperature, while the mass flow rate, always set at a constant temperature of 65°C, was tuned on at each constant predetermined level, from the lower to the higher values. The experimental test parameters were defined taking into account the fan capacity and the mass flow range that the Coriolis was able to measure. The core wall temperatures were established in different levels, to evaluate the thermosyphon capacity to provide stable data. Furthermore, the minimum wall temperature of 120°C were selected to guarantee a large difference from the air flow temperature, assuring the outlet air temperature would not reach values close to the wall temperature, reducing errors in the NTU determination (Eq. 4). The maximum thermosyphon temperature of 220°C was limited by safety due the water vapor pressure, which, at 220°C, corresponds to approximately 23 bar.

Table 2.3 - Experimental test parameters matrix.

Condenser wall temperature		Air inlet temperature	Air mass flow rate [kg/min]
Square channels	Round tubes		
			0.10
120 °C	150 °C		0.15
			0.20
			0.25
150 °C	170°C	65°C	0.30
			0.35
180 °C	220°C		0.40
			0.45

The experimental uncertainty analysis was performed considering the following sources of error; uncertainties of the test core dimension, instrument uncertainties, temperature and mass flow rate random fluctuations and the fluid properties variations due to temperature dependency. The uncertainties methodology used is present in [26]. The uncertainties of the

vapor-to-air test results vary somewhat with the core dimensions, air mass flow rate and temperature tested. A conservative analysis was made to encompass all tests done. The assumed uncertainties are shown in Table 2.4.

Table 2.4 - Experimental uncertainties.

	Average uncertainties
Temperature	±0.6%
Pressure	±5.4%
Mass flow rate	±0.2%
Reynolds number	±0.2%
Nusselt number	±6.5%
friction factor	±5.2%
Thermal resistance	±31%

2.3 Data treatment

To design a heat exchanger, it is necessary to know the thermal and pressure drop characteristics associated with both streams of the equipment. These parameters are generally presented in terms of Nusselt numbers, Fanning friction factors and flow Reynolds numbers. This section presents the data reduction method used to obtain these dimensionless parameters from experimental results. A temperature-dependent fluid properties correction is also necessary, due to the high temperature difference between the fluid and the exchanger walls. Finally, some literature correlations for Nusselt number and Fanning friction factor for square channels and round tubes in laminar, transition and turbulent regimes are presented.

2.3.1 Reynolds number

Most of the available correlations concerning heat transfer and pressure drops are functions of Reynolds numbers based on the hydraulic diameter of the respective flow passage, i.e.:

$$\mathrm{Re}_D = \frac{G_a D_{h,a}}{\mu_a} \tag{1}$$

where μ_a is the air dynamic viscosity, $G_a = \left(\dot{m}/A_{ff}\right)_a$ is the mass velocity and $D_h = 4\,A_{ff}\big/n^{\circ}_{ch}\big/P$ is the hydraulic diameter. Besides, $\dot{m}$ is the mass flow rate, where n°_{ch} is the number of channels in the air-side, P is the wet perimeter of one individual channel, $A_{ff} = n^{\circ}_{ch} D_s^2$ is the free flow cross-section area for the square cross section channels and $A_{ff} = n^{\circ}_{ch}\,\pi D_{\mathrm{int}}^2\big/4$ for the round tubes. In this work, all the physical properties appearing in the Reynolds number and other dimensionless parameters are evaluated at the log-mean average temperature, as defined in the sequence.

2.3.2 Nusselt number

The data reduction method here described is based on the steam-to-air steady state Kays and London technique [1]. All the fluid properties (cp, μ, Pr, ρ), on the air side, are evaluated at the log-mean average temperature given by,

$$T_{a,lm} = T_w - \Delta T_{lm} \tag{2}$$

where,

$$\Delta T_{lm} = \frac{\left(\Delta T_{in} - \Delta T_{out}\right)}{\ln\left[\left(\Delta T_{in}\right)/\left(\Delta T_{out}\right)\right]} \tag{3}$$

As already observed, one of the sides of the heat exchanger is actually the thermosyphon's condenser, where vapor is condensed, providing a uniform and controlled wall temperature boundary condition for the other stream, the air in this case. The thermal resistance of the air (convection in gas) is some orders of magnitudes larger than the vapor-liquid phase change resistance. These temperature boundary condition and the air and vapor side thermal resistances are discussed on Section 2.4.1 and 2.4.3, respectively. Therefore, the air represents the controlling thermal resistance, as it has the lower minimum heat capacity from both sides, $C_{\min} = C_a = \left(\dot{m}c_p\right)_a$. Neglecting the vapor heat capacity, $C_{\min}/C_{\max} = 0$, an energy balance at a control volume on the air side results in:

$$\frac{\Delta T_{out}}{\Delta T_{in}} = \frac{T_w - T_{a,o}}{T_w - T_{a,i}} = e^{-NTU} \tag{4}$$

where NTU is the number of transfer units, defined as a ratio between the overall thermal conductance and the smaller heat capacity rate [13]:

$$NTU = \frac{UA}{C_{\min}} = \frac{1}{C_{\min}} \int_A U \, dA \tag{5}$$

For steady state conditions, the local overall heat transfer coefficient U can be considered constant. The thermosyphon test section can be modeled as a thermal circuit, formed by several thermal resistances in series or in parallel, depending on the thermosyphon arrangement [19]. Figure 2.6 presents schematics of the thermosyphon thermal circuits for both heat exchanger cores (square channels and round tubes cross sections). As the square channel condenser is formed by five plate sandwiches formed by "pl" and "cb" plates, the thermal resistances arrangement is formed by five parallel resistances. The vapor actually spreads into the vapor passages columns of the condenser, independently of the air-side conditions. In the case of the round tube core, only one thermal resistance is considered for the vapor flow, as it condenses externally over the tube bank. Each tube was considered not influenced by the neighbors' tubes, as the distances between them are sufficiently large. In this figure 2.6, R_1 and R_2 represent the heat conduction resistance through the evaporator wall and the simplified nucleate pool boiling thermal resistances, respectively. In the present study, these resistances, which are predicted using literature correlations, are not investigated, once the focus is on the compact heat exchanger core, placed on the condenser section. In addition, it is important to mention that the temperature reading at the adiabatic section T_{ad} is close to the thermosyphon vapor temperature T_v, i.e. $T_{ab} \cong T_v$ [19].

The thermal circuit of the condenser is considered composed of three components: (1) air-side thermal resistance R_a, (2) wall thermal resistance R_w, and the (3) vapor-side thermal resistance R_v, so that:

$$\frac{1}{UA} = R_a + R_w + R_v \tag{6}$$

where the vapor-side thermal resistance R_v is determined by:

$$R_v = \frac{1}{A_v h_v} \tag{7}$$

Figure 2.6 – Thermosyphon test section thermal circuit.

where, A_v is the total area where the condensation occurs. For the square channels core $A_v = 2n_{col}HL$ (with n_{col} as the number of columns) and for the round tubes array $A_v = n_{ch}^{\circ}\pi D_{ext}L$ (with n_{ch}° the total number of tubes). In the vapor-side, h_v is the heat transfer coefficient of the film condensation, which can be computed using the two correlations presented in Table 2.5.

Table 2.5 – Vapor side heat transfer correlations.

Ref.	Surface	Fluid	Equation	
Groll and Rösler [27]	Condensation on vertical flat plates	General.	$h_v = 0,63\left(\dfrac{\rho_l^2 g h_{lv}' k_l^3}{\mu_l H}\right)^{1/3} q''^{-1/3}$	(8)

			$h_v = 25\dfrac{k_l}{D_{ext}}\Pr_l^{0,4}\operatorname{Re}^{0,25}$	
Kaminaga et al. [28]	Condensation over horizontal round cylinders bank	General.	$\operatorname{Re}_f = \dfrac{4q}{\pi D_{ext}\mu_l h_{lv}}$	(9)

where, ρ_l is the liquid phase density, g is the gravity, h_{lv} is the specific enthalpy of phase change, k_l is the liquid-phase thermal conductivity, μ_l is the liquid-phase dynamic viscosity, q is the heat transfer rate, q'' is the heat flux on the condenser walls, $\Pr_l$ is the dimensionless Prandlt number for the working fluid in the liquid phase, Re_f is the dimensionless Reynolds number based on the film, H is the column height for the square channels core (Eq. 8) and D_{ext} is the diameter of the round tubes array (Eq. 9).

In the present case, the first correlation, Eq. (8), proposed by Groll and Rosler [27], was used to model the film condensation over vertical flat plates of the square channels inside of the thermosyphon condenser, since this correlation is based on the flat plate Nusselt condensation model. The second correlation, Eq. (9), proposed, by Kaminaga et al. [28], was applied for the external horizontal round tube area. According to Mantelli [19], the correlation of Kaminaga et al. [28] is recommended when it is not possible to recognize the liquid film flow regime within the thermosyphon, as is the present case. These correlations are suitable for the one-specie condensation in a pure vapor atmosphere and were developed specifically to predict the condensing heat transfer coefficient in two-phase thermosyphons [19].

Back to Eq. (6), the second right hand side thermal resistance R_w refers to the heat conduction through the heat exchanger core walls. The heat conduction resistance through a flat plane and a cylindrical tube are given by the well-known expressions, respectively:

$$R_w = \frac{\delta_w}{2k_w HL} \tag{10}$$

$$R_w = \frac{\ln\left(D_{ext}/D_{int}\right)}{2\pi k_w L} \tag{11}$$

The equivalent thermal circuit for the condenser section is composed by the resistances R_v and R_w as:

$$R_{c,eq} = R_v + R_w = \frac{T_v - T_w}{q} \tag{12}$$

where T_v and T_w are, respectively, the vapor and the condenser wall temperatures, measured experimentally, as described in Section 2.2. The heat transfer rate (q) transported by the thermosyphon, is quantified experimentally by the sensible heat increase of the air passing through the exchanger, by:

$$q = \left(\dot{m}c_p\right)_a \left(T_{a,i} - T_{a,o}\right) \tag{13}$$

Finally, the last term of the Eq. (6), is the air-side thermal resistance. i.e.:

$$R_a = \frac{\Delta T_{lm}}{q} = \frac{1}{\eta_{o,a} A_a h_a} \tag{14}$$

where A_a is the air side area computed by $A_a = 4 n_{ch}^\circ D_s L$ for the square channels geometry and $A_a = n_{ch}^\circ \pi D_{int} L$ for the round tube bank. The $\eta_{o,a}$ is the air-side fin global efficiency of the square channels modeled as fins with uniform cross-sectional area with its solution detailed in [1]. Manipulating the previous equations, the air side heat transfer coefficient h_a, for the square channel core of the heat exchanger, can be computed by:

$$h_a = \frac{1}{\eta_{o,a}} \left(\frac{1}{U_a} - \frac{A_a \delta_w}{A_w k_w} - \frac{A_a}{A_v h_v} \right)^{-1} \tag{15}$$

For round tubes, this expression takes the form:

$$h_a = \left(\frac{1}{U_a} - \frac{A_a \ln\left(D_{ext}/D_{int}\right)}{2\pi k_w L} - \frac{A_a}{A_v h_v} \right)^{-1} \tag{16}$$

As already discussed, considering the vapor-side wall temperature constant, it is possible to simplify the "known side", disregarding it. The complete analysis involving this hypothesis is described in Section 2.4.

Finally, the Nusselt number (Nu) can be computed from its definition, as:

$$Nu = \frac{h_a D_h}{k_a} \tag{17}$$

where, the heat transfer coefficient h_a is defined by Eqs. (15) or (16) (depending on the geometry of the core), k_a is the air thermal conductivity and D_h is the hydraulic diameter.

Table 2.6 shows recent and consolidate correlations and models, taken from the literature, to determine the Nusselt number for square channels and round tubes in laminar (Shah and London [30], Muzychka and Yovanovich [31] and Gnielinski [32]), transitional flow regimes (Gnielinski [32] and Sarmiento et al. [33]) and turbulent (Gnielinski [32], Petukhov and Popov [34], Colburn [35], Dittus-Boelter [35]). Note that for the model of Sarmiento et al. [33], the turbulent Nusselt number was written in terms of the area square root, instead of hydraulic diameter. The predictions of these models are compared with the experimental data. Discussions are shown on Section 2.4.

Table 2.6 –Literature correlations and models of Nusselt number for square cross section channels and round tubes from laminar to turbulent flow regimes.

Ref.	Equation

Shah and London (1978) [30] (Laminar Flow)	$$\overline{Nu}_{D,lam} = \begin{cases} 1.953\left(\dfrac{1}{L^*_{th,D}}\right)^{1/3} \; ; \; L^*_{th,D} \le 0.03 \\[4mm] 4.36 + 0.0722\left(\dfrac{1}{L^*_{th,D}}\right) ; \; L^*_{th,D} > 0.03 \end{cases} \; ; \; Re_D < 2300$$ $$L^*_{th,D} = \frac{L/D_h}{Re_D \, Pr}$$	(18)
Muzychka and Yovanovich (2004) [31]: (Laminar Flow)	$$\overline{Nu}_{\sqrt{A},lam} = \left[\left(C_4 \frac{f(Pr)}{\sqrt{L^*_{th,\sqrt{A}}}}\right)^m + \left(\left\{C_2 C_3\left(\frac{f\,Re_{\sqrt{A}}}{\sqrt{L^*_{th,\sqrt{A}}}}\right)^{1/3}\right\}^5 + \left\{C_1\left(\frac{f\,Re_{\sqrt{A}}}{8\sqrt{\pi}\,\varepsilon^\gamma}\right)^{1/3}\right\}^5\right)^{m/5}\right]^{1/m}$$ $$L^*_{th,\sqrt{A}} = \frac{L/D_h}{Re_{\sqrt{A}}\, Pr}$$ $$f(Pr) = \frac{0.564}{\left[1 + \left(1.909\,Pr^{1/6}\right)^{9/2}\right]^{2/9}}$$ $$f\,Re_{\sqrt{A}} = \left[\left(\frac{12}{\sqrt{\varepsilon}(1+\varepsilon)\left[1 - \frac{192\varepsilon}{\pi^5}\tanh\left(\frac{\pi}{2\varepsilon}\right)\right]}\right)^2 + \left(\frac{3.44}{\sqrt{L^*_{th,\sqrt{A}}}}\right)^2\right]^{1/2}$$ $$m = 2.27 + 1.65\,Pr^{1/3}$$ $$C_1 = 3.24; \; C_2 = 3/2; \; C_3 = 0.409; \; C_4 = 2; \; \gamma = 1/10$$ $$0.1 < Pr < \infty; \; Re_{\sqrt{A}} < 2037$$	(19)
Gnielinski (2010) [32]: (Laminar Flow)	$$\overline{Nu}_{D,lam} = \left[Nu_{D,T,1}^3 + 0.7^3 + \left(Nu_{D,T,2}^3 - 0.7\right)^3 + Nu_{D,T,3}^3\right]^{1/3}$$ $$Nu_{D,T,1} = 3.66$$ $$Nu_{D,T,2} = 1.615\sqrt[3]{Re_D\,Pr\,D_h/L}$$ $$Nu_{D,T,3} = \left(\frac{2}{1+22\,Pr}\right)^{1/6}\left(Re_D\,Pr\,\frac{D_h}{L}\right)^{1/2}$$ $$Re_D < 2300$$	(20)
Gnielinski (2010) [32]: (Turbulent Flow)	$$\overline{Nu}_{D,tur} = \frac{(f/8)(Re_D - 1000)Pr}{1 + 12.7\sqrt{(f/8)}\left(Pr^{2/3} - 1\right)}\left[1 + \left(\frac{D_h}{L}\right)^{2/3}\right]$$ $$f = \left[1.82\left(\log_{10} Re_D\right) - 1.64\right]^{-2}$$ $$0.5 < Pr < 2000 \; ; \; 4000 < Re_D < 1\times10^6$$	(21)
Petukhov − Popov (1963) [34]: (Turbulent Flow)	$$\overline{Nu}_{D,tur} = \frac{(f/2)Re_D\,Pr}{C + 12.7\sqrt{(f/2)}\left(Pr^{2/3} - 1\right)}$$ $$f = 0.00128 + 0.1143\,Re_D^{-0.311}$$ $$C = 1.07 + \frac{900}{Re_D} - \frac{0.63}{1 + 10\,Pr}$$ $$0.5 < Pr < 1\times10^6 \; ; \; 4000 < Re_D < 5\times10^6$$	(22)

Colburn correlation apud Bhatti and Shah (1987) [35]: (Turbulent Flow)	$$\overline{Nu}_{D,tur} = 0.023\,\mathrm{Re}_D^{0.8}\,\mathrm{Pr}^{1/3}$$ $$0.5 < \mathrm{Pr} < 3 \; ; \; 10^4 < \mathrm{Re}_D < 10^5$$	(23)
Dittus-Boelter correlation apud Bhatti and Shah (1987) [35]: (Turbulent Flow)	$$\overline{\mathrm{Nu}}_{D,tur} = \begin{cases} 0.024\,\mathrm{Re}_D^{0.8}\,\mathrm{Pr}^{0.4} & \text{for heating} \\ 0.023\,\mathrm{Re}_D^{0.8}\,\mathrm{Pr}^{1/3} & \text{for cooling} \end{cases}$$ $$0.7 < \mathrm{Pr} < 120 \; ; \; 2500 < \mathrm{Re}_D < 1.24 \times 10^5$$	(24)
Gnielinski (2010) [32]: (Transitional Flow)	$$\overline{Nu}_{D,tran} = (1-\chi)\overline{Nu}_{D,l}\left(\mathrm{Re}_D = 2300\right) + \chi\overline{Nu}_{D,t}\left(\mathrm{Re}_D = 4000\right)$$ $$\overline{Nu}_{D,l} = Eq.20$$ $$\overline{Nu}_{D,t} = Eq.21$$ $$\chi = \frac{\mathrm{Re}_D - 2300}{4000 - 2300} \; ; \; 0 \le \chi \le 1$$	(25)
Sarmiento *et al.* (2020) [33]: (Transitional Flow)	$$\overline{Nu}_{\sqrt{A},tran} = \left[\overline{Nu}_{\sqrt{A},lam}^{m_c} + \left(\frac{\Psi}{\overline{Nu}_{\sqrt{A},lam}^2 + \overline{Nu}_{\sqrt{A},tur}^2} \right)^{-\frac{m_c}{2}} \right]^{\frac{1}{m_c}}$$ $$\Psi = \exp\left[-\frac{\left(\mathrm{Re}_{\sqrt{A},critical} - \mathrm{Re}_{\sqrt{A}}\right)^2}{B^2} \right]$$ $$\overline{Nu}_{\sqrt{A},l} = Eq.19$$ $$\overline{Nu}_{\sqrt{A},t} = Eq.21$$ $$m_c = 12 \; ; \; \mathrm{Re}_{\sqrt{A},critical} = 1700 \; ; \; B = 406$$	(26)

2.3.3 Friction factor

The friction factor is determined by means of the experimental procedure described in Section 2.2. The input parameters are: the geometry, the inlet fluid temperature and pressure, the core pressure drop and the outlet fluid temperature. The "hot" friction factor, in steady flow rate conditions can be obtained by the following expression, proposed by Shah et al. [1]:

$$f = \frac{r_h}{L} \frac{1}{(1/\rho)_m} \left[\frac{2\Delta p}{G^2} - \frac{1}{\rho_i}\left(1 - \sigma^2 + K_c\right) - 2\left(\frac{1}{\rho_o} - \frac{1}{\rho_i}\right) + \frac{1}{\rho_o}\left(1 - \sigma^2 - K_e\right) \right] \tag{27}$$

where, r_h is the hydraulic radius, which, by definition, is equivalent to $r_h = D_h/4$ and L is the length of the core section. In the hot tests, the air was considered a perfect gas with the mean specific volume evaluated by:

$$\left(\frac{1}{\rho}\right)_m = \frac{\tilde{R}}{p_{ave}} T_{a,lm} \tag{28}$$

where, $\tilde{R}$ is the gas constant in [J/kg.K] and average pressure is given by $p_{ave} = \left(p_i + p_o\right)/2$. In Eq. (27), $\sigma = A_{ff}/A_{fr}$, is the ratio between the free-flow area and the air-side core frontal area, A_{fr}. K_c and K_e are the contraction and expansion coefficients, as proposed by [1] and [14],

and, finally, the densities ρ_i and ρ_o are evaluated at the inlet and outlet temperatures and pressures, respectively.

Table 2.7 presents some correlations and models suggested by the literature to determine the friction factor for square cross section channels and round tubes in laminar (Muzychka and Yovanovich [36]), transitional flow regimes (Sarmiento et al. [37]) and turbulent (Filonenko [38], and Colebrook [39]). The laminar Fanning friction factor in Eq. 32 is determined using Eq. 29. In addition, the Eqs. 29 and 32 use the Reynolds number based in the area square root.

Table 2.7 – Literature correlations and models of Fanning friction factor for square cross section channels and round tubes from laminar to turbulent flow regimes.

Ref.	Equation	
Muzychka and Yovanovich (2009) [36] (Laminar Flow)	$f = \dfrac{1}{\mathrm{Re}_{\sqrt{A}}} \left\{ \left(\dfrac{3.44}{\sqrt{L^+}}\right)^2 + \left(\dfrac{12}{\sqrt{\varepsilon}\,(1+\varepsilon)\left[1 - \dfrac{192\varepsilon}{\pi^5}\tanh\left(\dfrac{\pi}{2\varepsilon}\right)\right]}\right)^2 \right\}^{1/2}$ $L^+ = \dfrac{L/D_h}{\mathrm{Re}_{\sqrt{A}}}$ $\mathrm{Re}_{\sqrt{A}} < 2300$	(29)
Filonenko (1954) [38]: (Turbulent Flow)	$f = \left[1.82\left(\log_{10}\mathrm{Re}_D\right) - 1.64\right]^{-2}$	(30)
Colebrook (1939) [39]: (Turbulent Flow)	$\dfrac{1}{\sqrt{f}} = -2.0\log\left(\dfrac{e/D_h}{3.7} + \dfrac{2.51}{\mathrm{Re}_D\sqrt{f}}\right)$	(31)
Sarmiento et al. (2021) [37]: (Transitional Flow)	$f_{\sqrt{A}} = \left[1 + \left(\dfrac{1.12 D_h}{L}\right)^{2/3}\right] f_L^{\alpha_f}\, f_{TS}^{1-\alpha_f}\, f_{TR}^{(1-\alpha_f)(1-\beta_f)}$ $f_L = Eq.29$ $f_{TS} = \dfrac{1}{4}\left[1.8\left(\log_{10}\dfrac{\mathrm{Re}_{\sqrt{A}}}{6.02}\right)\right]^{-2}$ $f_{TS} = \dfrac{1}{4}\left[2\left(\log_{10}\dfrac{4.17 D_h}{6.02}\right)\right]^{-2}$ $\alpha_f = \dfrac{1}{1 + \left(\dfrac{\mathrm{Re}_{\sqrt{A}}}{2410}\right)^2}$ $\beta_f = \dfrac{1}{1 + \left[\dfrac{0.886\,\mathrm{Re}_{\sqrt{A}}}{(320 r/e)}\right]} \;\; ; \;\; r = \dfrac{D_h^2}{P}$	(32)

2.3.4 Temperature-dependent fluid properties correction

The air properties are very temperature dependent. The viscosity, thermal conductivity and density are functions of the absolute temperature and may be very sensitive to its variations [13]. Thus, when the fluid temperature differs significantly from the wall temperature, is necessary to apply some correction to the data, to take into account the effect of fluid property

variations. In this work, the property ratio method, extensively used for internal flow, is applied. For gases, the effects of the temperature in the Nusselt number and in the friction factor, due to property variations, are correlated by the following equations, respectively [13]:

$$\frac{Nu}{Nu_{cp}} = \left(\frac{T_w}{T_m}\right)^n \tag{33}$$

$$\frac{f}{f_{cp}} = \left(\frac{T_w}{T_m}\right)^m \tag{34}$$

For the present case, the log-mean temperature $T_{a,lm}$ is considered the mixed mean fluid temperature, T_m. The subscript cp in Eqs. (33) and (34) refer to constant properties (i.e., Nu and f for constant fluid properties). The exponents "n" and "m" of Eqs. (33) and (34) can assume different values, depending on the boundary conditions and the heat transfer geometry. Table 2.8 shows the values for these exponents, as proposed by the literature [1], for laminar and turbulent flows of gases in circular tubes, considering a heating condition.

Table 2.8 - Property ratio method exponents.

Fluid	Heating
	Laminar flow
Gas	$n = 0.0$, $m = 1$ for $1 < T_w/T_m < 3$
	Turbulent flow
Gas	$n = -0.5$, $m = -0.1$ for $1 < T_w/T_m < 2.4$

According to Shah [1], the constants shown in the Table 2.8 are obtained considering constant heat flux boundary conditions. As, in the present study, the boundary conditions can be quite different, i.e., constant wall temperatures, the proposed coefficients may not be very accurate to correct the properties.

2.4 Results

The experimental data generated with the procedure described in Section 2.2 were treated using the reduction method described in Section 2.3. According with Shah [1], this method can be considered precise if some requirements are met:
- constant temperature condition and homogeneity in the heat transfer rate trough the core walls;
- the number of heat transfer units (NTU) should be between 0.5 and 3;
- the steam-side thermal resistance must be much smaller than the air side one.

All the thermo-hydraulic dimensionless characteristics for the gas flow (air) were adjusted using Eqs. 33 and 34, to correct the high temperature difference between the fluid and the heat exchanger walls observed during tests.

In this section each of the above three requirements are evaluated based on the experimental data obtained, with the objective of verifying whether Section 2.2 experimental procedure, based on Kays and London method [14] is adequate for the present study.

2.4.1 Constant wall temperature requirement

The use of two-phase thermosyphons coupled to compact heat exchangers should fulfill the constant wall temperature requirement, as phase-change heat transfer coefficients, established at the condenser section, are very high. However, temperature gradients along the condenser walls may be present [19] if condensation takes place in the presence of non-condensable gases (NCG), compromising the hypothesis of constant temperatures. To mitigate this problem, it is necessary to carry out a purge procedure before starting the experiments, in order to eliminate any possible NCGs that would be present in the thermosyphon. In this work, the purge process was carried out in three stages: thermosyphon pressurization, first purge and second purge.

Data from a typical purge procedure, which followed the steps mentioned in Section 2.2, are discussed. For purging, the needle valve, located at the top of the thermosyphon condenser, is opened until vapor is released from the device to the atmosphere. The thermosyphon vapor temperature was maintained at 180°C, which corresponds to an internal pressure of approximately 10 bar, while a constant temperature air flow rate of 0.20kg/min at 65°C was passing through the heat exchanger core.

Figure 2.7 shows the thermosyphon transient temperatures (evaporator, adiabatic section and condenser) during the three stages of the purging process, while Figure 2.8 shows the condenser temperature non-uniformity (ΔT is the maximum minus the minimum temperatures obtained from the six thermocouples installed on the condense section, where $\Delta T = 0$ means that the temperature through the condenser is completely uniform and stable).

Without purge (pressurization stage), a temperature difference of 3.5 °C was obtained between the condenser and the adiabatic sections (number 1 in Figure 2.7), while the condenser temperature was oscillating, with an average of 2.38 °C (number 1 in Figure 2.8). After the first purge, represented by numbers (2) in Figures 2.7 and 2.8, the temperature difference between the adiabatic section and the condenser reduced to approximately 1.5 °C, while the differences in the temperature along the condenser also reduced to 0.61 °C in average. Finally, after the second purge process, characterized by numbers (3) in Figures 2.7 and 2.8, the thermosyphon condenser and adiabatic section temperatures approached to 0.75 °C of difference and the temperature readings dispersion reduced to 0.22 °C, lower than the measurement uncertainty of the thermocouples used in the experiment (0.5°C). These results are compatible with a thermosyphon free from NCGs, showing a uniform and stable wall temperature on the vapor side of the heat exchanger core (thermosyphon condenser).

The geyser boiling is another thermosyphon temperature phenomenon that could compromise the desired constant wall temperature condition at the condenser walls. This effect is characterized by periodic temperature oscillations and generally occurs at low heat flux and/or high confinement numbers. The confinement number Co is quantified as the ratio of the capillary length of the fluid and the channel hydraulic diameter [40 - 41]. This is one of the main parameters affecting the Geyser boiling regime. For $Co > 0.5$ confinement effects are significant, and their effects begin to be observed at low as $Co \approx 0.35$ [42]. The confinement number was calculated for the present case, being the maximum value of $Co \approx 0.05$, which indicate the thermosyphon does not operate on confined condition, reducing the chance of geyser boiling. Moreover, from the analysis of Figures 2.7 and 2.8, which shows the condenser temperature readings over approximately three hours under steady-state regime, no significant temperature oscillation was observed, suggesting the geyser boiling doesn't occur at the tested conditions.
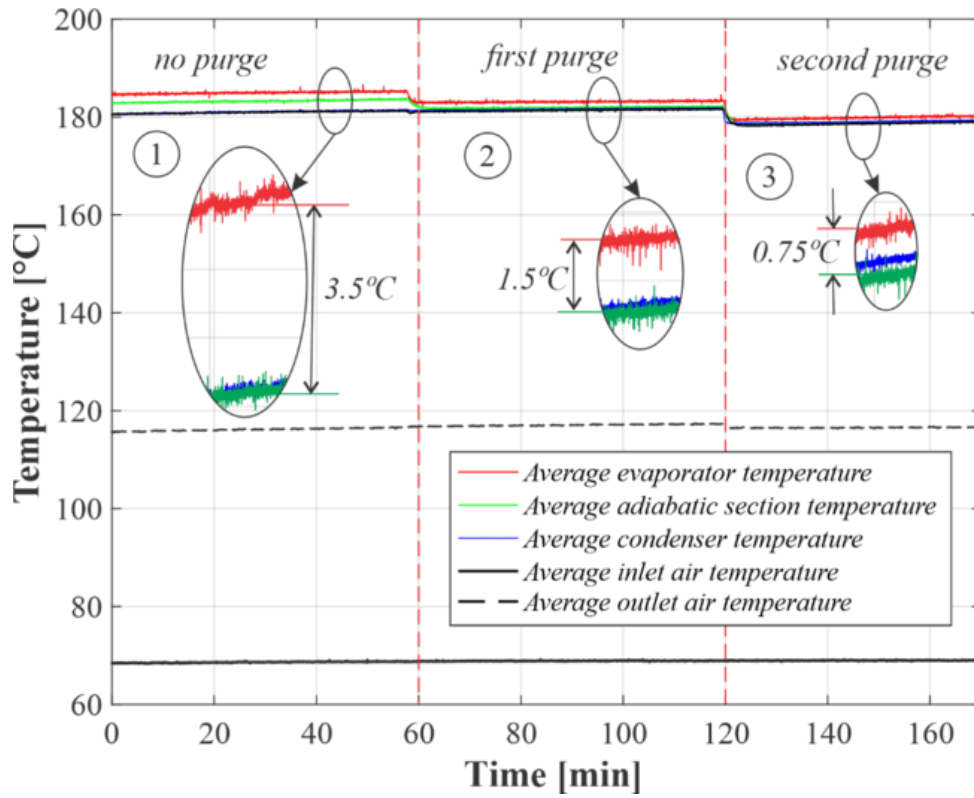
Figure 2.7 - Thermosyphon temperature transient during the purge procedure.
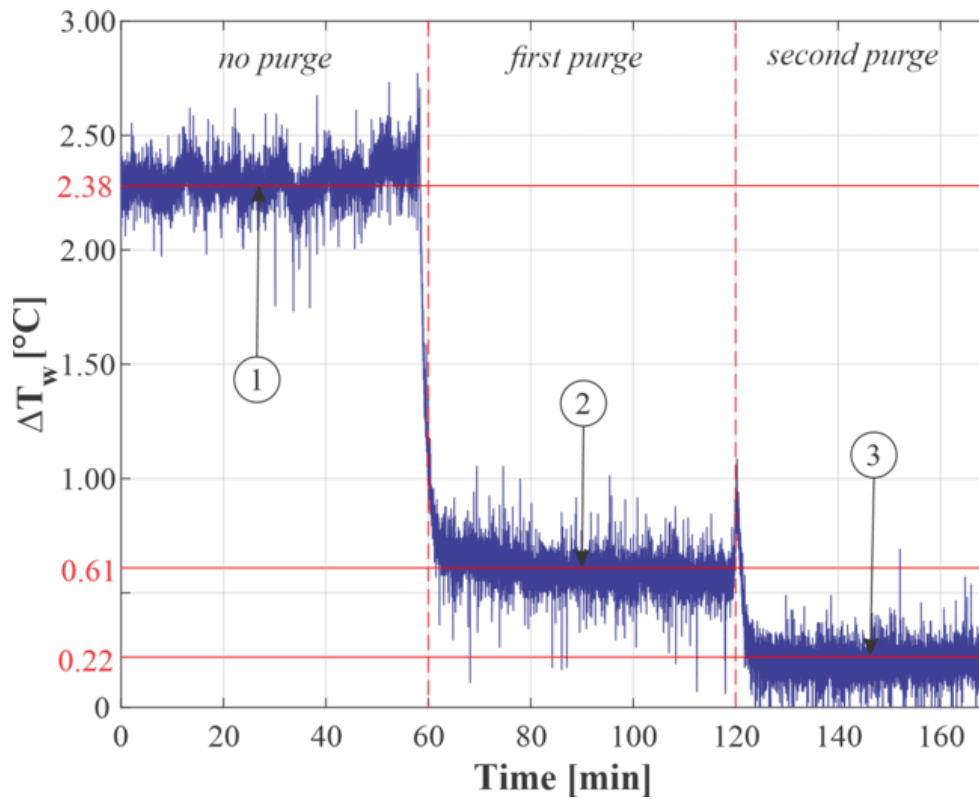
Figure 2.8 - Transient condenser temperature $\left(T_w\right)$ analysis during the purge procedure.

2.4.2   Evaluation of the number of transfer units (NTU)

Once the constant wall temperature condition was guaranteed, the experimental tests presented in the matrix of experiments (Table 2.3) were carried out. Figure 2.9 shows the number of transfer units (NTU), computed by the Eq. 5, for the two cores studied in this work. According to the criteria established by Shah [1] to provide a high-accuracy in data, the NTU has to be kept between 0.5 and 3, which was satisfied in both core cases. The square cross section channel heat exchanger geometry was tested in the laminar and transition flow regimes, which correspond to approximately Reynolds numbers range between 850 and 2800. However, the core composed of round tubes was tested in the transition and turbulent flow regimes, corresponding to Reynolds range from approximately 2200 to 8000. Even though the mass flow rates tested in both exchangers were very similar (see test matrix Table 2.3), the different flow regimes obtained are mainly due to the difference in the number of channels of each core (50 channels in the square channel and 16 channels in the round tubes). The number of channels in both exchangers was intentionally selected to test the workbench in all fluid flow regimes, from laminar to transition regime in square channel core and transition to turbulent regime in round tube core. The Figure 2.9 also shows that, regardless of the wall temperature, the NTU maintained a practically stable condition, and it decreased exponentially as a function of the Reynolds number, presenting practically constant values (approximately 0.6) for Reynolds greater than 2000.
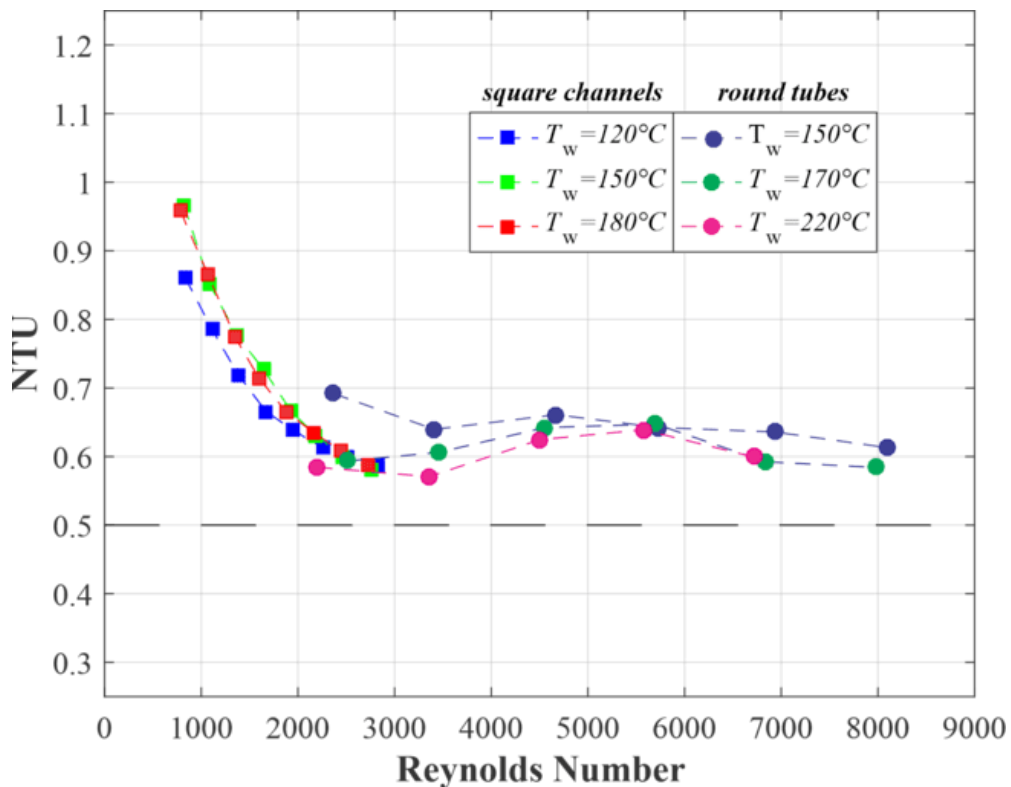
Figure 2.9 - Number of heat transfer units (NTU) vs. Reynolds number for the square channels and round tubes heat exchangers core.

2.4.3   Evaluation of the dominant thermal resistance

Another requirement for the use of the data reduction method is that the air-side thermal resistance is dominant over the vapor-side (thermosyphon condenser), i.e. a capacity rate ratio

of $C_{min}/C_{max} \approx 0$. However, the vapor side heat capacity rate $\left(C_{max} = \left(\dot{m}c_p\right)_v\right)$ determination is not straightforward since the condensing vapor mass flow rate is a quite difficult variable to measure. In this case, the heat capacity rate ratio was assessed in in terms of the air side $\left(R_a\right)$ and vapor side $\left(R_v\right)$ thermal resistances. For that, the thermal resistances on the vapor side of the thermosyphon were calculated with experimental data, using the Eq. 12, and theoretically, by the Eqs. 8 and 9, for the square cross section and round tubes respectively. The air-side experimental thermal resistance was evaluated using Eq. 14.

Figures 2.10 and 2.11 show the experimental thermal resistances as a function of the heat transfer rate, for the air and vapor sides, for the square channels and round tubes cores, respectively. The vertical bars represent experimental data uncertainty. The theoretical vapor side thermal resistances were also plotted, in order to verify whether the two-phase thermosyphon condensation models, present in the literature, can be used as a design tool for this kind of device. An average vapor side thermal resistance of around 7x10^{-3} K/W was obtained for the square channels and of 5x10^{-3} K/W for the round tubes. The average air side thermal resistance, for both cases, was approximately 0.5 K/W. This means that the vapor side thermal resistance was approximately two orders of magnitude smaller than that of the air side, fulfilling the requirement of the data reduction method presented in Section 2.3.

Regarding the vapor side, for the square channels core, an average difference of 21% was noticed between data and theoretical model, using the correlation proposed by Groll and Rosler [27] (see Table 2.5), for the prediction of the condensation heat transfer coefficient. Actually, this model is appropriate to vertical condenser walls, as it is based on the Nusselt condensation model in vertical plates [29] (see Figure 2.6, detail A).

For the round tubes core, an average difference between data and model of 38% was obtained with use of the correlation proposed by Kaminaga et al. [28]. This model is usually suggested when it is not possible to recognize the liquid film flow regime within the thermosyphon, which is the case of the crossflow condensing vapor in external surfaces of a bundle of horizontal tubes (Figure 2.6, detail B). In both cases, the differences between the models and the experimental data were almost within the uncertainty of the experiment which, for both geometries, were 31% on average, 22% minimum and 49% maximum, showing that these models can be used to design the compact heat exchanger condenser section of thermosyphons.
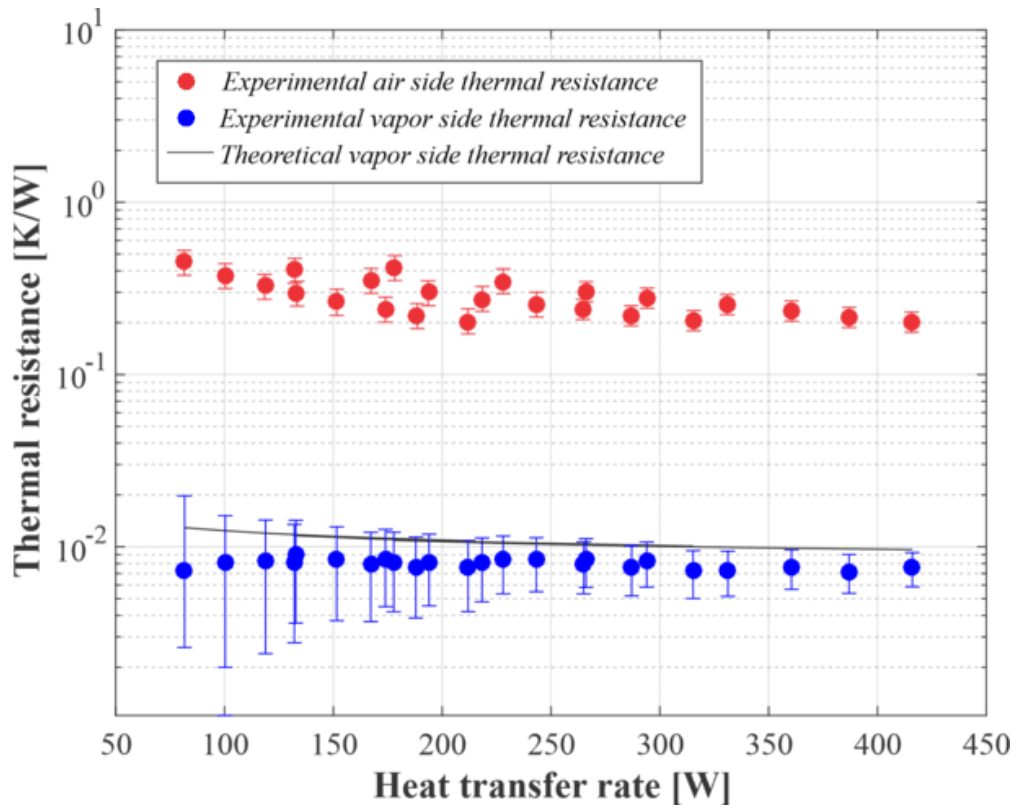
Figure 2.10 - Air side and vapor side thermal resistances magnitude comparison for the square channels heat exchanger core.
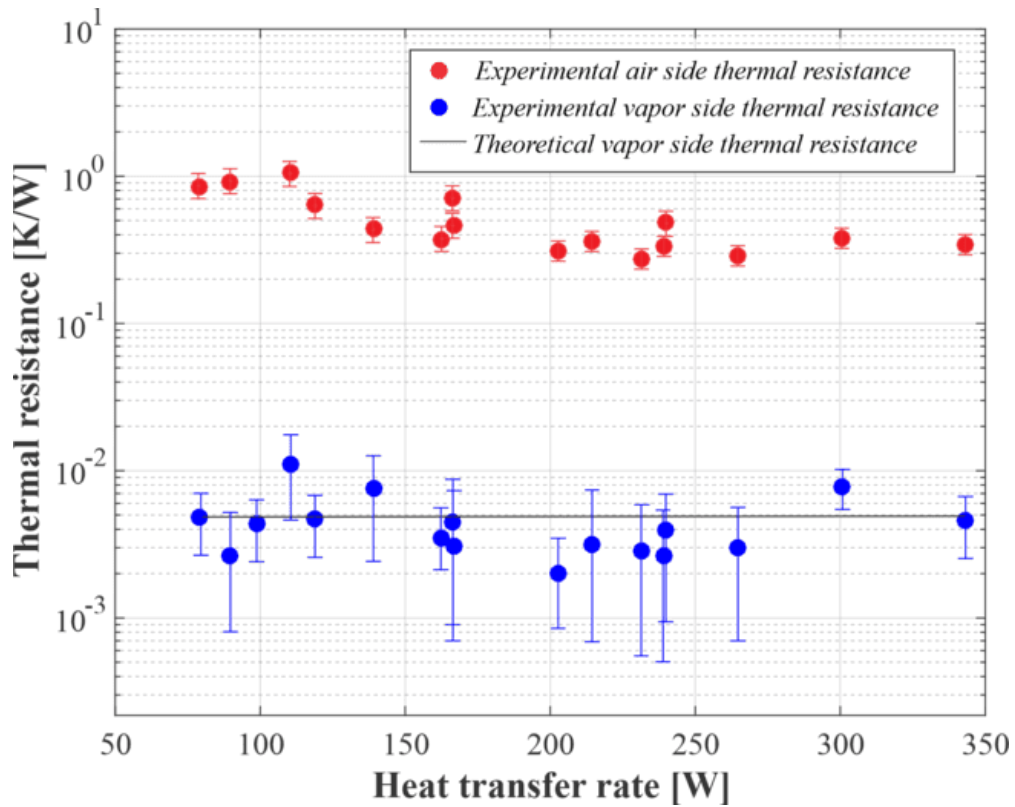
Figure 2.11 - Air side and vapor side thermal resistances magnitude comparison for the round tubes heat exchanger core.

2.4.4 Nusselt number analysis

Figure 2.12 presents the Nusselt number as a function of the Reynolds numbers for the square cross-section channels, the data of which were treated according to the methodology presented in Section 2.3. The Nusselt number data show low dispersion for all wall temperature tested (120, 150 or 180°C). The exponent $n = 0$ was applied in the Eq. 33 to correct the Nusselt number for the fluid temperature properties dependence, for the laminar airflow on a heating condition. To validate the work bench data, experimental Nusselt number was compared with the literature correlations for laminar flow and transition regimes, using the convection heat transfer models proposed by Shah and London [30] and Muzychka and Yovanovich [31] for laminar flow, and Gnielinski [32] and Sarmiento et al. [33] for transitional flow (these model expressions are in Table 2.6).

Figure 2.12 - Comparison of predictions for Nusselt number given by [30], [31], [32] and [33], with the experimental data for the square cross sectional channels heat exchanger core.

The results show that, for low Reynolds numbers smaller than 1000, the model that best represented the experimental data was the correlation proposed by Gnielinski [32], which underestimated Nusselt, for Reynolds greater than 1250. The correlation developed by Shah and London [30] shows a good agreement with data for Reynolds from 1000 to 2000, underestimating Nusselt in the transition region, over 2100. For Reynolds numbers greater than 1500, the models by Muzychka and Yovanovich [31] and Sarmiento et al. [33], presented the best accordance with experimental data, with average errors of approximately 6.9% and 6.7%, respectively, considering the entire range of Reynolds analyze (600 to 2800). The average errors of each of the correlations (600 < Re < 2800) are shown in Table 2.9.

For further analysis, a scatter plot of the experimental data vs. the theoretical Nusselt number predictions is shown in Figure 2.13. The full line corresponds to the match between experimental data and model predictions. The regions between dashed lines represents $\pm 15\%$ of error margin. The models of Sarmiento et al. [33] and Muzychka and Yovanovich [31], deviates from the experimental data within the 15% error margin for Nusselt numbers greater than 6 (Re

> 1200). For Reynolds number smaller than 1500 the error of these models was approximately 20%. On the other hand, the Shah and London [30] and Gnielinski [32] models showed errors less than 15% for Nusselt number smaller than 7 (Re < 1500) but, in the flow transitional region, these models deviate from the experimental data with maximum differences of 27% and 21%, respectively.

Table 2.9 - Square channels geometry standard deviation for 600<Re<2800.

Model	average deviation n=0
Shah and London [30]	13,9%
Muzychka and Yovanovich [31]	6,9%
Gnielinski [32]	13,5%
Sarmiento et al. [33]	6,7%
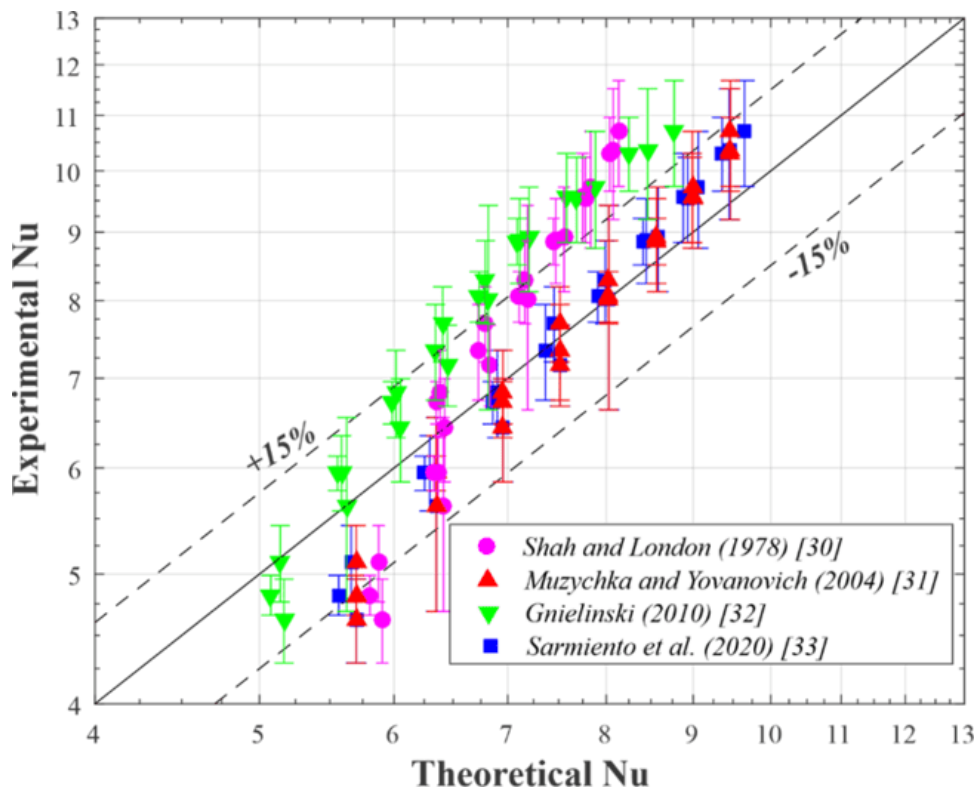
Figure 2.13 –Error band for Nusselt number given by [30], [31], [32] and [33], with the experimental data for the square cross sectional channels heat exchanger core.

Figure 2.14 shows the Nusselt as a function of Reynolds numbers for the round tube heat exchanger, the data of which were corrected with the Eq. 33, using the exponent *n=-0.5,* as suggested by the literature [1] for turbulent airflow on a heating condition (Table 2.8). A greater experimental data scattering was observed due to the temperature effect, when compared to the results obtained in the square cross-sectional channel (laminar regime), especially when the Reynolds number was greater than 3000. The experimental data obtained with higher wall temperatures presented Nusselt numbers slightly lower than those obtained with lower wall temperatures for the same Reynolds number. However, the differences between these experimental data are within the experimental uncertainty range.

The data for round tubes were compared with Petukhov and Popov [34], Colburn and Dittus-Boelter (Bhatti and Shah [35]) correlations for turbulent flow regime, and Gnielinski [32] and Sarmiento et al. [33] correlations for the transition flow regime (Table 2.6).

Nusselt number models of Petukhov and Popov [34], Gnielinski [32] and Sarmiento et al. [33], that take into account the friction factor, presented a better fit with the experimental data (average deviation less than 8%) than the models that do not consider it, as the Colburn and Dittus-Boelter (Bhatti and Shah [35]) which showed average errors of approximately 18%. The model that best fits the experimental data was that of Gnielinski [32], which takes into account the friction factor and also the entrance region effects (which are significant when the exchanger length is small) and the effects associated with the transitional regime, which in this case happens approximately in the range of 2000<Re<3000. The average errors for all models are shown in Table 2.10, for all the tested Re number range (2000<Re<8000).

In the scatter plot of Figure 2.15, it is again apparent that the models that do not take into account the friction factor showed greater discrepancies with the experimental data, especially for Nusselt numbers smaller than 15 (Re < 3000) with deviations greater than 15%. For Reynolds greater than 3000 (Nu > 15) all analyzed models showed high consistency with the experimental data, with errors less than 15%.

In general, a good agreement between the experimental data was obtained, for all the correlations analyzed, showing that the proposed apparatus has great potential for the characterization of the heat transfer coefficient of unknow channels in heat exchangers (especially the compact ones) operating in different flow regimes: laminar, transition and turbulent.
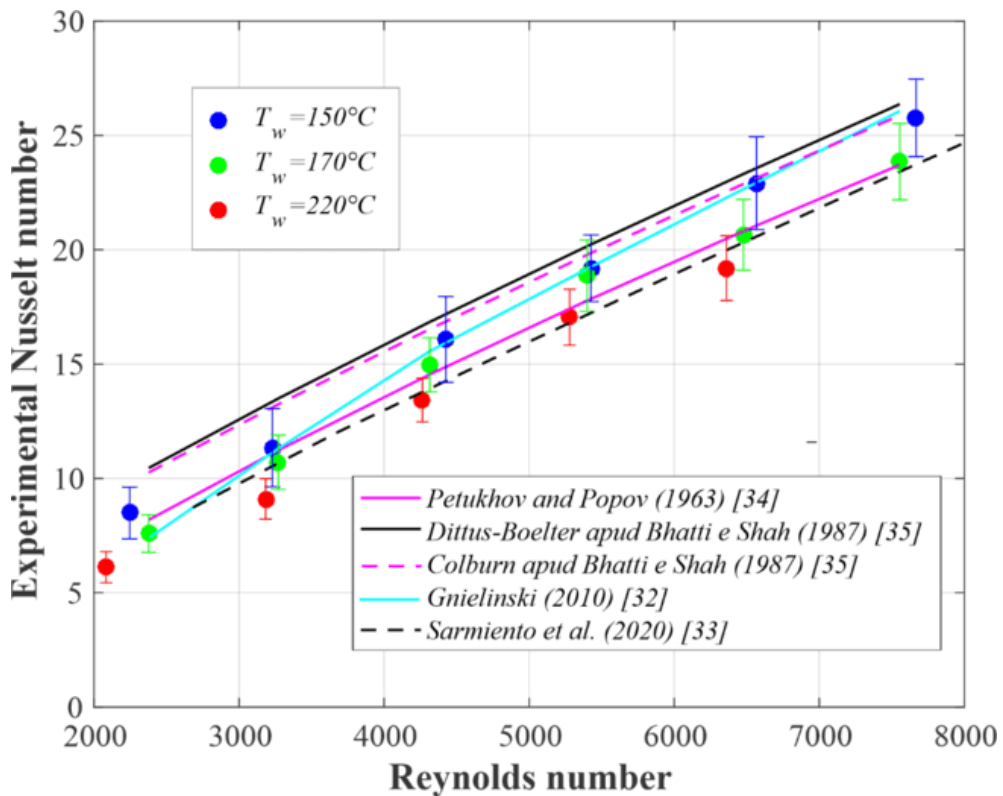
Figure 2.14 - Comparison of Nusselt number correlations given by [32], [33], [34] and [35], with the experimental data of the round tubes heat exchanger core.
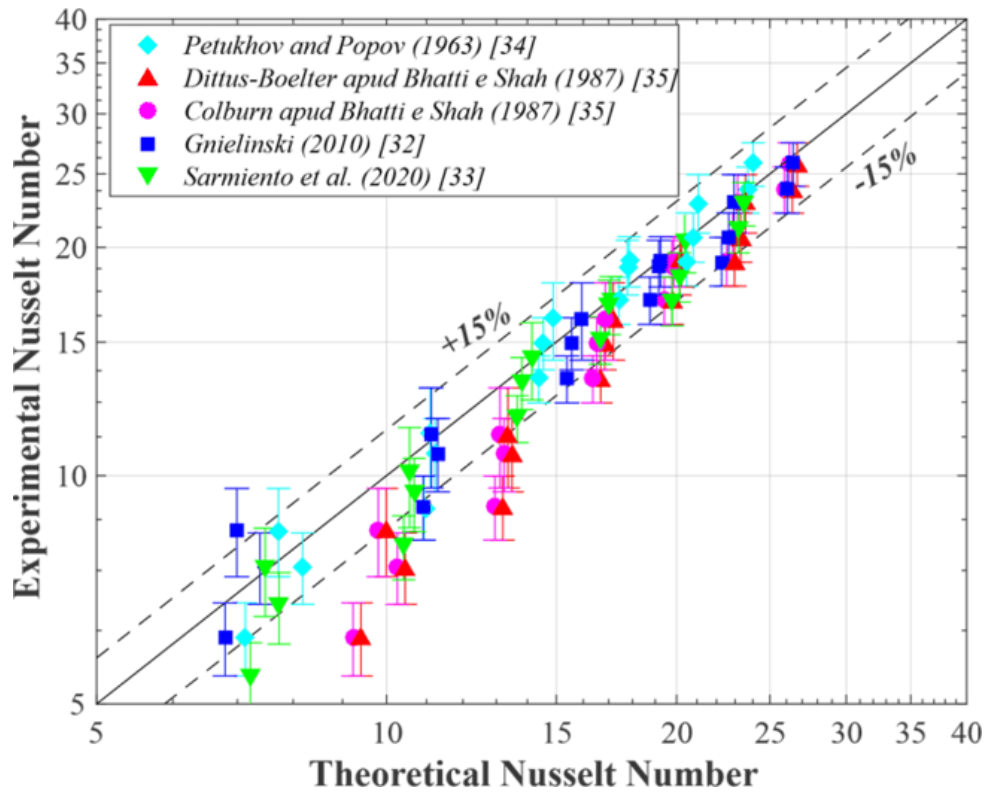
Figure 2.15 - Error band for Nusselt number given by [32], [33], [34] and [35], with the experimental data of the round tubes heat exchanger core.

Table 2.10 – Round tubes heat exchangers core standard deviation for 2000<Re<8000.

Model	average deviation n=-0.5
Petukhov and Popov [34]	7.51%
Dittus-Boelter apud Bhatti e Shah [35]	18.81%
Colburn apud Bhatti e Shah [35]	16.58%
Gnielinski [32]	6.82%
Sarmiento et al. [33]	7.41%

2.4.5 Analysis of the Fanning friction factor

To complete the heat exchanger thermal and hydrodynamic characterization methodology, the friction factor data for the square cross-section and round tube channel, at different temperatures, were evaluated. As mentioned before, the present work doesn't suggest any improvement for the usual friction factor determination methodology. The Fanning friction factor is computed directly by the average data of pressure, mass flow rate and temperatures, as input parameters of Eq. 18. The core entrance and exit pressure-loss coefficients, K_c and K_e were obtained from the multiple-square-tube and round tube chart suggested by Kays and London [13]. In addition, air temperature-dependent properties were adjusted using Eq. 34 for the hot stream friction factors, with exponent "m" equal to 1, for air heating in laminar flow regime (cross-section channel) and equal to -0.1 for air heating in turbulent flow regime (round tube channel), as suggested by Shah et. al [1] (Table 2.8).

The square channels experimental friction factor data, as a function of the Reynolds numbers, are shown in Figure 2.16. The data were compared with the correlations proposed by

Muzychka and Yovanovich [36] and Sarmiento et al. [37] (see Table 2.7), showing good agreement with both correlations, with larger differences for Reynolds numbers smaller than 1000. Also, different data dispersion was noticed for different wall temperatures: at 150 °C, the wall temperature showed the lowest friction factors and the greatest deviations, when compared with data for the temperatures of 120°C and 180°C. However, the deviations for both correlations were below 15% for most of the data, as shown in Figure 2.17.

Table 2.11- Square channels geometry standard deviation for 2000<Re<8000.

Model	average deviation m=1
Muzychka and Yovanovich (2009) [36]	9.12 %
Sarmiento et al. (2021) [37]	10.36 %
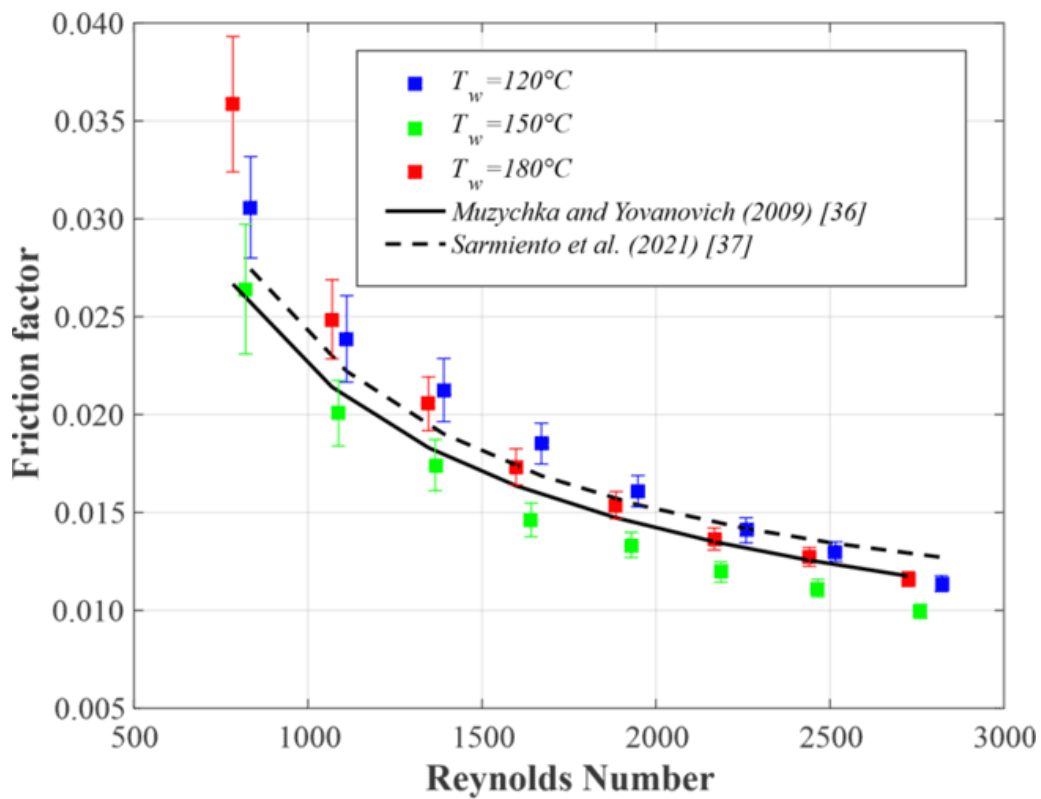
Figure 2.16 – Comparison of friction factor correlations given by [36], [37], with the experimental data of the square channels heat exchanger core.
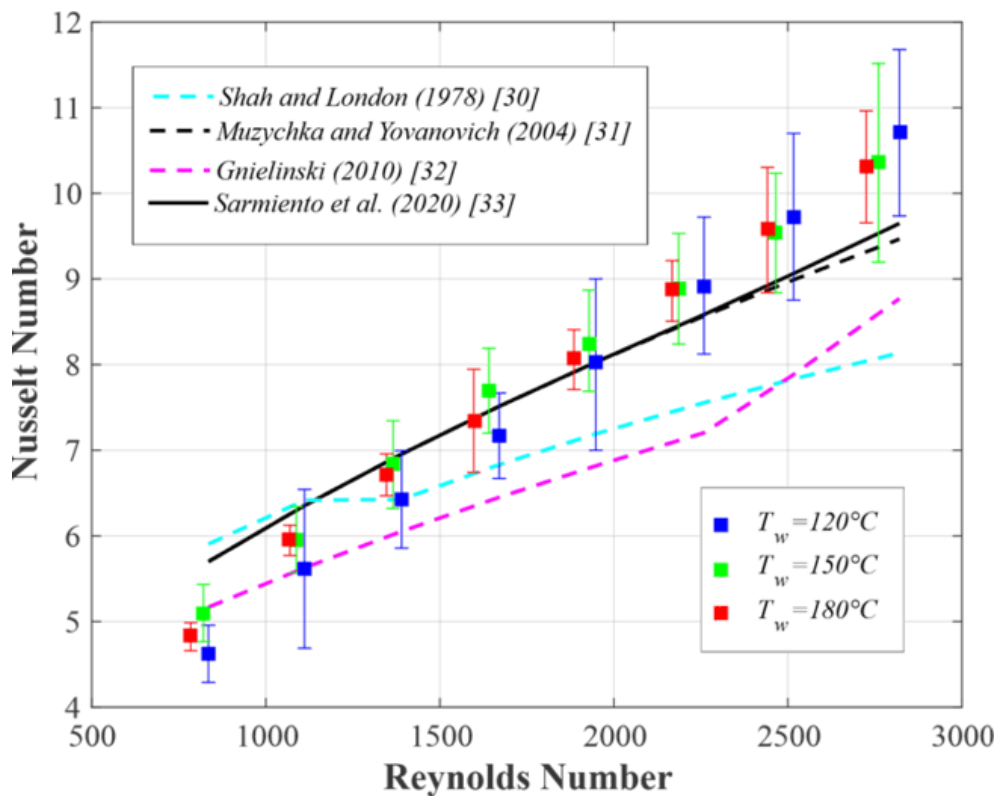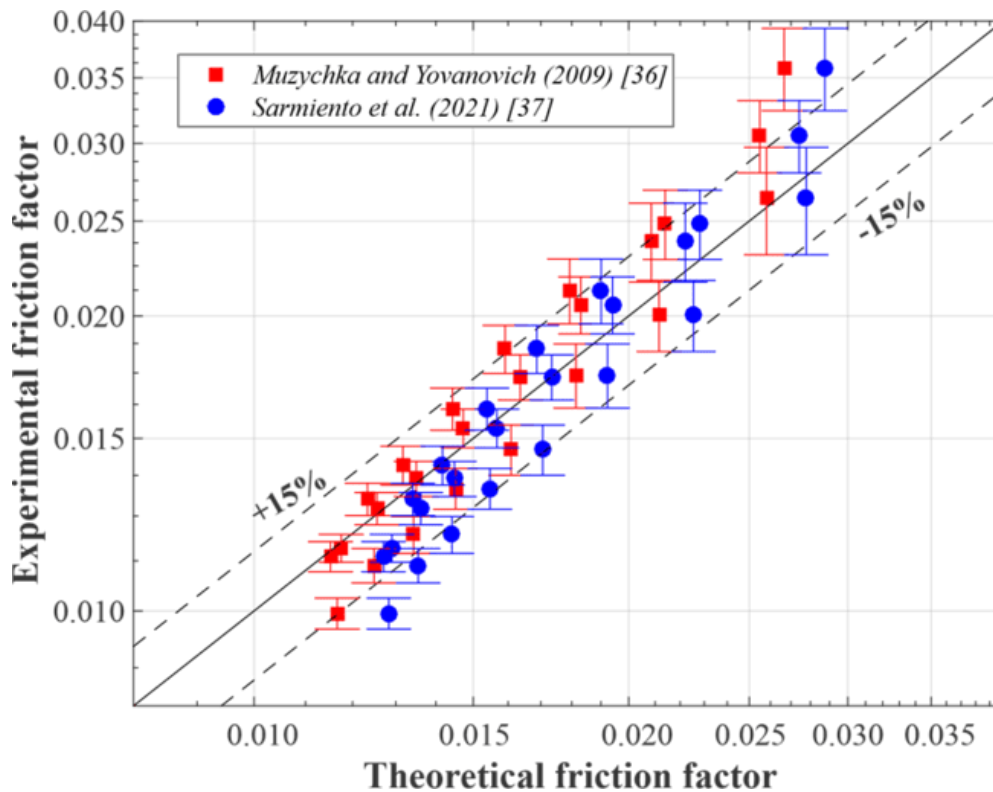
Figure 2.17 - Comparison of predictions for friction factor given by [36] and [37], with the experimental data for the square cross sectional channels heat exchanger core.

In the case of the round tube heat exchanger, the data for the friction factor were recorded at two wall temperatures, 150 and 170 °C, where the results are presented in Figure 2.18 for the Reynolds range from 2000 to 8000. The experimental data were compared with the Filonenko [38] and Colebrook [39] models for turbulent flow and the Sarmiento et al. [37] model for the transitional and turbulent regime (see Table 2.7 for the expressions). For Reynolds number lower than 4000, the experimental data showed greater dispersion between them, due to the effect of temperature (Point 1). At the same point 1 of the Figure 2.18, the data also presented a high discrepancy with the analyzed correlations. The model that presented the best agreement was the one proposed by Sarmiento et al. [37], which is suitable for this regime (transition and turbulent flow regime). For Reynolds numbers greater than 4000, all models analyzed presented similar behavior. In general, the average deviation between the experimental data and all models, for the entire Reynolds range (2000 to 8000) was approximately 15% as shown in Table 2.12.

In the scatter plot of Figure 2.19 all models presented errors greater than 15% for Reynolds number lower than 4000 (experimental friction factors greater than 0.015) as shown in Point 1 of Figures 2.18 and 2.19. This suggests that the exponent $m=-0.1$ used to correct the data in the Eq. 20, for heating in turbulent flow regime is not the most suitable for the transition regime, requiring further studies to determine these exponents for these conditions. However, for Reynolds number greater than 4000 (friction factor smaller than 0.015) all models show errors smaller than 15% with experimental data.

Thus, it is possible to conclude that the experimental setup developed also allows the determination of the characteristics of the friction factor in the core of heat exchangers (especially the compact ones) with average deviations within 15% for the different flow regimes, that is, laminar, transition and turbulent flow regimes.
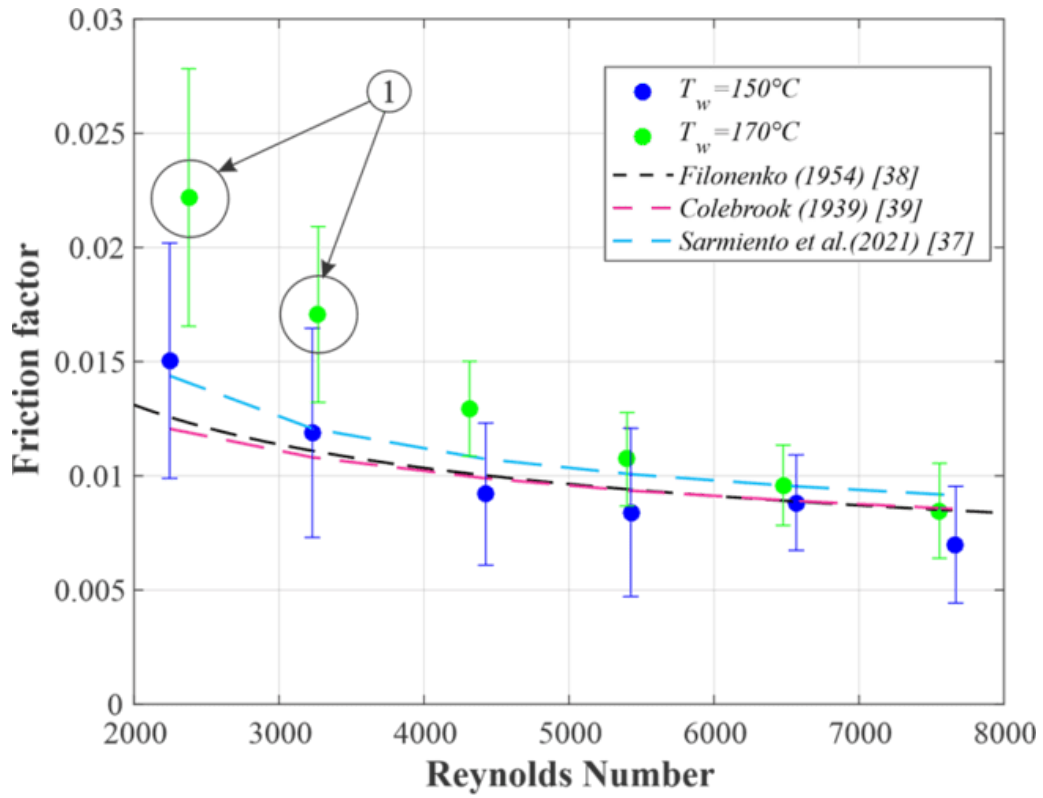
Figure 2.18 – Comparison of friction factor correlations given by [38], [39] and [37] with the experimental data of the round tube heat exchanger core.
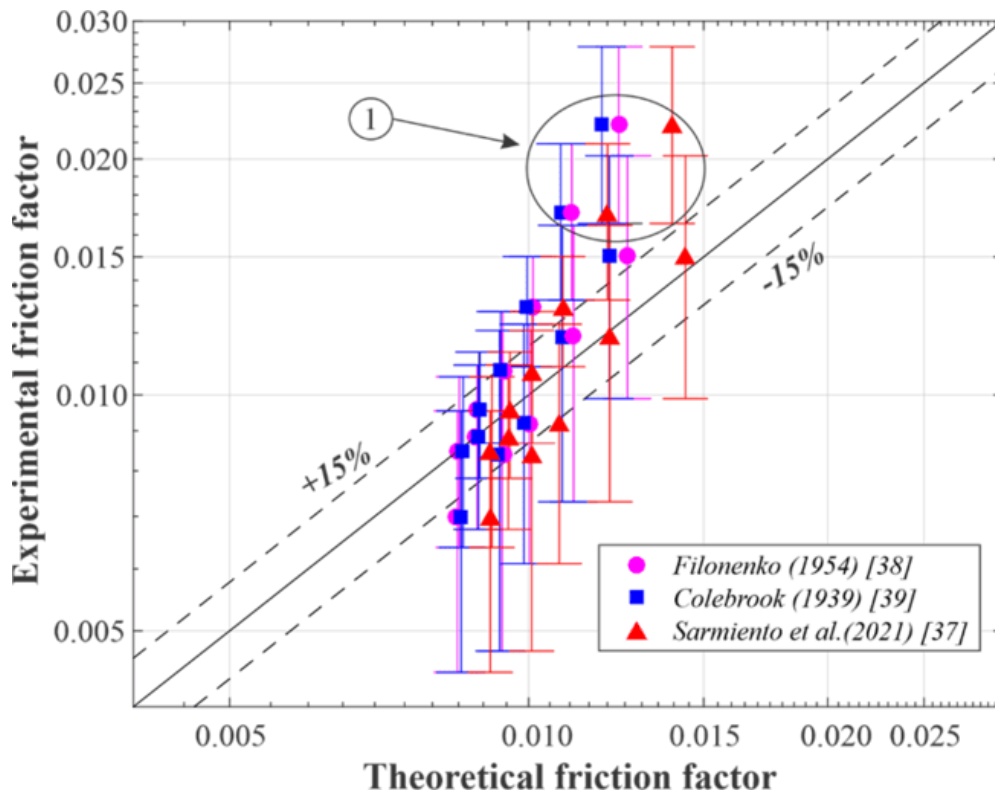
*Figure 2.19 - Comparison of predictions for friction factor given by [38], [39] and [37], with the experimental data for the round tubes heat exchanger core.*

Table 2.12 – Round tubes heat exchangers core standard deviation for 2000<Re<8000.

Modelo	average deviation m=-0.1
Filonenko (1954) [38]	15.60 %
Colebrook (1939) [39]	16.53 %
Sarmiento et al. (2021) [37]	14.92 %

2.5 Discussions and conclusions

A complete experimental methodology for determining the thermo-hydraulic characteristics of channels with unknown geometries, for application in heat exchanger cores, based on the steady-state Kays and London technique, was developed. A two-phase thermosyphon was incorporated into the technique to provide vapor to the known side of the heat exchanger, promoting the constant wall temperature condition at the unknown side under characterization. Two simple and consolidated heat exchanger geometries (square cross section channels and round tubes) were tested in the test rig, to validate the proposed methodology by comparing the results with available models in the literature. The present experimental data, treated with the Kays and London data reduction method, agreed well with the literature models.

In order for this method to be considered accurate, three necessary requirements were analyzed: constant wall temperature condition; number of heat transfer units (NTU), which should be between 0.5-3, and the vapor-side thermal resistance, which must be much smaller than that of the air side.

The two-phase thermosyphon has proved to establish uniform and stable wall temperature conditions on the vapor side of the heat exchanger core (thermosyphon condenser). It was found that the dispersion of temperature readings in the condenser (difference between maximum and minimum temperature recorded) was on average 0.22°C, that is, lower than the measurement uncertainty of the thermocouples used in the experiment (±0.5°C). The number of transfer units was kept in the range of 0.5 to 3, for both heat exchangers. The highest values were observed for the core of square channels for Reynolds number smaller than 2000, with values between 1 to 0.6. For Reynolds numbers greater than 2000, in both cores, the NTU value was approximately 0.6, fulfilling the requirement established by the NTU criterion. In addition, it was found that the thermal resistance of the vapor side (thermosyphon condenser) was approximately of two orders of magnitude lower than that of the air side, that is, the average thermal resistance of the steam side was of approximately 7×10^{-3} K/W, for square channels, and of 5×10^{-3} K/W, for round tubes, while the average thermal resistance on the air side, for both configurations, was approximately 0.5 K/W.

Finally, the thermal and hydrodynamic characteristics of the two cores (square cross section channels and round tubes) were determined and the results of the Nusselt number and friction factor were compared with consolidated models in the literature. For both the square channel and the round tubes heat exchangers, the average deviation between the experimental data and all models, for the Nusselt number and for the friction factor, were in the range of 15%. The experimental results were encouraging, as thermosyphons showed to provide, to the known side of heat exchangers, the expected temperature uniformity, control and stability during the experiments.

Furthermore, it can be concluded that different heat exchanger cores, with any channel geometries, can be characterized by incorporating the core, containing the unknown surface, to the thermosyphon condenser.

In conclusion, the experimental setup proposed has many important good features: it is versatile, able to provide fine tuning and precise control of the testing variables and presents

reduced size and cost, being, therefore, a valuable tool for the characterization of unknown heat transfer geometries for application in the compact heat exchanger cores, whose channels have intricate geometries.

2.6 References

[1] Shah, R. K.; Sekulik, D. P., Fundamentals of heat exchanger design. John Wiley & Sons, 2003.

[2] Wilson, E. E., A basis of rational design of heat transfer apparatus, ASME Journal of Heat Transfer 37 (1915) 47-70.

[3] Shah, R. K., Assessment of modified Wilson plot techniques for obtaining heat exchanger design data, Proceedings of Ninth International Heat Transfer Conference 5 (1990) 51-56.

[4] Styrylska, T. B., and Lechowska, A. A. Unified Wilson Plot Method for Determining Heat Transfer Correlations for Heat Exchangers, ASME J. Heat Transfer, (2003); 125(4): 752–756. https://doi.org/10.1115/1.1576810

[5] Hwang, K., Jeong, J., Hyun, S., Saito, K., Kawai, S., Inagaki, K., & Ozawa, R. (2003). Heat transfer and pressure drop characteristics of enhanced titanium tubes. Desalination, 159(1), 33–41. doi:10.1016/s0011-9164(03)90043-9

[6] Katz, A., Aakre, S. R., Anderson, M. H., & Ranjan, D. (2021). Experimental investigation of pressure drop and heat transfer in high temperature supercritical $CO2$ and helium in a printed-circuit heat exchanger. International Journal of Heat and Mass Transfer, 171, 121089. https://doi.org/10.1016/j.ijheatmasstransfer.2021.121089

[7] Seo, J.-W., Cho, C., Lee, S., & Choi, Y.-D. (2015). Thermal Characteristics of a Primary Surface Heat Exchanger with Corrugated Channels. Entropy, 18(1), 15. doi:10.3390/e18010015

[8] Cowell, T. A. (2011). The Wilson Plot – why it doesn't work and what to do about it. Vehicle Thermal Management Systems Conference and Exhibition (VTMS10), 99–106. doi:10.1533/9780857095053.2.99

[9] Fernández-Seara, J., Uhía, F. J., Sieres, J., & Campo, A. (2007). A general review of the Wilson plot method and its modifications to determine convection coefficients in heat exchange devices. Applied Thermal Engineering, 27(17-18), 2745–2757. doi:10.1016/j.applthermaleng.2007

[10] Howard, C. P. (1967). The Single-Blow Transient Testing Technique for Compact Heat Exchanger Surfaces. Journal of Engineering for Gas Turbines and Power, 89(1), 29. doi:10.1115/1.3616604

[11] Ranganayakulu, C., Luo, X., & Kabelac, S. (2017). The single-blow transient testing technique for offset and wavy fins of compact plate-fin heat exchangers. Applied Thermal Engineering, 111, 1588–1595. doi:10.1016/j.applthermaleng.2016.05.118

[12] Wu, Z., Xu, S., Yang, L., & Wang, Z. (2020). Numerical investigation of single-blow transient testing technique. International Communications in Heat and Mass Transfer, 105023. doi:10.1016/j.icheatmasstransfer.2020.105023

[13] M, Kays W, and London A. L. Compact Heat Exchangers (3rd Edition). S.l.: Scientific International, 2018. Internet resource.

[14]   Saha, S. K., & Haaris Khan, A. (2020). Numerical Study on the Effect of Corrugation Angle on Thermal Performance of Cross Corrugated Plate Heat Exchangers. Thermal Science and Engineering Progress, 100711. doi:10.1016/j.tsep.2020.100711

[15]   Ma, T., Zhang, J., Borjigin, S., Chen, Y.-T., Wang, Q.-W., & Zeng, M. (2015). Numerical study on small-scale longitudinal heat conduction in cross-wavy primary surface heat exchanger. Applied Thermal Engineering, 76, 272–282. doi:10.1016/j.applthermaleng.2014

[16]   Han, Z., Guo, J., Zhang, H., Chen, J., Huai, X., & Cui, X. (2021). Experimental and numerical studies on novel airfoil fins heat exchanger in flue gas heat recovery system. Applied Thermal Engineering, 192, 116939. https://doi.org/10.1016/j.applthermaleng.2021.116939

[17]   Pidaparti, S. R., Anderson, M. H., & Ranjan, D. (2019). Experimental Investigation of thermal-hydraulic performance of discontinuous fin printed circuit heat exchangers for Supercritical CO2 power cycles. Experimental Thermal and Fluid Science. doi:10.1016/j.expthermflusci.2019.04.025.

[18]   Junqi, D., Jiangping, C., Zhijiu, C., Yimin, Z., & Wenfeng, Z. (2007). Heat transfer and pressure drop correlations for the wavy fin and flat tube heat exchangers. Applied Thermal Engineering, 27(11-12), 2066–2073. doi:10.1016/j.applthermaleng.2006.11.012

[19]   Mantelli, M. B. H., Thermosyphons and Heat Pipes: Theory and Applications. Springer Nature, 2021.

[20]   Lukitobudi, A. R., Akbarzadeh, P., Johnson, P. W., & Hendy, P. (1995). Desing, construction and testing of a thermosyphon heat exchanger for medium temperature heat recovery in Bakeries. Heat Recovery Systems & CHP, 481-491.

[21]   Cieśliński, J. T., & Fiuk, A. (2013). Heat transfer characteristics of a two-phase thermosyphon heat exchanger. Applied thermal engineering, 51(1-2), 112-118.

[22]   Song, W., Zheng, C., & Yang, J. (2021). Heat transfer rate characteristics of two-phase closed thermosyphon heat exchanger. Renewable Energy, 177, 397-410.

[23]   Sarmiento, A. P. C., Milanese, F. H., Mantelli, M. B. H., & Miranda, V. R. (2020). Theoretical and experimental studies on two-phase thermosyphon shell and shell heat exchangers. Applied Thermal Engineering, 171, 115092.

[24]   Esen, M and Esen, H., Experimental investigation of a two-phase closed thermosyphon solar water heater, Solar Energy, 79(5), 459-468 (2005).

[25]   Esen, M, Thermal performance of a solar cooker integrated vacuum-tube collector with heat pipes containing different refrigerants, Solar Energy, 76(6), 751-757 (2004).

[26]   J.P. Holman, Experimental methods for engineers, McGraw-Hill Education, Boston, MA, United States, 2011.

[27]   Groll, M; and Rösler, S., Operation Principles and Performance of Heat Pipes and Closed Two-Phase Thermosyphon, Journal of Non-Equilibrium Thermodynamics, 17, p 91-151, 1992.

[28]   Kaminaga, F., Hashimoto, H., Feroz, C., Goto, K., and Matsumara, K., Heat Transfer Characteristics of Evaporation and Condensation in a Two-Phase Closed Thermosyphon, in Proc. of 10th Int. Heat Pipe Conf., Stuttgart, Germany, pp. 1–6, 1997.

[29]   Nusselt , W., . Die oberflachenkondensation des wasserdamphes. VDI-Zs, v. 60, p. 541, 1916.

[30]   Shah, R. K., and A. L. London. Laminar flow forced convection in ducts, in: Adv. Heat Transf. Irvine, T.; Hartnett, J.P, 1978: p.482.

[31]   Muzychka, Y. S., and M. M. Yovanovich. "Laminar forced convection heat transfer in the combined entry region of non-circular ducts." J. Heat Transfer 126.1 (2004): 54-61. https://doi.org/10.1115/1.1643752

[32]   Gnielinski V. (2010) G1 Heat Transfer in Pipe Flow. In: VDI e. V. (eds) VDI Heat Atlas. VDI-Buch. Springer, Berlin, Heidelberg. https://doi.org/10.1007/978-3-540-77877-6_34

[33]   Sarmiento, A. P. C., Soares, V. H. T., Milanez, F. H., & Mantelli, M. B. H. (2020). Heat transfer correlation for circular and non-circular ducts in the transition regime. International Journal of Heat and Mass Transfer, 149, 119165. https://doi.org/10.1016/j.ijheatmasstransfer.2019.119165

[34]   Petukhov, B. S. (1970). Heat Transfer and Friction in Turbulent Pipe Flow with Variable Physical Properties. Advances in Heat Transfer, 503–564. doi:10.1016/s0065-2717(08)70153-9

[35]   Bhatti, M. S., Shah, R.K., "Turbulent and transition flow convective heat transfer in ducts." Handbook of single-phase convective heat transfer (1987).

[36]   Muzychka, Y. S., and M. M. Yovanovich. "Pressure drop in laminar developing flow in noncircular ducts: A scaling and modeling approach." Journal of Fluids Engineering 131.11 (2009).

[37]   A.P.C. Sarmiento, F.H. Milanez, M.B.H. Mantelli, Theoretical models for compact printed circuit heat exchangers with straight semicircular channels, Applied Thermal Engineering, Volume 184, 2021, 115435, ISSN 1359-4311.

[38]   Filonenko, G. K. "Hydraulic resistance in pipes.", Teploenergetika 1 (1954): 40-44.

[39]   Colebrook, C. F, "Turbulent flow in pipes, with particular reference to the transition region between the smooth and rough pipe laws", Journal of the Institution of Civil engineers, 11, 1938-39, pp. 133 – 156.

[40]   Robinson, A. J., Smith, K., Hughes, T., & Filippeschi, S. (2020). Heat and mass transfer for a small diameter thermosyphon with low fill ratio. International Journal of Thermofluids, 1, 100010. https://doi.org/10.1016/j.ijft.2019.100010

[41]   Pabón, N. Y. L., Mera, J. P. F., Vieira, G. S. C., & Mantelli, M. B. H. (2019). Visualization and experimental analysis of Geyser boiling phenomena in two-phase thermosyphons. International Journal of Heat and Mass Transfer, 141, 876-890. https://doi.org/10.1016/j.ijheatmasstransfer.2019.06.052

[42]   Smith, K., R. Kempers, and A. J. Robinson. "Confinement and vapour production rate influences in closed two-phase reflux thermosyphons Part A: Flow regimes." International Journal of Heat and Mass Transfer 119 (2018): 907-921. https://doi.org/10.1016/j.ijheatmasstransfer.2017.10.049

3. Heat transfer and pressure drop correlations of circular offset strip fins heat transfer geometry for compact heat exchangers

Nomenclature

A	=	heat transfer area, [m^2]
A_o	=	minimum free-flow cross section area, [m^2]
A_w	=	heat conduction area, [m^2]
C	=	flow stream capacity rate, [W/K]
c_p	=	specific heat of fluid at constant pressure, [J/kg]
Dh	=	hydraulic diameter, [m]
d_c	=	channel diameter, [m]
f	=	Fanning friction factor, [-]
G	=	mass velocity based on the minimum free area, [kg/m^2]
h	=	heat transfer coefficient, [W/m²]
h_r	=	fin height, [m]
j	=	Chilton-Colburn factor, [-]
k	=	distancing factor, [-]
k_w	=	fluid thermal conductivity, [W/m.K]
L	=	heat exchanger core length, [m]
l	=	fin length or unitary cell length, [m]
$\dot{m}$	=	mass flow rate, [kg/s]
N	=	Number of channels, [-]
Nu	=	Nusselt number, [-]
Pr	=	Prandtl number, [-]
s	=	transverse space, [m]
T	=	temperature, [K]
t	=	fin thickness or gap between two holes, [m]
U	=	overall heat transfer coeficient, [W/m²]
ε	=	Effectiveness, [-]
η	=	Fin efficiency, [-]
μ	=	fluid dynamic viscosity, [Pa . s]
ρ	=	fluid density, [kg/m^3]

Subscripts

a	=	air
c	=	circular
cp	=	Constant properties
i	=	inlet
m	=	mean
o	=	outlet
r	=	rectangular
v	=	vapor
w	=	wall

3.1 Introduction

Compact heat exchangers (CHE) are very-known devices present in most varied thermal cycle setups, from residential air- conditioning system to a nuclear power plant. Their function is to allow an efficient heat transfer from one medium to another. The classification of compact

refers to a category with a large heat transfer area per unit volume of the exchanger, this is, the heat transfer surface area density greater than about 700m^2/m^3 or a hydraulic diameter $D_h \leq 6$ mm for operating in a gas stream and 400m^2/m^3 or higher for operating in a liquid or phase-change stream [1]. They are also classified according to the construction method, which each type is preferred for a particular application, always exposing the fluids to a heating or cooling condition through a high area. The heat transfer surface can vary from a simple flat plate to a complex porous media matrix. The evolution of these devices over time has led to an increase in the surface area/volume ratio and lightweight, in addition to reducing: space, support structure, footprint, energy requirements and costs [1]. The manufacturing technology available is one of the key constraints to the creation of enhanced heat transfer surfaces for the compact heat exchanger cores.

The internal geometry of the heat exchanger core where fluids are forced to flow can assume different forms depending on the fluid application and the flow conditions. The exchanger core design is made to maximize heat transfer rate and minimize the friction-power expenditure as much as possible. For all fluids, the heat transfer rate per unit of surface area increases with the fluid-flow velocity at the first power of the velocity. In the meantime, the friction-power expenditure also increases with the flow velocity, but in this turn, the power rises to the cube of the velocity and never less than the square [2]. For low-density fluids, such as gases, friction-power expenditure tends to be high. To reduce the friction-loss, the gas-flow velocities should be reduced by increasing the number of flow passages, which also reduces the heat transfer rate per unit of surface area. Thus, large amounts of surface area are necessary to counteract the limited heat transfer rates in gas-flow heat exchangers. Plate-fin, tube-fin, and regenerators are examples of compact heat exchangers with high surface area density used for gas flow on one or both fluid sides.

In a plate-fin heat exchanger (PFHE), extended surfaces are used to increase the heat transfer surface area and overcome the thermal conduction deficiency of the gases. There are a variety of plate-fin surface types used for diverse applications: plain fins, louvered fins, offset strip fins, wavy fins, pin fins, and perforated fin. The literature presents correlations and predictive models of heat transfer and pressure drop for many of these complex geometries [2], which are often employed in the design of heat exchangers. Though the compact heat exchanger types, the plate-fin are high-performance surfaces often used in several high efficiency components such as recuperators. Among all, recent investigations are focused on the design of high effectiveness heat exchangers using the offset strip fins heat transfer geometry and on the performance improvement attained with its dimensional variations [3]-[7].

One of most used fin geometries applied in plate-fin heat exchangers is the rectangular offset strip fin (rOSF). This heat transfer surface has a rectangular cross section into short flow-length strips fin, which are used to detach the boundary layer and consequently improve the heat transfer performance at a given flow velocity. The use of interrupted fins results in a flow configuration where the boundary layer is never fully developed, favoring high heat transfer rates. The interruptions also increase the friction, but the increment in the heat transfer rate is advantageous relating to the small increase in friction [2]. Over decades the rOSF was object of deep study [8]-[11]. A complete literature review is presented including heat transfer and pressure drop power law correlations of Colburn factor j and Fanning friction factor f were suggested in terms of the dimensionless geometric parameters α, δ and γ (defined in Fig. 3.1) and the of Reynolds number (Re), covering the laminar to turbulent regimes [12]. Attention is continuously paid to this surface geometry, including some modifications and improvements

which are proposed [13][14]. Some thermodynamic optimization methods can be used to design the optimum configuration and dimensions of the fins [15]. However, reproducing the optimum design into the final rOSF exchanger is still the most challenging limitation due to the manufacturing issues, that requires fin folding and brazing process becoming complex and expensive for some applications.

The evolution of the heat exchangers and manufacturing techniques allows the creation of new enhanced heat exchanger core surfaces. Techniques such as printed circuits and additive manufacturing increase the degree of freedom in the geometric aspects of the surfaces being possible to design advanced and enhanced geometries in terms of minimizing thermodynamic irreversibility. The higher precision of the manufacturing techniques also favors the fabrication of smaller flow passages contributing to reduce the hydraulic diameter, which allows to increase the number of flow passages and consequently provides higher heat transfer surface area in the compact heat exchangers. Taking advantage of modern manufacturing techniques, a novel heat transfer surface, similar to the rOSF is proposed in the present study. The novel heat transfer surface has similar geometrical characteristics to the rOSF, being the main difference the cross-section shape of the flow passages, which instead rectangular are circular. Due to that, the geometry will be called circular offset strip fin (cOSF). It can be obtained by staggering a sequence of perforated plates, resulting in a fluid path similar to the one observed in the rectangular configuration. The stacked plates can be joined by diffusion bonding or not, depending on its application. Once the rOSF plate-fin surface is still in used, the new cOSF geometry may be an alternative due to the similar hydrodynamic performance and the possible lower manufacturing cost.

Some potential advantages encourage the use of the novel circular offset strip fins in place of the rectangular offset strip fins. The manufacturing method of the cOSF (stacking perforate plates) doesn't present the contact resistance found in the plate fin rOSF (between the plates and the rOSF matrix). Moreover, in the novel configuration, when joined by diffusion bonding, eliminates the need of brazing, allowing the increase of working temperature of the component and to reduce costs. Moreover, the manufacturing method enable the use of different materials through the stack (bimetallic approach), allowing the use of high temperature materials only on the hot end of the heat exchanger, which would also permit an increase of the working temperature without a considerable increase of cost. In the cOSF the circular fin profile acts as "fillets" which reduces the thermal stress concentration in the fin basis at the exchanger heating and cooling cycles. The resultant diffusion bonded body is more robust than the plate fin heat exchangers which also is favorable to the increase of the working pressure. In addition, the CAD manufacturing methods as CNC digital cutting machines, allow to reproduce with precision the optimum design of the cOSF flow passages, resulting in most efficient heat exchangers, once the fin fold technique used in the rOSF is not so precise. Further cOSF advantages are also discussed in the present work.

Thus, to assess the potential of the new geometry, five diffusion bonded heat exchangers cores containing the cOSF surface inside were manufactured. In each core, the dimensions of the flow passages were varied in order to elucidate the influence of each dimensional aspect in the thermal and hydrodynamic performance of the novel heat transfer structure. The cores were tested using the steam to air, steady state Kays and London technique [16] in a test rig assisted by a two phase thermosyphon to provide the constant wall temperature condition [Chapter 2] [17]. The experimental data were treated using a data reduction method to obtain the heat transfer Nusselt number (Nu) and Chilton Colburn (j) factor and the pressure drop Fanning friction factor (f). From the experimental data, predictive equations are devised

for the new circular geometry. Finally, a performance comparison between the rectangular and circular offset strip fins heat transfer geometries for heat exchanger cores are presented.

3.2 Geometry description and data reduction

In the present section the geometrical aspects and the hydraulic diameter of the cOSF heat transfer geometry are described. In addition, the data reduction method used to access the heat transfer and pressure drop characteristics is detailed, including the temperature dependent property-ratio correction method. The Colburn factor-j and the Fanning friction factor j correlations for the rOSF suggested by [10] is also presented.

3.2.1   Offset strip fin heat transfer surface

The proposed cOSF heat transfer surface can be obtained by a sequence of staggered perforated plates containing offset circular holes arrayed in the flow direction. The resultant cOSF geometry is similar and has the same characteristics of the rOSF configuration. The only difference is the flow passages that are round instead of rectangular, leading to non-uniform cross section fins in the circular case. The circular fin profile is used to have higher efficiency than the rectangular fins, however it also causes a slightly higher obstruction for the flow. The Fig. 3.1, shows a comparison scheme of both geometries, where the upper region shows the rOSF geometrical description and at the bottom there is the cOSF, formed by the two types of perforated plates indicated as A and B, with its respective dimensions. Note that the holes centers of plate A are always in the half distance between the center of the holes of the plate B. Also, plate A always has one perforation less than plate B. The cOSF cores always start and end with plate A type. Due to the geometry's similarity of both surfaces, the base geometric dimensions aspects used in the rOSF characterization were kept facilitating the comprehension and comparison.

In the rectangular offset strip fin configuration, the surface geometry is described by the fin length l_r, height h_r , transverse spacing s_r and fin thickness t_r. The fin offset is considered uniform and equal to a half-fin spacing. The case of non-uniform offset would generate more variables and will not be evaluated on the present study. For the circular geometry the passage width s_r and height h_r of the rectangular form are equal and correspond to the hole diameter denoted by d_c. The circular fin length l_c corresponds to the same passage or fin length for both surfaces. Finally, the fin thickness t_c, for the circular geometry represents only the offset distance, or the gap between two holes due the circular configuration, the cross-sectional fin thickness is not uniform. In both geometries the dimension c is the wall conduction thickness. Some dimensionless parameters were defined to access the influence of the surface proportions on the heat transfer and pressure drop of the rOSF core; $\alpha_r = s_r/h_r$, $\delta_r = t_r/l_r$, and $\gamma_r = t_r/s_r$ [10]. The same dimensionless parameters were also kept in the present study for the cOSF geometry: $\alpha_c = d_c/d_c = 1$, $\delta_c = t_c/l_c$, and $\gamma_c = t_c/s_c$. The circular geometry implies that the alpha factor is unitary, because the height and width of the circular flow channels are equal to the passage diameter.

rectangular offset strip fins (rOSF)

$\alpha_r = s_r/h_r$
$\delta_r = t_r/l_r$
$\gamma_r = t_r/s_r$

$\alpha_c = d_c/d_c = 1$
$\delta_c = t_c/l_c$
$\gamma_c = t_c/d_c$

circular offset strip fins (cOSF)
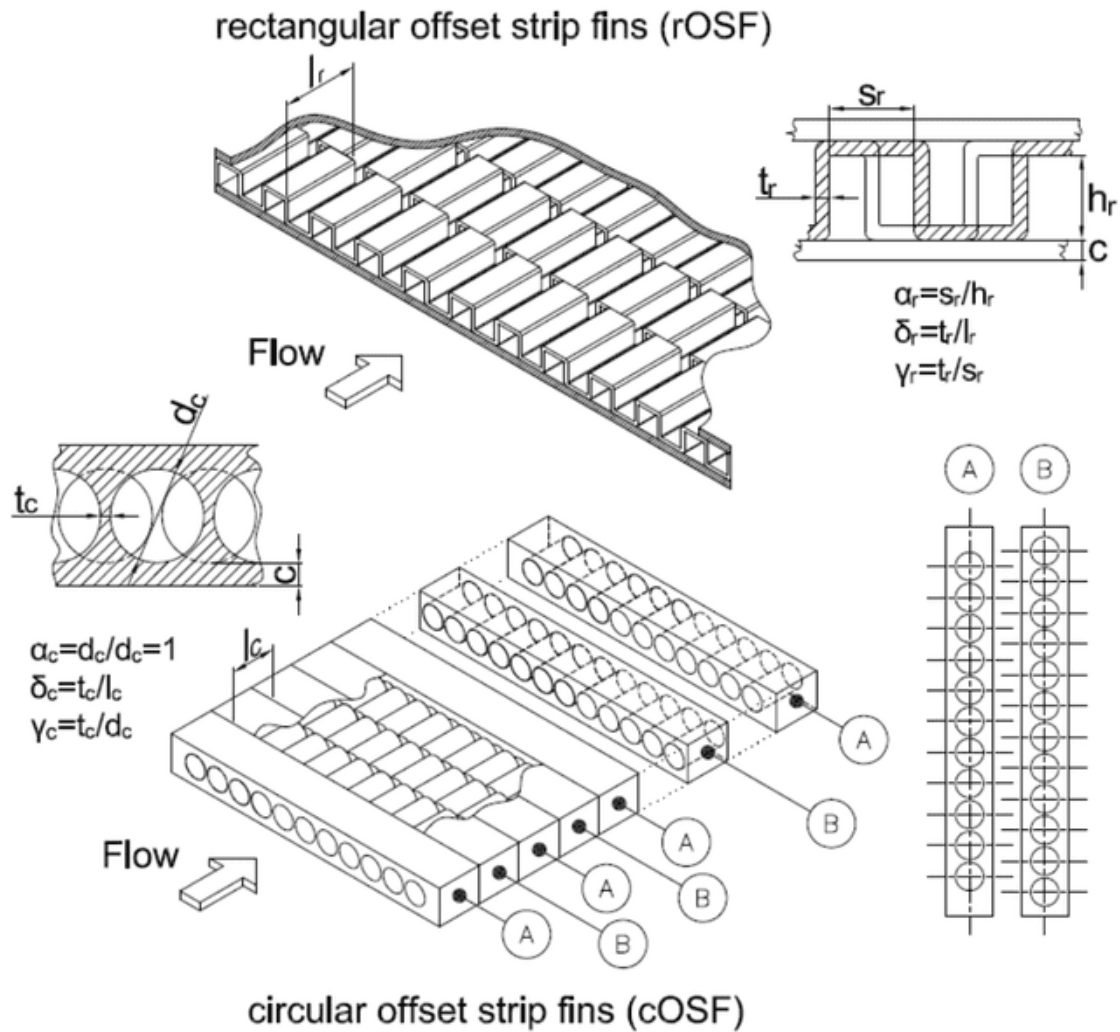
Figure 3.1 - Geometrical description of rectangular and circular offset strip fin heat transfer geometries.

3.2.2 Hydraulic diameter

The hydraulic (or equivalent) diameter D_h by its definition is

$$D_h = \frac{4A_o}{A/l} \tag{1}$$

Where A_o is the minimum free-flow cross section area, A is the heat transfer or the fluid wet area and l is the unitary cell length. Fig. 3.2 presents the dimensional characteristics of the cOSF. Only the fluid volume of the interior of cOSF geometry is plotted to facilitate the visualization. The unitary element, which is the cell that is repeated several times inside the heat exchanger core is evidenced with its respective dimensions. Note that only the uniform offset pattern was evaluated, which means that the holes are always centered at half distance between the two holes of the next row.
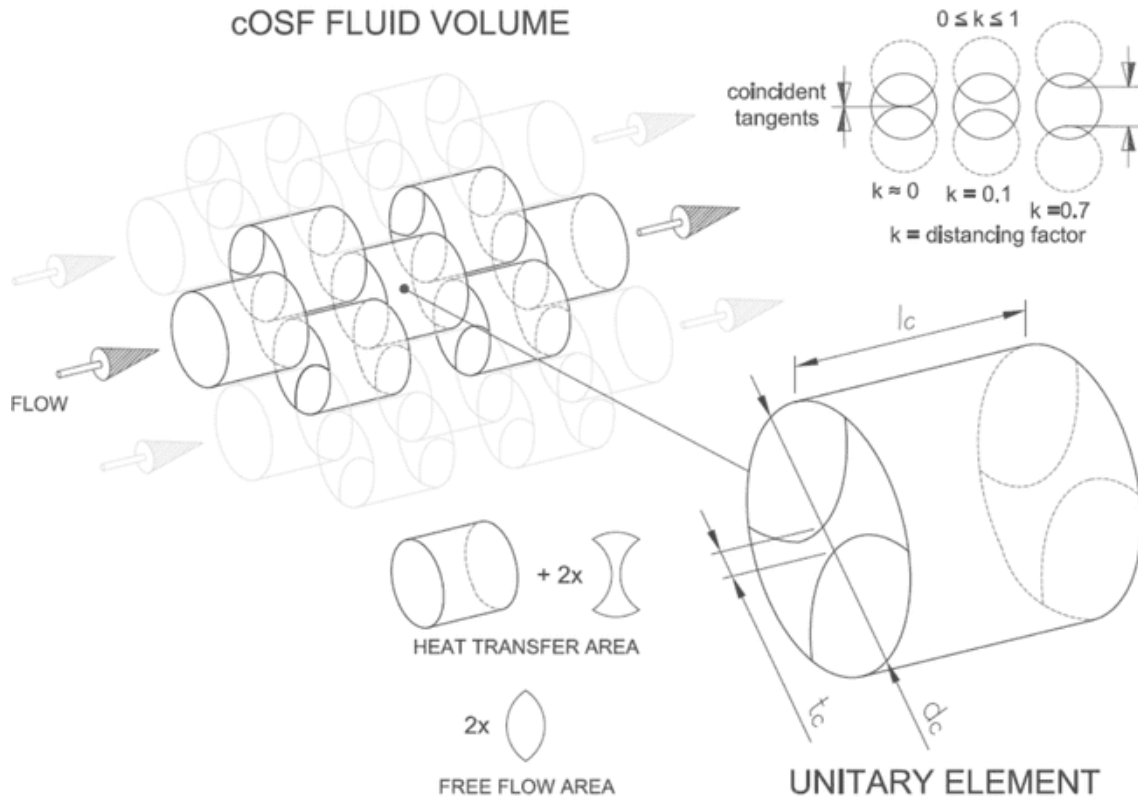
Figure 3.2 –Fluid volume and dimensional characteristics of the circular offset strip fin geometry.

Each unitary element has four communication passages, two entrances and two exits, formed by the circle intersections. The sum of the two intersections characterizes the minimum free-flow cross section area, A_o. The tangential distance between the holes is denoted by t_c. An additional variable k, which varies from 0 to 1 $(0 < k < 1)$, was implemented to characterize the passages obstruction degree. When k is equal to zero, $k = 0$, the circles tangents are coincident, and the passages has the minimum obstruction. The opposite occurs when k is unitary, $k = 1$, leading to the complete obstruction of the passages. The obstruction degree visualization is present in the top right of the same figure. The tangential hole distances t_c can be obtained by the following equation

$$t_c = kd_c \tag{2}$$

The minimum free-flow cross section area of each unitary element can be computed by,

$$A_o = d_c^2 \left[\cos^{-1}\left(\frac{1+k}{2} \right) - \frac{1+k}{2} \sqrt{1 - \frac{(1+k)^2}{4}} \right] \tag{3}$$

The heat transfer area A, of the unitary element is composed by the cylinder shell area and two times the fin frontal area, formed by the area of the hole diameter minus the free-flow area A_o. The offset strip fins have leading and trailing edges at each strip, which contribute to the heat transfer area resulting to a heat transfer area which can be computed by:

$$A = \frac{\pi d^2}{2} + \pi l_c d_c - 2A_o \tag{4}$$

The mass flow averaged velocity on each channel can be obtained by $G = \dot{m}/NA_o$, where $\dot{m}$ is the total mass flow rate and N is the number of holes in which the flow is divided in the first plate of the staggered sequence. Actually, the free passage area encountered by the flow in the first plate is the round circle with diameter d_c. Nevertheless, it was still considered as the circle's intersections area, which corresponds to the minimum free-flow area [2]. This assumption results in a mass flow velocity sensible to the channels obstruction degree. In addition, assuming all channels are uniform and have the same proportions, the flow is divided evenly between the holes, where, by definition, the Reynolds number based on the hydraulic diameter is denoted by,

$$\mathrm{Re}_d = \frac{GD_h}{\mu} = \frac{4\dot{m}l}{NA\mu} \tag{5}$$

where μ is the dynamic viscosity.

3.2.3   Data reduction and temperature-dependent fluid properties correction

The steady state steam-to-air Kays and London Technique [16] was used to obtain the experimental data and determine the airside heat transfer Chilton-Colburn $\dot{j}$, and Fanning friction factor, f in function of the Reynolds number. For that, a compact heat exchanger coupled to a two-phase thermosyphon was used to determine the heat transfer characteristics of the new surface [Chapter 2]. One side of the exchanger core was subjected to water vapor condensation at a specified temperature T_v (hot fluid), to keep the wall temperature T_w constant, leading to $T_w = T_v$, while in the other side, air (cold fluid) was forced through the cOSF surface. In this configuration, the air side has the controlling thermal resistance, which means a capacity rate ratio equal to

$$C^* = C_{\min}/C_{\max} = 0 \tag{6}$$

Where, the capacity rates for the air and the steam side respectively are,

$$\begin{aligned} C_{\min} = C_a = \left(\dot{m}c_p\right)_a \\ C_{\max} = C_v = \left(\dot{m}c_p\right)_v \end{aligned} \tag{7}$$

For this configuration, from an energy balance in a control volume at the air side of the heat exchanger and idealizing a local overall heat transfer coefficient U_a uniform throughout the core, it can be evaluated from the number of transfer units,

$$U_a = \frac{C_a NTU}{A_a} \tag{8}$$

Also, for this configuration, is possible to apply the relation of

$$\frac{T_v - T_{a,o}}{T_v - T_{a,i}} = e^{-NTU} = 1 - \varepsilon \qquad (9)$$

For which in the left-hand side, $T_{a,i}$ and $T_{a,o}$ are the air flow temperature just before and after its passage through the heat exchanger. For the right-hand side, the term $(1 - \varepsilon)$ is the heat exchanger ineffectiveness, which for this configuration is

$$\varepsilon = \frac{T_{a,o} - T_{a,i}}{T_v - T_{a,i}} \qquad (10)$$

Thus, the air side film coefficient, h_a, can be computed from the overall thermal resistance considering three components in series: (1) air-side thermal resistance; (2) wall thermal resistance; and (3) steam-side thermal resistance. Since the steam-side component is around two orders of magnitude bigger than the air-side thermal resistance [Chapter 2], it can be neglected resulting in a constant wall temperature condition denoted by:

$$h_a = \frac{1}{\eta_{o,a}} \left(\frac{1}{U_a} - \frac{A_a t_w}{A_w k_w} \right)^{-1} \qquad (11)$$

Where the wall thickness is t_w, A_w is the overall heat conduction cross-section area, which in the present case is equal to the vapor side area A_v, k_w represents the material thermal conductivity and $\eta_{o,a}$ is the air-side fin efficiency, which for the cOSF heat transfer surface refers to a semi-circular profile fin with non-uniform cross-sectional area. The efficiency solution for this kind of fin is not trivial. Thus, the fin efficiency of a parabolic fin profile, which is very similar, was applied for simplicity

$$\eta_{cOSF} = \frac{2}{\left[4 \left(m \, d_c / 2 \right)^2 + 1 \right]^{1/2} + 1}$$

$$m = \left[\frac{4 h_a}{k_w \left(d_c + t_c \right)} \right]^{1/2} \qquad (12)$$

All the air properties are evaluated at the log-mean average temperature

$$T_{a,lm} = T_v - \Delta T_{lm} \qquad (13)$$

Where

$$\Delta T_{lm} = \frac{\left(T_v - T_{a,i} \right) - \left(T_v - T_{a,o} \right)}{\ln \left[T_v - T_{a,i} / T_v - T_{a,o} \right]} \qquad (14)$$

Finally, the Colburn factor and the Nusselt number can be evaluated by their definition

$$Nu_{D_h} = \frac{h_a D_h}{k_a} \qquad (15)$$

And

$$j = \frac{h_a \, \mathrm{Pr}^{2/3}}{\left(Gc_p\right)_a} \tag{16}$$

The friction factor is evaluated directly from the following equation

$$f = \frac{D_h}{2L} \frac{1}{\left(1/\rho\right)_m}\left[\frac{\Delta p}{G^2} - \left(\frac{1}{\rho_o} - \frac{1}{\rho_i}\right)\right] \tag{17}$$

In this case, the entrance and exit core effects were included in the total friction factor, once its constants values are unknown for the new cOSF geometry. For interrupted surfaces with highly turbulent flow this assumption may lead to a small increase in the pressure drop, in comparison with the major contribution of core friction pressure drop [17]. In the Eq. 17, L is the total length of the heat exchanger core. The term Δp is the differential pressure drop. ρ_i and ρ_o are the fluid densities at the inlet and outlet temperatures respectively, and ρ_m is the mean fluid density $1/\rho_m = 0.5\left(1/\rho_i + 1/\rho_o\right)$. The proposed cOSF heat transfer geometry can be used in different applications including high temperature levels. In this case, the fluid temperatures, and consequently the fluid properties, can vary significantly requiring some kind of temperature correction. The properties-ratio method [2] is extensively used to take into account the fluid property variations in the heat exchanger, which for gases is given by

$$\frac{Nu}{Nu_{cp}} = \left(\frac{T_w}{T_m}\right)^n \tag{18}$$

$$\frac{f}{f_{cp}} = \left(\frac{T_w}{T_m}\right)^m \tag{19}$$

Here, the subscript cp refers to the constant property variable, and T_w/T_m is absolute temperatures ratio. The value of the exponents n and m are the ones which minimize the data dispersion at generated at different wall temperatures. For the novel cOSF geometry the exponents n and m are unknow. Thus, the values defined for round pipes for airflow at a heating condition were evaluated for the present case. Further details are discussed in Section 3.4.

The use of power law expression was explored by many authors to describe the hydrodynamic and thermal characteristics of the rOSF. The f and j in function of the dimensionless parameters, Reynolds number, α, δ and γ follow constant-slope log-linear lines in both, deep laminar and fully turbulent flow regions [10]. The same expression structure was kept to the cOSF geometry. The aspect ratio term, α, is unitary in the circular geometry, reducing the expressions as follows

$$f = A\,\mathrm{Re}^{a1}\left(\alpha\right)^{a2}\left(\beta\right)^{a3}\left(\gamma\right)^{a4} = A\,\mathrm{Re}^{a1}\left(\beta\right)^{a3}\left(\gamma\right)^{a4} \tag{20}$$

$$j = B\,\mathrm{Re}^{b1}\left(\alpha\right)^{b2}\left(\beta\right)^{b3}\left(\gamma\right)^{b4} = A\,\mathrm{Re}^{b1}\left(\beta\right)^{b3}\left(\gamma\right)^{b4} \tag{21}$$

The asymptote-matching method was used to devise the exponents of these form expressions for the novel cOSF. For the case of the rOSF, the generated equations correlate with the experimental data of 18 rOSF cores within +-20%. The correlations to predict the heat transfer and pressure drop on rOFS proposed by [10] are

$$f = 9.6243 \, \mathrm{Re}^{-0.7422} \, \alpha^{-0.1856} \delta^{0.3053} \gamma^{-0.2659}$$
$$\times \left[1 + 7.669 \times 10^{-8} \, \mathrm{Re}^{4.429} \, \alpha^{0.920} \delta^{3.767} \gamma^{0.236} \right]^{0.1}$$

(22)

$$j = 0.6522 \, \mathrm{Re}^{-0.5403} \, \alpha^{-0.1541} \delta^{0.1499} \gamma^{-0.0678}$$
$$\times \left[1 + 5.269 \times 10^{-5} \, \mathrm{Re}^{1.340} \, \alpha^{0.504} \delta^{0.456} \gamma^{-1.055} \right]^{0.1}$$

(23)

3.3 Experimental method

In this section, the experimental facility used to generate the heat transfer and pressure drop data of the cOSF geometry is described, including the thermosyphon test section, device which contains the cOSF geometry core, used to promote the constant wall temperature condition. The experimental procedure and the determination of data uncertainties are also detailed in sequence.

3.3.1 Experimental facility

The experimental data were obtained at the same experimental facility and procedure used in the compact heat exchangers coupled to a two-phase thermosyphon to characterize heat transfer surfaces [Chapter 2]. Fig. 3.3 presents a scheme of the inline experimental setup. All the experiment was designed to provide a continuous, uniform and stable air flow rate at constant temperature at the inlet of the test section. The heat transfer and pressure drop data were measured at the test section, which contains a compact heat exchanger core with air heating in the cOSF "unknown" side at the expense of condensing water vapor on the other side. The water vapor condensation was used to provide the constant temperature condition at the heat exchanger core, a condition necessary to apply the steam-to-air data reduction method presented in the Section 3.2. A thermosyphon was used to provide the water vapor at the known side, where an evaporator was coupled to the heat exchanger core, which works as the condenser section of the thermosyphon. During the experiments, a forced draft air flow rate was controlled by a centrifugal fan, as its temperature is adjusted and kept constant by means of an electric heater and the mass flow rate was measured by a Coriolis mass flow meter. The air flow at a constant mass flow rate and temperature was then led to a long square cross section duct with 50mm inner side and 800mm length for the inlet of the test section. The long duct was intended to develop the air flow, in order to reach the test section as stable and fully (thermal and hydrodynamically) developed. After the passage through the test section, another duct with equal cross section but with 500mm length was placed to lead the air flow to the ambient. The air flow temperatures upstream and downstream of the test section and at the test section core walls were measured by calibrated thermocouples type K. Four at the test section inlet, six in the heat exchanger core walls (3 on each side of the thermosyphon condenser) and other four at the test section outlet. The air differential pressure and the inlet gauge pressure were measured and recorded with pressure transducers at the test section inlet and outlet.
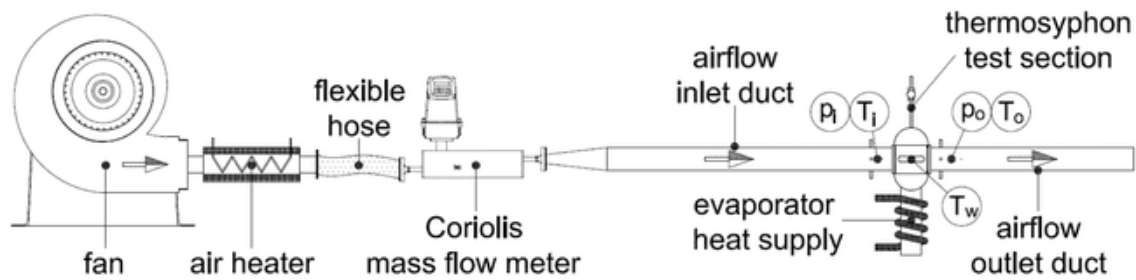
Figure 3.3 - Experimental facility diagram.

3.3.2   Test section

The test section, which is a crossflow heat exchanger core placed at a thermosyphon condenser, is presented in Fig. 3.4. The thermosyphon can be described in two sections, the evaporator, where heat is supplied to the system, and the condenser, which in turn, transfers the heat to the air flux during its passage through cOSF geometry. At the left-hand-side of the figure is a schematic description of the thermosyphon assembly, with the evaporator section on the bottom and the compact heat exchanger condenser section in the upper region. The thermosyphon was charged with water as working fluid, at 90% of filling ratio, which represents the percentual evaporator volume filled with water. With the heat supply in the evaporator section by means of an electric resistance, the working fluid contained inside (water) changes phase to vapor, filling all the thermosyphon interior, as shown in center scheme of the same figure. At the condenser section, the water vapor has contact with the heat exchanger gap walls (vapor passages), which are the "known" side of the heat exchanger core, surface where the condensation occurs. In this configuration, the constant wall temperature condition is established, once the air side has the controlling thermal resistance, since its heat capacity is considerably smaller than the condensing water vapor. The water, back to the liquid phase when condensed, is drained by gravity again to the evaporator section, completing the heat transfer cycle inside the thermosyphon. The cOSF geometry is aligned with the air flow in the x direction, while the thermosyphon is displaced at y axis direction. At the right-hand side of the same figure a picture of one of the five thermosyphon test sections used in the essays is presented (thermosyphon containing the core III in the condenser). Different heat exchanger cores containing different cOSF dimensions and proportions were incorporated in the thermosyphon condenser, to take advantage of the technique and observe the heat transfer and pressure drop influence of each geometrical aspect. The use of the thermosyphon is advantageous as it can provide constant and stable core wall temperatures; different wall temperature levels can be established with accuracy. It is compact and consequently low-cost device and the data obtained in this experiment are clean and stable.
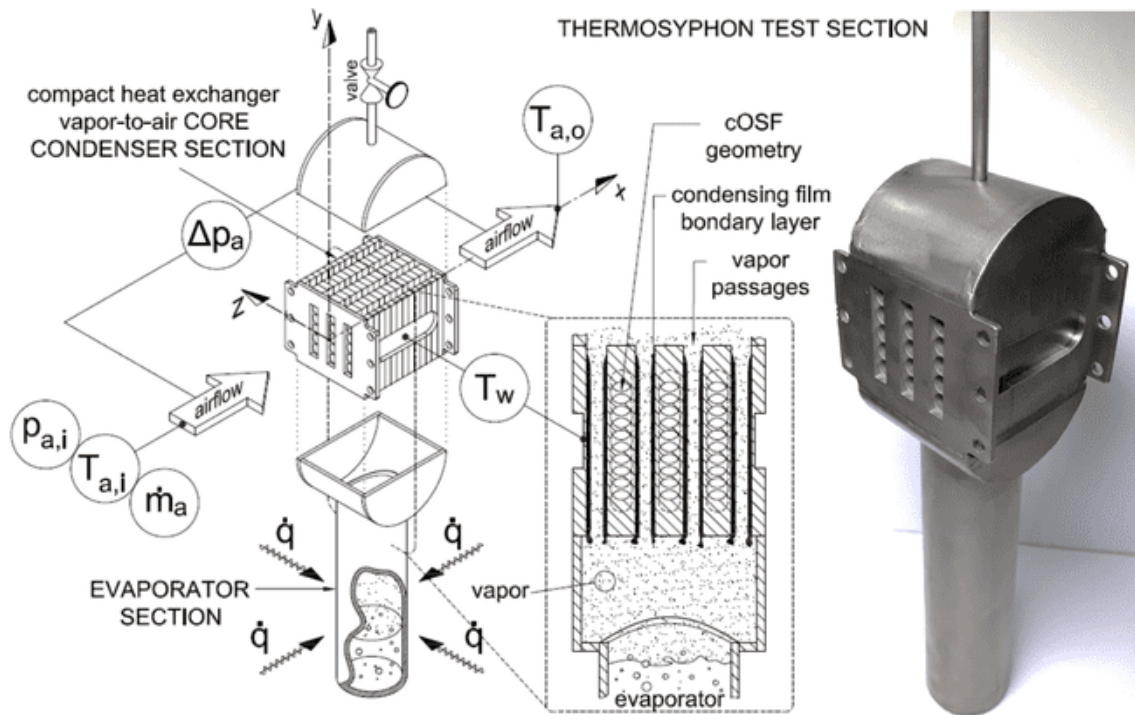
Figure 3.4 – Thermosyphon test section and schematic description (the core III was used as example).

3.3.3 cOSF compact heat exchanger cores

A detailed description of the crossflow compact heat exchanger incorporated in the thermosyphon condenser is presented in Fig. 3.5. The heat exchanger has air heating in the unknown side and water vapor condensation on the know side. The heat exchanger core is formed by a sequence of interspaced plates (plates type A and type B) and 2 face plates "fc" placed on the heat exchanger extremities. The plates type A and B has offset perforations in order to obtain the cOSF geometry when stacked. The sequence of stacked plates was joined by diffusion bonding. The resultant joined body core contains cOSF columns separated by free gaps used to allow the circulation of water vapor. Note that the number of columns n_{col} can vary depending on the cOSF hydraulic diameter. All the heat exchanger core is symmetric with respect to the planes xy, xz and yz, with the origin placed in the core center. The air flows through the core in the x direction, while the vapor has contact with the walls and condenses in the y direction. The figure cut view exposes: the gap walls (vapor passages where the condensation occurs), the cOSF heat transfer geometry, the fluid volume of the cOSF (for visualization purposes) and the milled slot, placed in the core side, used to measure the core wall temperatures. Note that two milled slots were made in both sides of the core to reduce the external wall thickness. The resultant wall thickness t is the same conduction thickness used to separate the airflow from the condensing vapor.
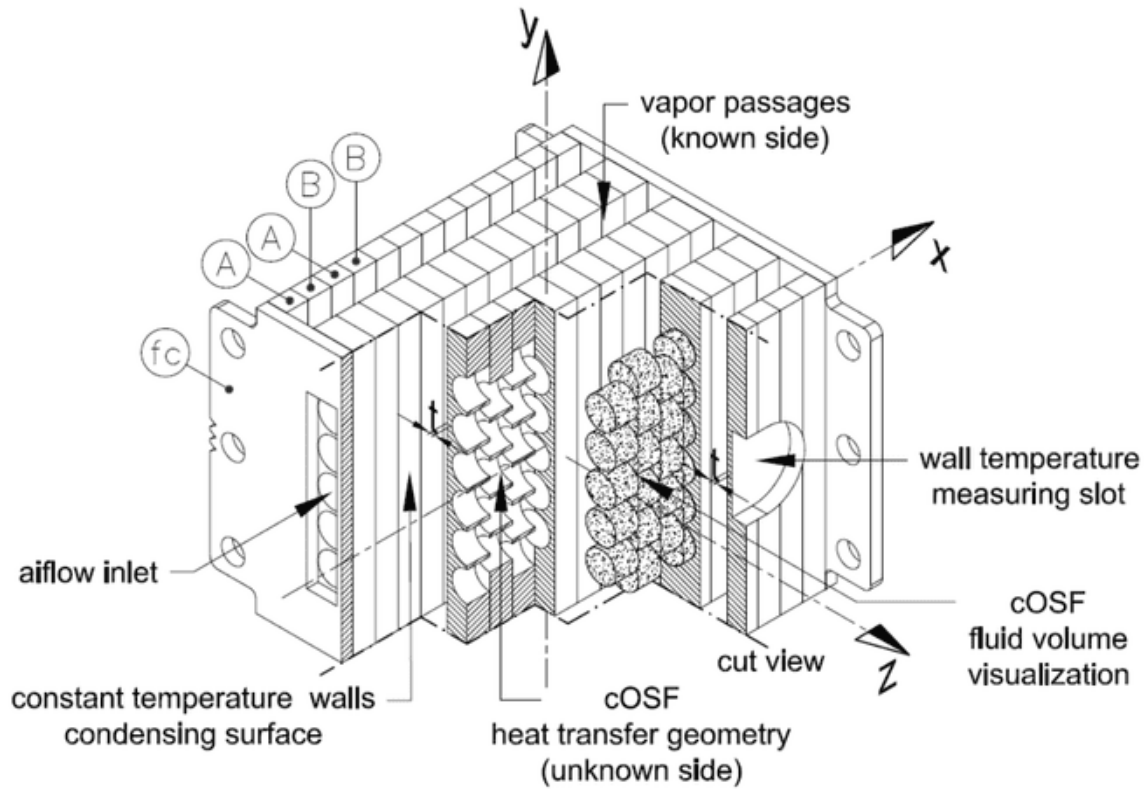
Figure 3.5 - Thermosyphon condenser, vapor-to-air crossflow heat exchanger core (the core III was used as example).

To devise the cOSF pressure drop and heat transfer curves, five different cores containing the circular offset strip fin surface were manufactured and tested with the thermosyphon test section. The cores were produced with five different cOSF proportions as shown in the scaled unitary cell scheme of Fig. 3.6. The figure also shows the assembly of stacking plates for each core and their respective pictures. All cores were manufactured in stainless steel A 316L. The cores II to core V are formed by 7 plates type A and 6 type B with 6mm each and 2 face plates "fc" with 3 mm thickness. The core I has 12 plates type A, 11 plates type B and 2 face plates, all plates with 3 millimeters thickness.
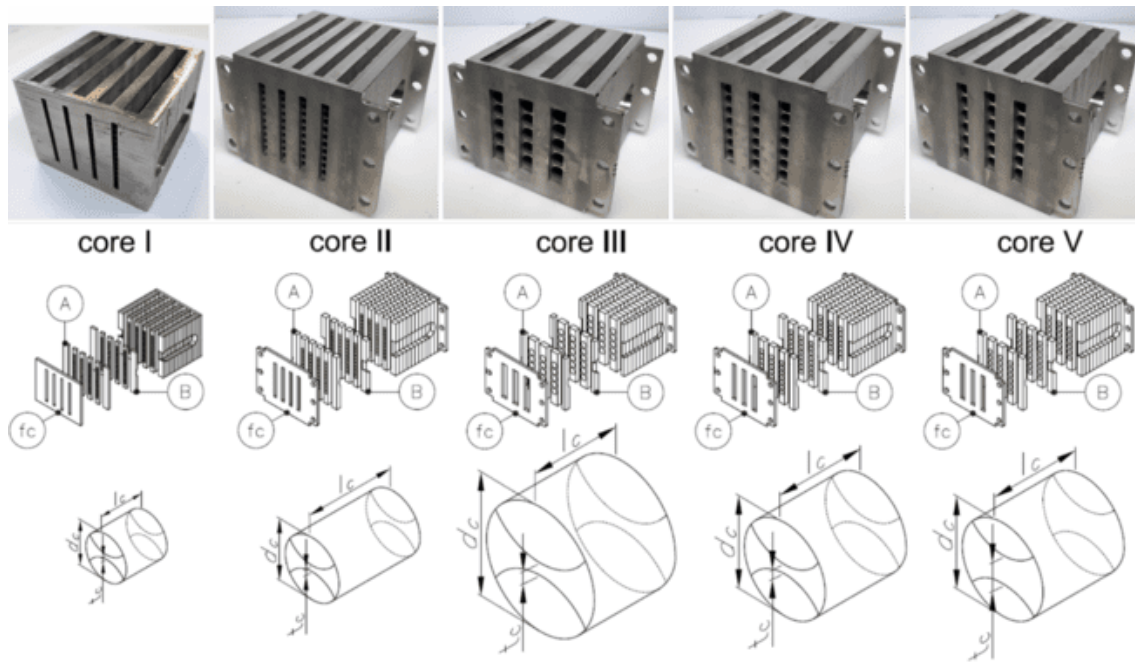
Figure 3.6 – cOSF heat exchanger cores, picture (top), diffusion bonded plates sequence (middle) and scaled cOsf unitary elements (bottom).

The five cores were designed to investigate the influence of each dimensionless parameters δ and γ on the heat transfer and pressure drop of the cOSF surface. The cOSF geometry has 3 degrees of freedom, hole diameter, fin length and the free-low obstruction degree (fin thickness). In each core, two of the three degrees of freedom were kept constant while one was varied to evidence its influence. Back in Fig. 3.6, is a scaled scheme of the unitary element's proportions of each core is shown, to visualize the proportions of cOSF geometries tested. Table 3.1 present the cores dimensions, the dimensionless parameters, the hydraulic diameter and the respective areas calculated with the Eq. 1, Eq. 2 and Eq. 4. The vapor side area A_v which is equal to the wall heat conduction cross sectional area A_w, is given for one individual column and considers both sides of one column. The number of flow passages N (the number of holes contained in the plate A) and the number of columns n_{col} containing the cOSF is also given. The number of vapor passages is equal to $n_{col}+1$. The cOSF columns are always between two vapor columns. Note that the cores have some geometrical similarities to allow the performance comparison. The core I has the same proportions as the core IV, but with half diameter size, to evidence the geometry scaling effect. At the cores I, II, III and IV the parameter gamma was kept constant, while the delta was varied, to evaluate its influence. And finally, the fifth core has the same diameter and length as the core IV, but the distance t was increased, also increasing obstruction degree, to observe its effect.

Table 3.1 - Unitary cell parameters and dimensions.

	Core I	Core II	Core III	Core IV	Core V
D_h [mm]	1.737	2.430	4.428	3.474	2.232
d [mm]	3	4	8	6	6
l [mm]	3	6	6	6	6
t [mm]	0.3	0.4	0.8	0.6	1.8
k	0.1	0.1	0.1	0.1	0.3
$\alpha = d/d$	1	1	1	1	1

$\delta = t/l$	0.1	0.0667	0.134	0.1	0.3
$\gamma = t/s$	0.1	0.1	0.1	0.1	0.3
A_a [mm²]	32.887	83.601	183.603	131.552	143.060
A_o [mm²]	4.762	8.465	33.862	19.047	13.293
A_v [mm²]	6645.6	6801.6	6739.2	7113.6	7020
N	13	10	5	7	6
n_{col}	4	4	3	3	3

3.3.4 Experimental procedure, vapor-to-air tests

The experimental tests were conducted with the same procedure described in [Chapter 2]. The five thermosyphons test sections containing each one a cOSF heat exchanger core were evaluated at the input boundary conditions shown in Table 3.2. During the experiments each airflow rate level was tested at a constant inlet temperature, while the heat exchanger core wall temperature was kept constant by the thermosyphon. The experimental data were recorded in steady-state, characterized by constant mass flow rate, temperatures and pressure readings. It is important to mention that a purge procedure [18] was done before the experiments, in order to "sweep away" to the atmosphere the non-condensable, remaining only the pure water vapor inside the thermosyphon. This procedure stabilizes and makes uniform the thermosyphon wall temperatures. Finally, the measurements of the air-flow rate, airflow temperature upstream and downstream of the test section, the test section wall temperature, and the pressure drop across the test section, together with the considerations of the air side controlling thermal resistance, the pressure losses at the entrance and exit of the core included in the overall pressure drop and the parabolic fin efficiency assumption for the cOSF profile, provide sufficient information for the determination of the Colburn factor-j and the Fanning friction factor f. Together with the Reynolds number, also be determined by using the above measurements, the nondimensional characteristics of the cOSF geometry were determined.

Table 3.2 - Experimental test parameters matrix.

Air inlet temperature	Air mass flow rate [kg/min]	Condenser wall temperature	Test duration
65°C	0.10 0.15 0.20 0.25 0.30 0.35 0.40 0.45	170°C 220°C	300 s

3.3.5 Uncertainties analysis

The experimental uncertainties analysis of the directly measured parameters and the indirect calculations were made considering the systematic errors and random fluctuations of the measuring system and instruments. The considered source of errors was: the test core

dimensions, the data acquisition system and the instruments (thermocouples and the Coriolis mass flow meter). The fluid properties temperature assumption is also a source of error, but in an indirect way. The uncertainties were determined using the methodology presented by [19]. Each core tested presented a slightly different uncertainty, thus, a global uncertainty was assumed to encompass each variable tested. The uncertainties analysis is present in Table 3.3.

Table 3.3 - Uncertainties analysis.

Parameter	Average uncertainties
Temperature	±0.6%
Pressure	±6.3%
Mass flow rate	±0.2%
Reynolds number	±0.2%
Heat transfer rate	±1.3%
Nusselt number	±6.1%
j factor	±7.0%
f factor	±6.8%

3.4 Results and discussions

3.4.1 Data reduction and temperature dependence fluid properties correction

All data obtained in the experimental setup using the procedure described in Section 3.3 were treated with the data reduction method present in the Section 3.2. In addition, due to the high temperature difference between the wall and the mixed mean fluid temperature, the temperature-dependent fluid properties correction given by Eq. 18 and Eq. 19 was applied in all experimental data. Since the cOSF is a new geometry, the exponents "n" and "m" are unknown. The temperature correction factors exponents, "n" and "m" were evaluated with different values for all the thermal and friction data, from the cOSF cores I to V, to identify the ones which provide the lowest data dispersion. The value of n=0 (for the heat transfer) and m=1.8 (for the friction factor) showed the smaller data dispersion with the percentual ratio of the standard deviation to the mean of 1.5 ± 0,7 % and CV%=3.2 ± 1.2% respectively. The literature suggests the values of n=0 and m=1 for fully developed laminar flow of gas at a heating condition on a circular tube [2]. Applying the same value of m=1 in the cOSF data, the dispersion level becomes %CV=4.2 ± 1.9 %, which is close to the minimum value found with m=1.8. Thus, the value of n=0 and m=1, used for circular tube was also selected as the coefficient for the properties ratio method applied for the cOSF. As an example of the data treatment results, the Fig. 3.7 shows the friction factor and Colburn factor obtained for the core II at different Reynolds number. A good data approach is observed, both for Colburn factor and friction factor data generated at different wall temperature conditions. The Colburn factor data was tested twice to reduce random uncertainties in this experiment.
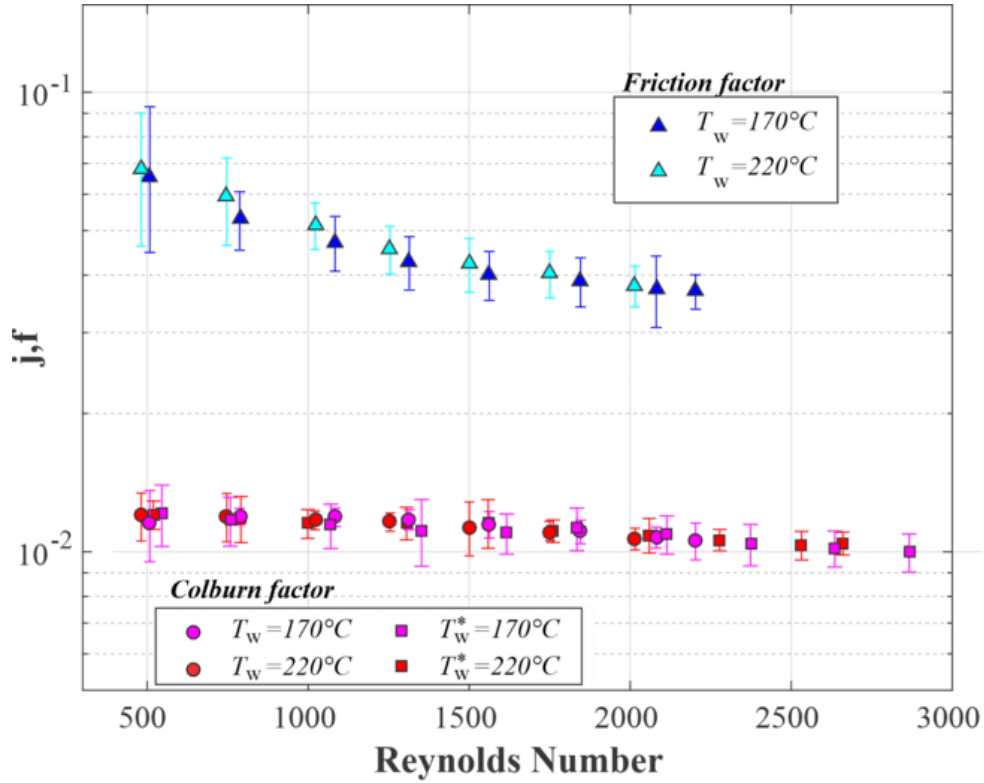
Figure 3.7 - Friction factor and Colburn factor of the Core II, generated at 170 and 220°C wall temperatures and corrected with the Eqs. 18 and 19 with the exponents n=0 and m=1.

3.4.2 cOSF heat transfer and pressure drop correlations

The Colburn factor-j and friction factor f data, for all the 5 cOSF cores tested presented a constant-slope log-linear behavior through all the Reynolds number range analysed. Thus, the experimental data of the cores II, III, IV and V in the range of 500 < Re < 3000 were used to devise correlations to predict the heat transfer and pressure drop in such cOSF cores in function of Re number and the dimensionless geometrical parameters δ and γ. The correlations were obtained based in the Eq. 22 and Eq. 23 form, with the constant values determined by the least-squares method. The least squares regression analysis yielded the following predictive correlations for the cOSF geometry.

$$j = \lambda_j \, \text{Re}^{-0.143} \tag{24}$$

$$Nu = \lambda_j \, \text{Re}^{0.857} \, \text{Pr}^{1/3} \tag{25}$$

$$f = \lambda_f \, \text{Re}^{-0.331} \tag{26}$$

$$\lambda_j = 0.02\left(\delta^{0.02}\gamma^{-0.235}\right) \tag{27}$$

$$\lambda_f = 0.715\left(\delta^{0.279}\gamma^{-0.149}\right) \tag{28}$$

The present Colburn factor (j), Eq. 24, correlate the experimental data within ±6% average error, where 98% of the predictions presents an error lower than 15%. In addition, there is the Fanning friction factor correlation (f), Eq. 26, which correlates the friction data within an

average error of ±8%, where 90% error is lower than 15% and 98% of the error is within 20%. The scatter plots of Figs. 3.7 and 3.8 show the model and the experimental data comparison with their respective error margins. Note that the core I data was not used to devise the correlations, and instead of that, its data was used to validate the devised correlations with experimental results. A few data points are out of the 15% error margins, as indicated with the number 1 in both figures. These points belong to the core I data at low Reynolds number regime, which presented high uncertainties due to the bottom measuring instruments range. Moreover, these points were obtained at a very low air flow rate, which is subject to a to a phenomenon called rollover or drop-off in $\dot{j}$ [16], characterized by a consistently drops off of the j curve with decreasing Reynolds. The error in the measurement of the temperature and air mass flow rate at low Reynolds number may be the reason to cause this effect.
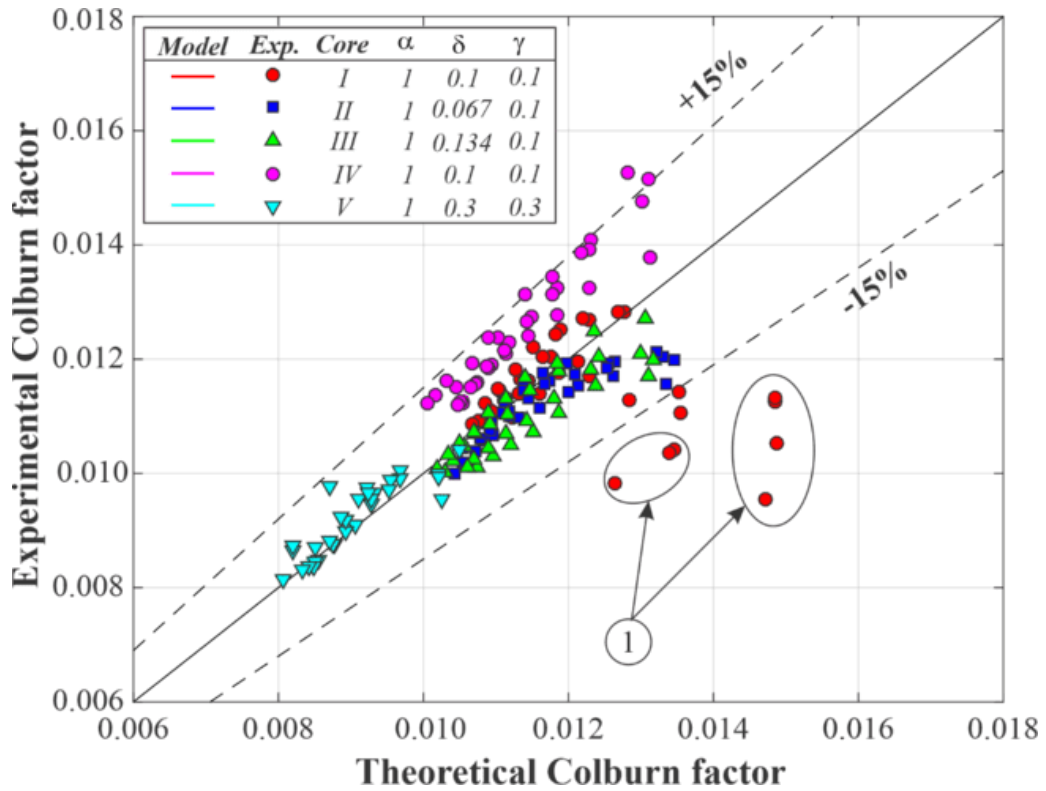
Figure 3.8 - Comparison of predictions for Colburn factor j given by Eq. 24 with the experimental data for circular offset strip fin cores listed in Table 3.1.
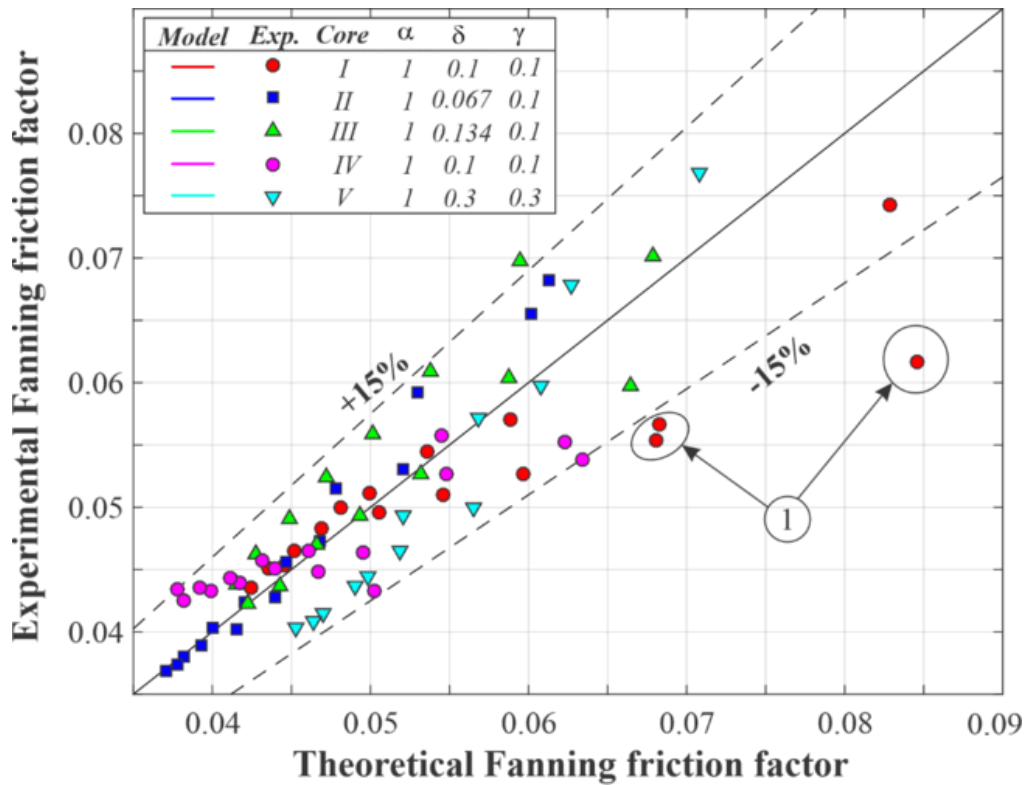
Figure 3.9 - Comparison of predictions for Fanning friction factor f given by Eq. 26 with the experimental data for circular offset strip fin cores listed in Table 3.1.

It was observed a thermal and hydrodynamic characteristic influence for each geometrical dimensionless parameter δ and γ. The combination of geometrical dimensions directly influences the flow pattern and can be used to enhance the heat transfer. The fin thickness, the offset distance and the channel length tend to have a competing influence on the flow field.

Figs. 3.10, 3.11 and 3.12 show the comparison of all experimental data with the devised Colburn factor, Nusselt number and friction factor models, given by the Eqs. 24, 25 and 26, respectively. The five Colburn factor, Nusselt number and Fanning friction factor curves in terms of Reynolds number are plotted, each one for its respective core. Note the curves of the core I and IV are coincident due their proportions δ and γ which are the same. The linear scale was used in the graphs to expose the data with the predictions. For all cores the data showed a continuous behavior not presenting an observable effect on the regime transition, from laminar to turbulent.

From a rough heat transfer analysis at the Figs. 3.10 and 3.11, it is possible to observed that the cOSF cores (I to IV) presented a general similar behavior (considering the error bars) through all the Reynolds range analysed. However, the obstruction degree, parameter γ, represented by the core V, shows a considerable adverse effect in the Colburn factor and Nusselt number curves. Actually, the influence on the heat transfer of the parameter γ is ten times bigger than the parameter δ, showing that the heat transfer is more sensitive to the flow passages obstruction than to the flow passages geometric proportions.

For the pressure drop point of view, presented in Fig. 3.12, the friction factor f is sensible to the flow passages geometric proportions and also to the channel's obstruction degree. It

means that both geometrical parameters δ and γ have considerable influence in the pressure drop. The geometrical influence of each parameter is evaluated in sequence from a comparison of the different aspect cores.
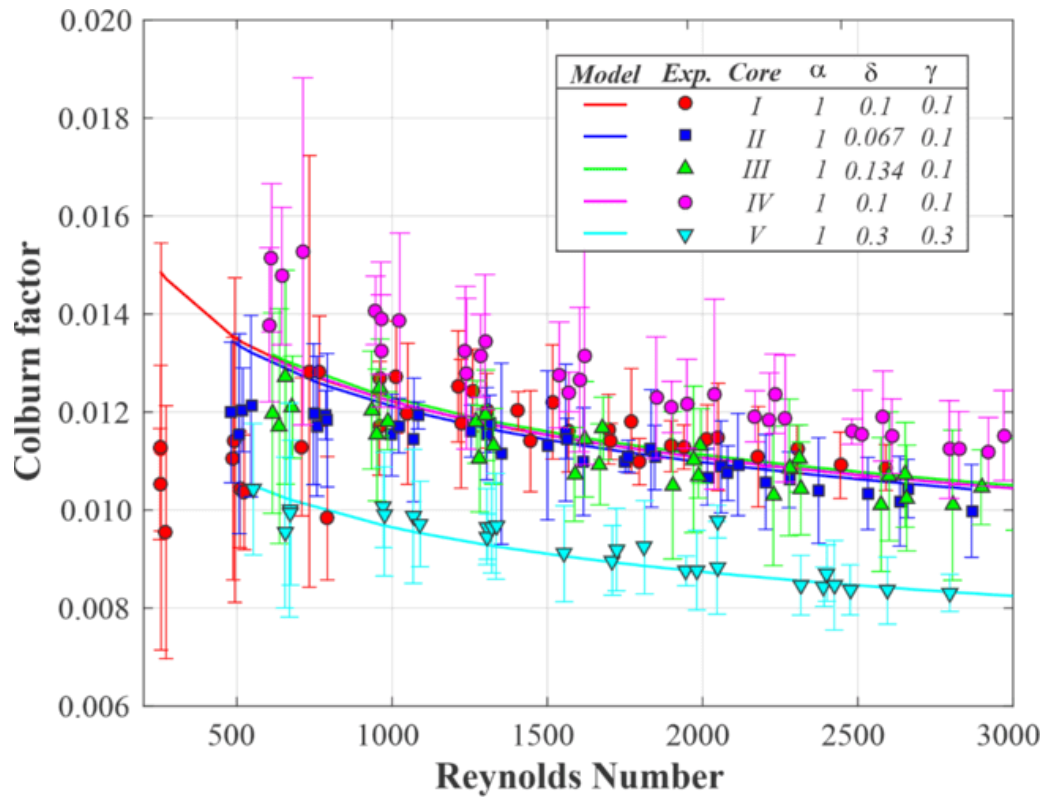
Figure 3.10 - Comparison of predictions from Eq. (24) with experimental data for the cores I to V presented in the Table 3.1.
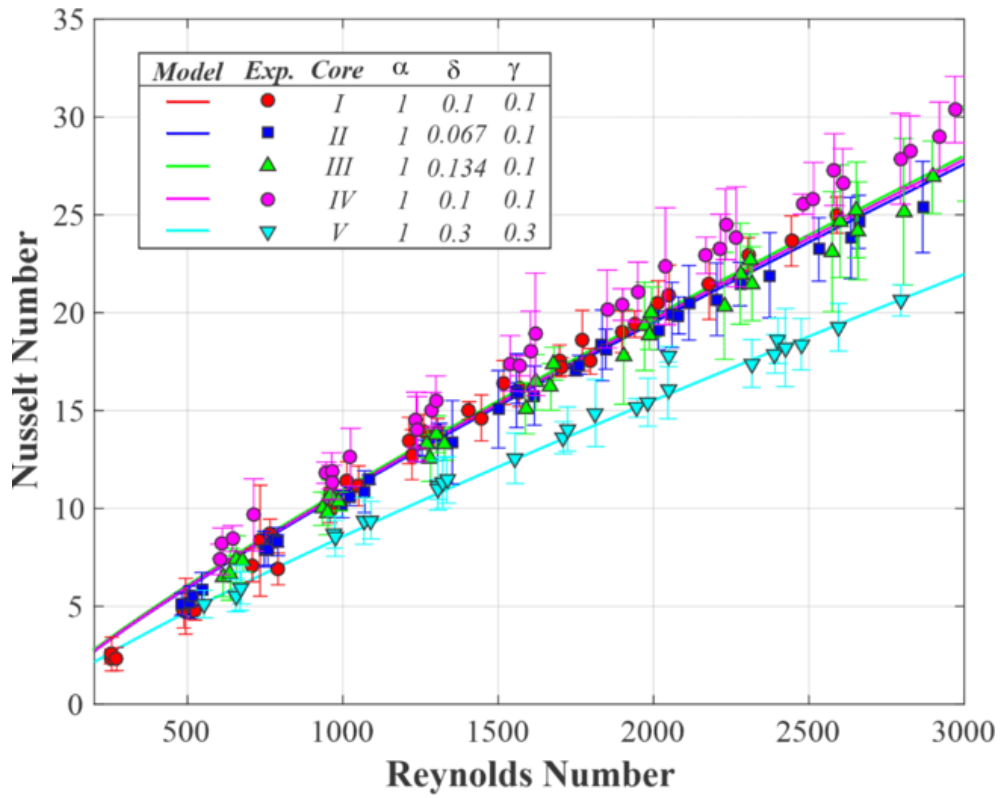
Figure 3.11 - Comparison of predictions from Eq. (25) with experimental data for the cores I to V presented in the Table 3.1.
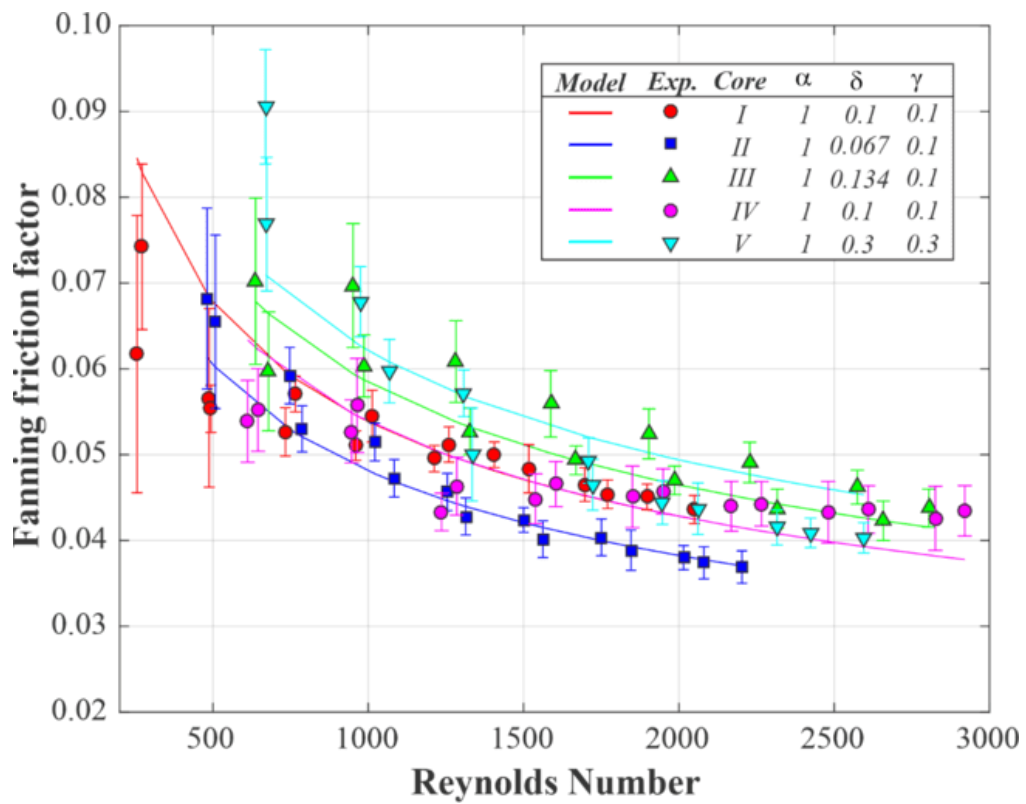
Figure 3.12 – Comparisons of predictions from Eq. 26 with the experimental data for the cores I to V listed in Table 3.1.

70

3.4.3 The influence of the geometrical aspects on the Colburn factor j and friction factor f

First, the influence of the cOSF scaling dimensions is evaluated (Fig. 3.13). For that, the j and f data for the cores I and IV, both with the same dimensionless proportions δ and γ, but the core I with the half hydraulic diameter of the core IV, are compered. The predictions of Eqs. 24 and 26 are also plotted for comparison. The experimental data of the cores I and IV show that the heat transfer and pressure drop are dependent only the dimensionless parameters δ and γ, and independent of the hydraulic diameter. Moreover, the data also agreed well with the proposed correlations. As mentioned before, the core I data were not used to devise the correlation, showing that the model is able to predict the heat transfer and pressure drop of cOSF independent of the geometry scale. The good agreement of the data of the core I with the present model validates experimentally the heat transfer and friction correlations for cOSF. Only some points of the core I data at low Reynolds number are out of the curve trend, which may be related to the rollover phenomena mentioned before.
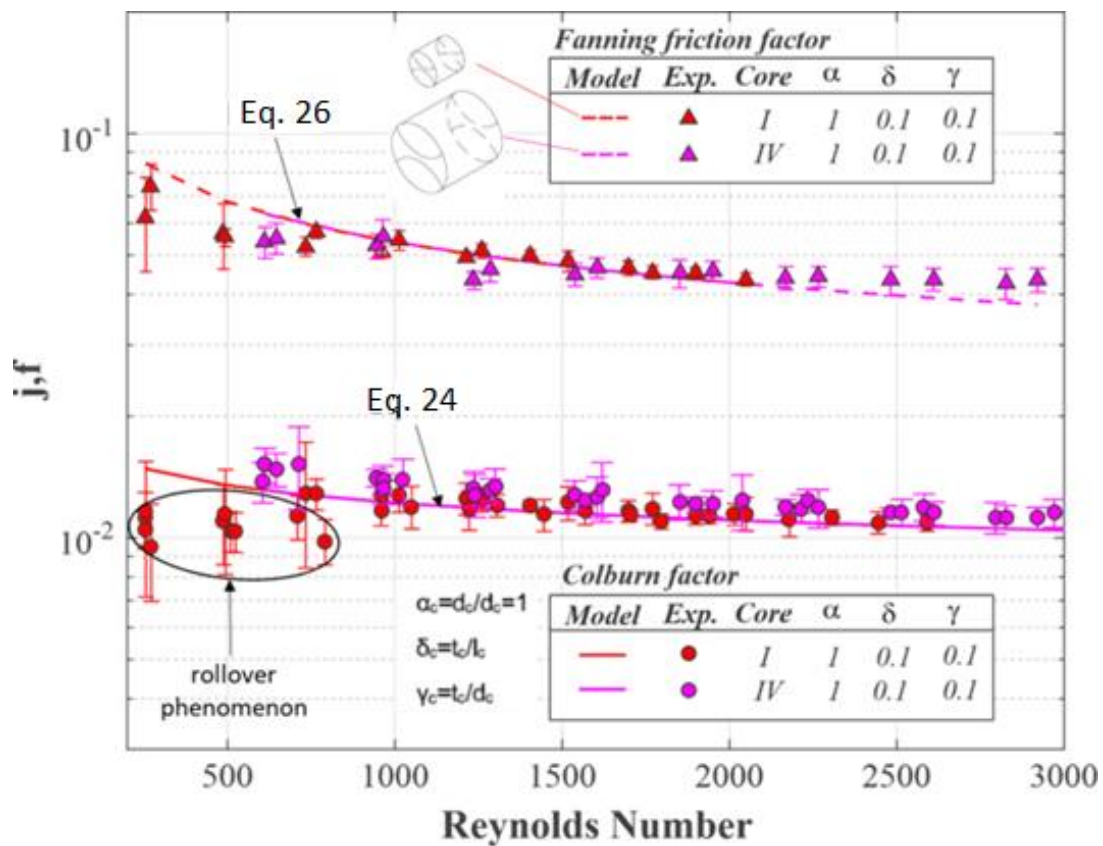
Figure 3.13 – Comparison of cores with the same dimensions but different hydraulic diameters.

In Fig. 3.14, the j and f data for three geometries, all with the same obstruction degree γ but different δ (obstruction degree/thin lengths ratio), are presented, now, separately. It is possible to observe the good agreement of the data with its respective j and f curves given by Eq. 24 and 26. Furthermore, as observed in Figs. 3.10 and 3.11, the parameter δ doesn't have much influence on the Colburn factor and its effect is most on the friction factor.

The influence of the parameter δ in the friction factor is clearly discernible; smaller δ, meaning smaller hydraulic diameter passages with longer lengths ratio means lower friction than the higher flow passages but with short flow developing lengths. It may be related to the higher boundary layer breaking frequency, and its consequent dissipation in the fin wakes caused by the uninterrupted channels. The friction factor increases proportionally from the smaller to the higher δ.
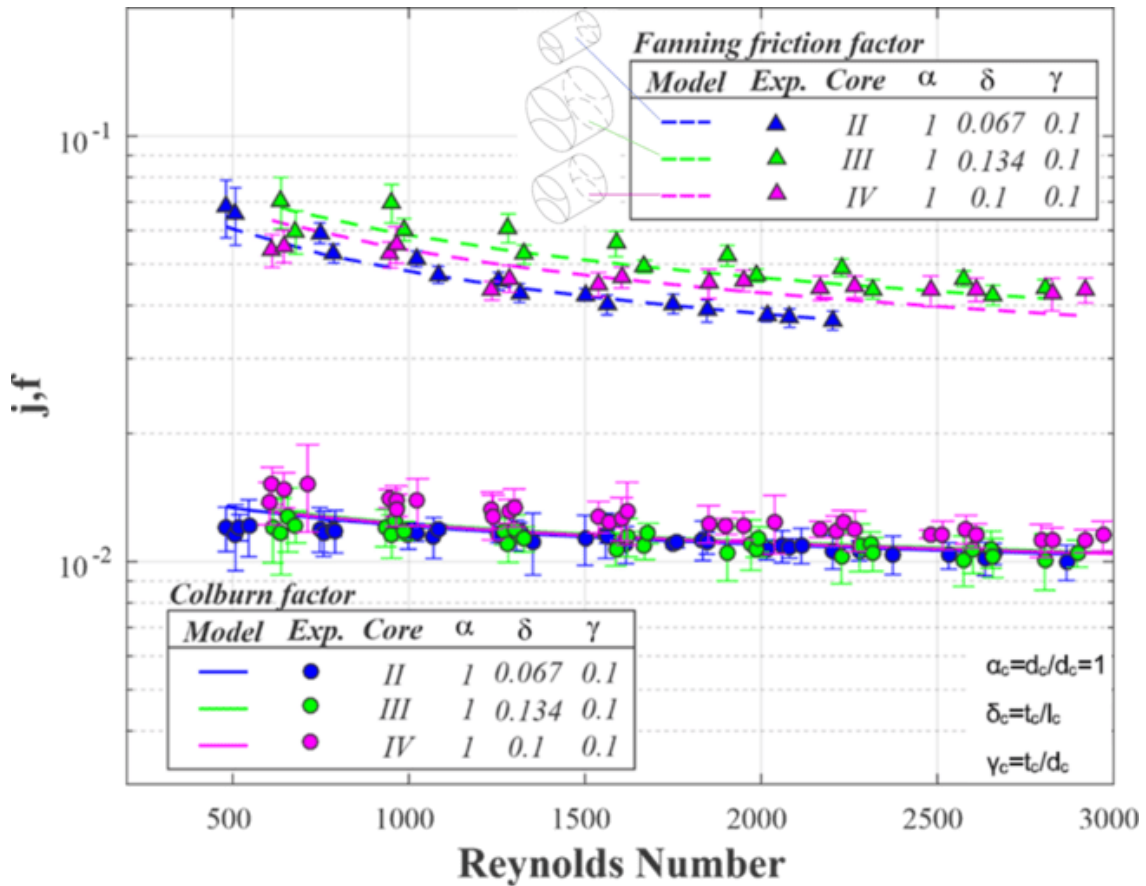
Figure 3.14 - Effect of fin thickness / unitary cell length on the experimental data and f and j curves of Eq. 24 and 26 for the cores II, III, IV of the Table 3.1.

The heat transfer and pressure evaluation of the obstruction degree is presented in Fig. 3.14. To access its effect, the data of the cores IV and V, containing cOSF geometries with the same dimensions but with different obstruction degree (thin thickness) were confronted. The adverse influence of the obstruction degree can be observed in both heat transfer and pressure drop. The core V data presented a higher pressure drop and a small heat transfer characteristics through all Reynolds number range analyzed. Thus, keeping the obstruction degree as small as possible is beneficial to the cOSF overall performance.
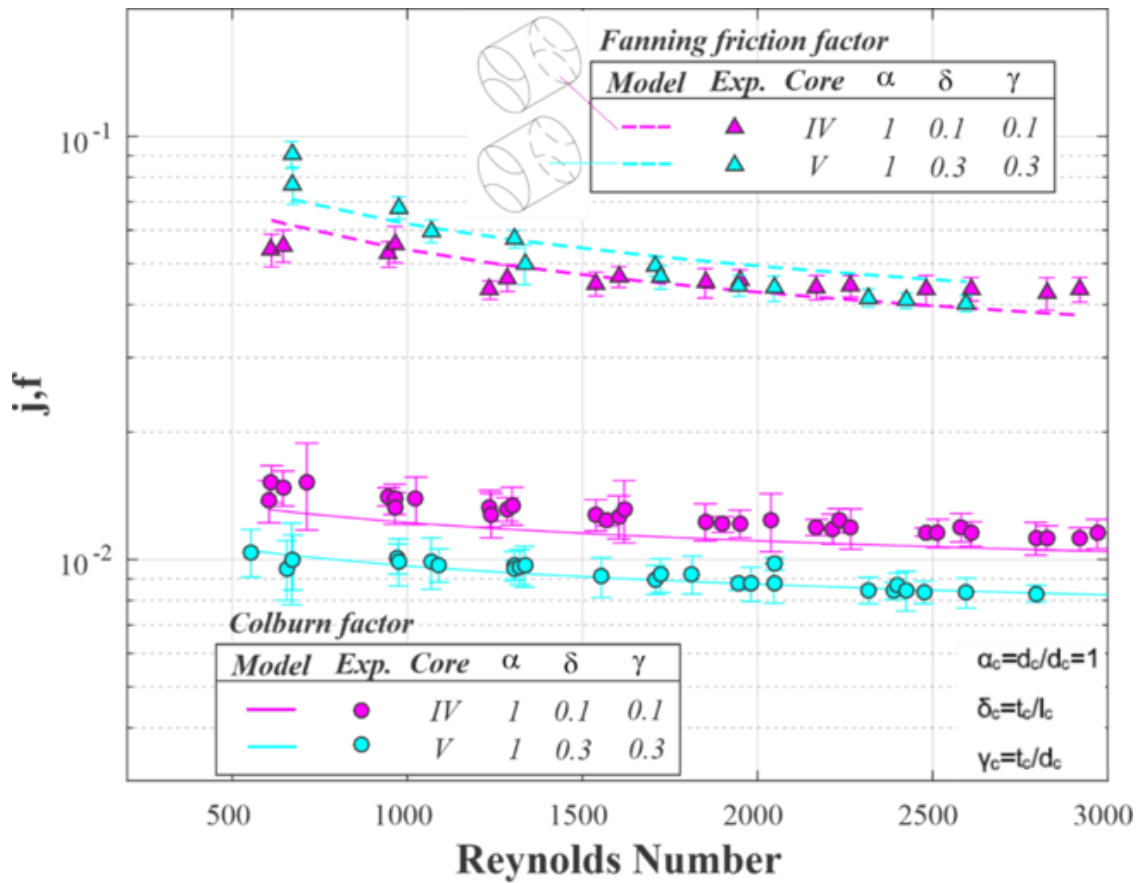
Figure 3.15 - Effect of the obstruction degree on the experimental j and f data.

3.4.4 Rectangular and circular offset strip fins performance comparison

In order to understand the performance of the cOSF geometry for the current heat exchanger application, the reference rOSF heat transfer geometry was used to compare the thermo-hydrodynamic efficiency in terms of flow area goodness factor (j/f) and volume goodness factor $(j/f^{1/3})$. These types of figures of merit are frequently employed in heat exchangers design to evidence the most suitable geometry for a specific application. The area goodness factor aims to select the heat transfer geometry which (for a given set of fluid properties Cp, μ, Pr, ρ, and a given hydraulic diameter Dh) will require the smallest heat exchanger frontal area. Similarly, the volume goodness factor yields to identify the geometry which will result in the smaller core volume [2]. The comparison was done using the devised correlations of the cOSF, Eqs. 24 and 26, with the rOSF correlations given by the Eqs. 22 and 23. First the area goodness factor of the five cOSF cores given in Table 3.1 and the respective rOSF are graphed in Fig. 3.16. In this figure is possible to visualize the similar behavior of the geometrical dimensionless parameters δ and γ in both geometries. In general, geometries with smaller δ and γ tend to have higher performance than the cores with bigger δ and γ cores. The biggest difference between the geometries is the drop of goodness factor for the rOSF after a maximum. The same behavior is not observed in the cOSF geometry, where in all cases the area goodness factor increased asymptotically with Reynolds. For the core I to V dimensions, the cOSF showed a superior area goodness factor performance after the Reynolds of 500.
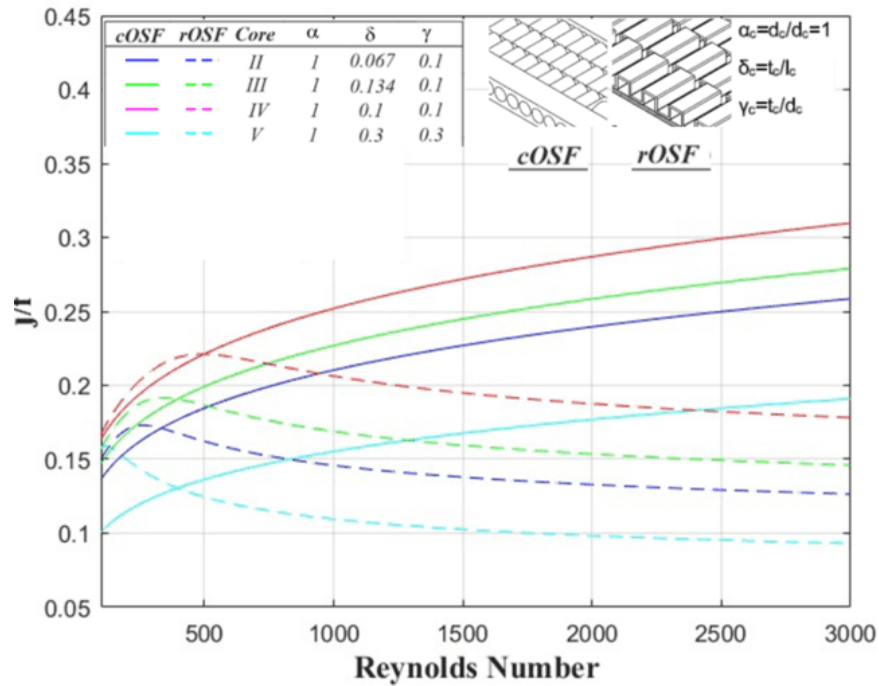
Figure 3.16 –Comparison of the Influence of the geometrical features of the offset strip fins (rectangular and circular) on their flow area goodness factor.

An additional performance evaluation criterion based on the volume goodness factor is presented in Fig. 3.17. At this analysis, the higher the volume goodness factors the smaller is the heat exchanger volume required for the same pump power. Again, both geometries showed a similar trend, where the cores I to IV had a similar performance and the core V presented an inferior tendency. By the volume goodness factor analysis, the rOSF geometry showed to require a smaller heat exchanger volume than the cOSF to exchange the same amount of heat for Reynolds number smaller than 1000. This effect can be related to the higher flow passages obstruction found in the cOSF by the semi-circular fin profiles. However, for Reynolds number higher than 1000 the cOSF tends to be superior.

$$FJ = j/f^{1/3}$$

cOSF	rOSF	Core	α	δ	γ
—	--	II	1	0.067	0.1
—	--	III	1	0.134	0.1
—	--	IV	1	0.1	0.1
—	--	V	1	0.3	0.3

$\alpha_c = d_c/d_c = 1$

$\delta_c = t_c/l_c$

$\gamma_c = t_c/d_c$

cOSF   rOSF

Reynolds Number
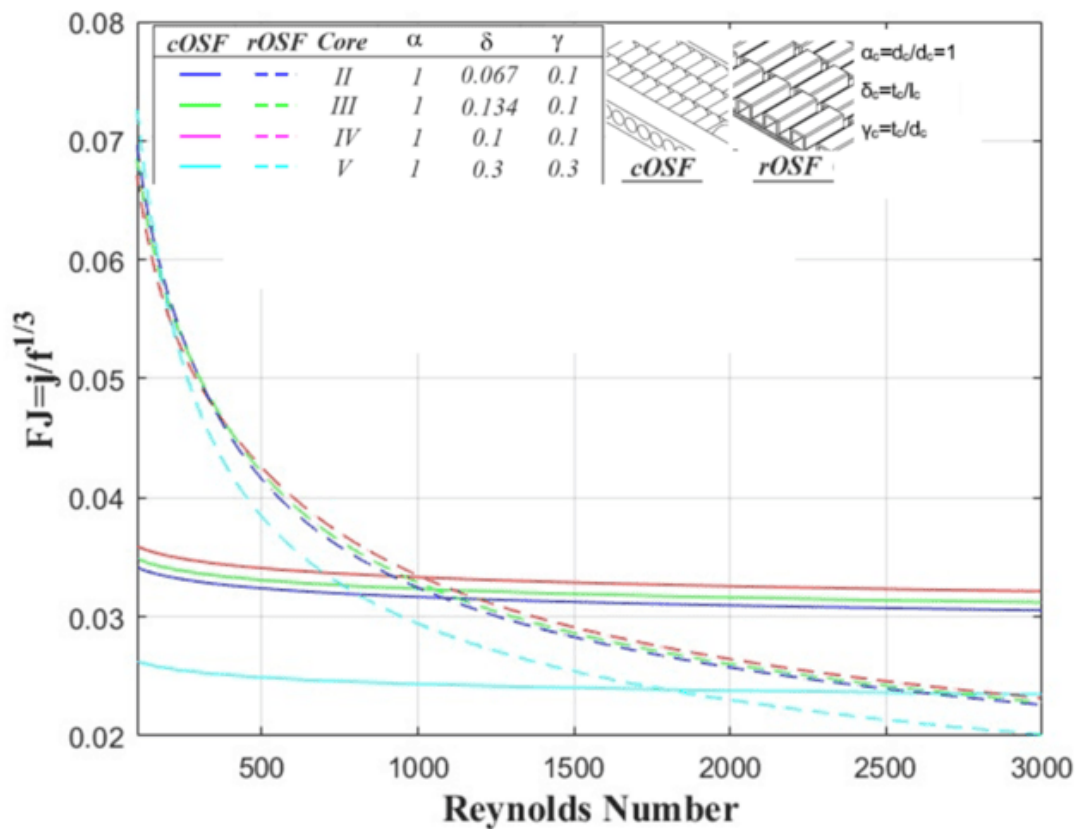
Figure 3.17 – Comparison of the Influence of the geometrical features of the offset strip fins (rectangular and circular) on their volume goodness factor.

3.5 Conclusions

A novel heat transfer geometry for compact heat exchangers, similar to the rectangular offset strip fins, is proposed. The circular offset strip fin has circular flow passages instead of the rectangular found in the rectangular offset strip fin configuration. The novel geometry was evaluated experimentally to assess its potential. The heat transfer and friction factor were investigated in 5 cOSF cores with variated flow passages dimensions. The Colburn factor j and Fanning friction factor f experimental data were obtained at two wall temperature levels in the Reynolds number range of 500<Re_{Dh}<3000. Single predictive correlations for j and f, in terms of dimensionless parameters δ and γ and Reynolds number were devised to describe the data asymptotic behavior, within an error of 6% and 8% for Colburn factor and Fanning friction factor respectively. The influence of each geometrical parameter on the performance of the geometry was investigated separately. Finally, the proposed novel circular offset strip fins are compared with the consolidated rectangular offset strip fins. The novel circular offset strip fins present some manufacturing and structural advantages in comparison with the literature offset strip fins, while similar thermal-hydraulic performance.

3.6 References

[1] Shah, R. K., Sekulić, D. P., "Classification of Heat Exchangers", Fundamentals of Heat Exchanger Design, 1st ed., Chap. 1, John Wiley & Sons, Ltd, New York, 2003, pp. 1-77. doi: https://doi.org/10.1002/9780470172605.ch1

[2] Kays, W. M., London, A. L., and Eckert, E. R. G. "Compact Heat Exchangers." ASME. J. Appl. Mech. June 1960; 27(2): 377. https://doi.org/10.1115/1.3644004

[3] Do, K. H., Choi, B.-I., Han, Y.-S., & Kim, T. (2016). Experimental investigation on the pressure drop and heat transfer characteristics of a recuperator with offset strip fins for a micro gas turbine. International Journal of Heat and Mass Transfer, 103, 457–467. doi:10.1016/j.ijheatmasstransfer.

[4] Li, J., Hu, H., & Zhang, Y. (2021). Experimental investigation and correlation development for two-phase pressure drop characteristics of flow boiling in offset strip fin channels. International Journal of Thermal Sciences, 160, 106693. doi:10.1016/j.ijthermalsci.2020.1

[5] Kim, M.-S., Lee, J., Yook, S.-J., & Lee, K.-S. (2011). Correlations and optimization of a heat exchanger with offset-strip fins. International Journal of Heat and Mass Transfer, 54(9-10), 2073–2079. doi:10.1016/j.ijheatmasstransfer.

[6] Zheng, X., & Qi, Z. (2018). A comprehensive review of offset strip fin and its applications. Applied Thermal Engineering, 139, 61–75. doi:10.1016/j.applthermaleng.2018

[7] Jiang, Q., Pan, C., Chen, Y., Zhang, Q., Tang, Y., Gu, J., & Aleksandr, P. (2021). Improved heat transfer and friction correlations of aluminum offset-strip fin heat exchangers for helium cryogenic applications. Applied Thermal Engineering, 192, 116892. doi:10.1016/j.applthermaleng.2021

[8] London, A. L. (1968). Offset Rectangular Plate-Fin Surfaces—Heat Transfer and Flow Friction Characteristics. Journal of Engineering for Gas Turbines and Power, 90(3), 218. doi:10.1115/1.3609175

[9] Joshi, H. M., & Webb, R. L. (1987). Heat transfer and friction in the offset strip fin heat exchanger. International Journal of Heat and Mass Transfer, 30(1), 69–84. doi:10.1016/0017-9310(87)90061-5

[10] Manglik, R. M., & Bergles, A. E. (1995). Heat transfer and pressure drop correlations for the rectangular offset strip fin compact heat exchanger. Experimental Thermal and Fluid Science, 10(2), 171–180. doi:10.1016/0894-1777(94)00096-q

[11] Zhu, Y., & Li, Y. (2008). Three-Dimensional Numerical Simulation on the Laminar Flow and Heat Transfer in Four Basic Fins of Plate-Fin Heat Exchangers. Journal of Heat Transfer, 130(11), 111801. doi:10.1115/1.2970072

[12] Sujoy K. Saha, Hrishiraj Ranjan, Madhu S. Emani, Anand K. Bharti, "Offset-Strip Fins", Heat Transfer Enhancement in Plate and Fin Extended Surfaces, 1st ed., Chap. 1, Springer, Switzerland, 2020, pp. 33-57. https://doi.org/10.1007/978-3-030-20736-6

[13] Peng, H., Ling, X., & Li, J. (2014). Performance investigation of an innovative offset strip fin arrays in compact heat exchangers. Energy Conversion and Management, 80, 287–297. doi:10.1016/j.enconman.2014.01.05

[14] Hao, J.-H., Chen, Q., Ren, J.-X., Zhang, M.-Q., & Ai, J. (2019). An experimental study on the offset-strip fin geometry optimization of a plate-fin heat exchanger based on the

heat current model. Applied Thermal Engineering, 154, 111–119. doi:10.1016/j.applthermaleng.2019

[15] Ordóñez, J. C., & Bejan, A. (2000). Entropy generation minimization in parallel-plates counterflow heat exchangers. International Journal of Energy Research, 24(10), 843–864. doi:10.1002/1099-114x(200008)24:10<843::aid-er620>3.0.co;2-m

[16] Shah, R. K., Sekulić, D. P., "Surface Basic Heat Transfer and Flow Friction Characteristics", Fundamentals of Heat Exchanger Design, 1st ed., Chap. 7, John Wiley & Sons, Ltd, New York, 2003, pp. 425-562. https://doi.org/10.1002/9780470172605.ch7

[17] Ramesh K. Shah, Dušan P. Sekulić., "Heat Exchanger Pressure Drop Analysis", Fundamentals of Heat Exchanger Design, 1st ed., Chap. 6, John Wiley & Sons, Ltd, New York, 2003, pp. 425-562. https://doi.org/10.1002/9780470172605.ch6

[18] Marcia B. H. Mantelli, "Fabrication and Testing", Thermosyphons and Heat Pipes: Theory and Applications, 1st ed., Chap. 5, Springer, Switzerland, 2021, pp. 135-153. https://doi.org/10.1007/978-3-030-62773-7

[19] J.P. Holman, Experimental methods for engineers, McGraw-Hill Education, Boston, MA, United States, 2011.

4. Numerical analysis of a novel wrap-around axisymmetric diffusion bonded recuperator for gas turbines with circular offset strip fins core geometry

Nomenclature

A	=	area, [m^2]
A_{ff}	=	free-flow area, [m^2]
C	=	flow stream capacity rate, [W/K]
c_p	=	specific heat of fluid at constant pressure, [J/kg]
d	=	diamter, [m]
D_h	=	hidraulic diameter, [m]
f	=	Fanning friction factor, [-]
G	=	mass velocity based on the minimum free area, [kg/m²]
h	=	Head loss, [m]
j	=	Chilton-Colburn factor, [-]
k_w	=	material thermal conductivity, [W/mK]
l	=	recuperator axial length, [m]
l_{core}	=	core length, [m]
l_{man}	=	manifold length, [m]
$\dot{m}$	=	mass flow rate, [kg/s]
n_{cells}	=	number of cells, [-]
n_{mod}	=	number of modules, [-]
Ntu	=	number of transfer units, [-]
p	=	pressure, [Pa]
Pr	=	Prandtl number, [-]
r	=	radius, [m]
R	=	thermal resistance, [K/W]
R	=	Ideal gas constant, [J/kgK]
Re	=	Reynolds number, [-]
s	=	obstruction degree or gap distance, [m]
s_p	=	space distance, [m]
T	=	temperature, [°C]
th	=	plate thickness, [m]
U	=	overall heat transfer coeficient, [W/m²]
V	=	volumetric flow rate, [m^3/s]
w	=	wall thickness, [m]
z	=	distance from the origin, [m]
α	=	module angle, [degrees]
ε	=	effectiveness, [-]
η	=	fin efficiency, [-]
v	=	specific volume, [m^3/kg]
ρ	=	fluid density, [kg/m^3]

Subscripts

a	=	air
g	=	gas
i	=	at the inlet
in	=	inlet
inn	=	inner
m	=	mean

mod	=	module
o	=	at the outlet
out	=	outer or outlet
x	=	refer to the plate X
y	=	Refer to the plate Y

4.1 Introduction

In the early 2000s, the energy production perspectives were pointing out the microturbine as a potential technology to take over the distributed power generation field in the range of 25 to 200 kW, due many advantages, among them; low emissions, multi fuel capability, low noise, compact size, high reliability and low maintenance [1] - [2]. However, for the turbogenerator's distributed power generation market competitiveness, with respect to the conventional gas turbines and reciprocating engines, a thermal efficiency of 30% or higher is essential. A conventional microturbine achieves at most 20 per cent efficiency without a recuperator. The use of a recuperator in the cycle Brayton improves its efficiency to 30 percent and 40 percent, depending on the recuperator's effectiveness [3]. After two decades of microturbines design development, the combustion, mechanical and generator efficiencies are close to the maximum. The same was attained with the compressor and the turbine aerodynamic efficiencies that are near plateauing with the CFD and optimization tools. Only three ways still have potential for efficiency advancement in the low-pressure ratio single-shaft radial flow microturbines which are: increasing values of turbine inlet temperature and pressure and recuperator effectiveness [4].

Arguably, the recuperator is the Achilles tendon of the microturbines due to three main reasons: the high cost, the pressure weakness, and the material temperature limit. High effectiveness recuperator requires a great surface area per volume, which implies in very small hydraulic diameters and consequently the need of very thin plates in its design. For the manufacturing point of view, faithfully reproducing the optimal design of the complex matrix of the exchanger core is a tough task that has a high cost and hampers the mass production of the component. It is estimated that about 25 - 30 percent of the overall machine cost is dedicated to the recuperator [5]. Regarding the pressure, the thin plates and the welding method used in the most recuperators result in a set that is not pressure resistant. For instance, the plate type, cross corrugated heat transfer geometry used in many exchangers, is formed by fin fold plates stacked and welded only in the side edges (periphery) [3], this configuration does not support high internal pressures, acting as a "balloon", due to the lack of structural junctions inside the exchanger core. And lastly, the operation temperature limit of the materials frequently used in recuperators, as the austenitic steel (300 series stainless steel), is about 675°C. The material limitation prevents the increase of cycle temperatures, and consequently inhibits the increase in cycle efficiency. Higher temperatures require the use of superalloys (Inconel, Haynes and PM2000) which would over increase the cost of the component [4].

Efforts are being made to develop high-performance recuperators at low cost. High-performance means; High effectiveness $\left(\varepsilon \geq 90\%\right)$, low total pressure drop $\left(\Delta p/p < 5\%\right)$, high operating pressure ratio and temperatures (4 bar or higher and up to 675°C), long life operation without any maintenance (about 40,000 hours) and compactness with light weight and integral manifolds [5]. Different exchanger types and heat transfer surfaces are proposed

to satisfy all the exigencies, each one with its own specific qualities and drawbacks. About the exchanger arrangement, there are two main types of recuperators: the annular wrap-around recuperator, mounted asymmetrically around the rotor, and the rear-mounted cube type recuperator, positioned behind the rotating machinery. The first, also called annular or axisymmetric recuperator is more resilient to the thermal cycle and has less total pressure drop as compared to the box type recuperator [2]. However, the cube type recuperator is simpler to manufacture, assembled in the turbine, and allow easier maintenance. Regarding to the heat transfer surface, there are three main types, the plate-type primary surface recuperator (currently the most used surface in the MGT recuperators), the extended surface recuperators and the tubular primary surface recuperator. The last, although withstands higher pressures, has lower surface area, lower heat transfer coefficient and higher pressure drop when compared with the other two surfaces discouraged its utilization.

The current emphasis is on the development of recuperators of plate-type primary surface. A variety of companies manufacture different recuperators using the commercially available plate-type primary surfaces; among them there are the cross-corrugated (CC), the cross-undulated (CU) and the cross-wavy (CW) surfaces. A complete overview of these surfaces is present in the literature [6][7]. Another high-performance heat exchanger surface used in gas-gas exchangers is the rectangular offset strip fin geometry. The large area density linked to the turbulent effect caused by flow interruptions in the sectioned fins provides high heat transfer coefficients with moderate pressure drop for gaseous flows. Some recent studies evaluate the application of the rectangular offset strip fin geometry in the recuperator of micro gas turbines [8][9]. However, despite the high heat transfer rate and low pressure drop, the OSF plate-fin geometry requires a brazing procedure to join the fins in the fluid separation wall in order to reduce the contact thermal resistance between them. The brazing procedure makes the OSF not viable due the high costs, high-temperature weakness and difficult automated manufacturing [5].

The Capstone annular wrap-around plate fin recuperator is one of the successful recuperator projects in current utilization [10]. With millions of produced samples, operation hours and start-load-stops (thermal stress) cycles the project is very consolidate in the market. Several qualities are attributed to its configuration such as high effectiveness, low pressure drop, high reliability and durability. In the other hand, the annular and fully welded fin fold plates recuperator also has some drawbacks. The exchanger is not simple to manufacture. High precision is required in the recuperator assembly, to reproduce the designed channels of the CC surface core and the manifolds have a complex design to ensure good flow distribution through the core on both fluid sides. The fully welded structure is rigid and makes maintenance difficult when necessary. In addition, the concept can't provide further improvements for the cycle because it can't withstand greater pressures and is not possible to use the bi-metallic plates approach to increase the component temperature operability without over increase the cost.

The present research proposes a new recuperator design concept with annular wrap-around configuration. The recuperator is divided into modules, where each one works as an independent counter flow gas-gas printed circuit heat exchanger. The modules are formed by a sequence of machined plates joined by diffusion bonding, containing two manifolds and one core each. The manifolds are positioned at the extremities and their function is to drive the air and the exhaust gases towards their respective paths through the core, while keeping them separated. The core, placed between the manifolds, houses the circular offset strip fin (cOSF) heat transfer geometry [Chapter 2], where the heat is exchanged between the fluids. The air

flow enters and exits the recuperator in a radial direction and the gas flows in the axial direction of the turbine axis. The flows assume the counter current configuration inside the core region. It is the first time that a diffusion bonding exchanger is suggested for a gas-gas recuperator application. The diffusion bonding is an advanced heat exchanger manufacturing process which allies robustness with compactness [11] showing to be advantageous for the present star-of-art.

Beyond to provide the same performance characteristics of the current recuperators (low pressure drop, high effectiveness and volume compactness), some qualities intrinsic of the new recuperator concept for micro gas turbines are listed:

- No clogging (the cOSF heat transfer geometry of the recuperator core has all the communication flow passages, which prevent clogging of the channels).
- Increased pressure ratio and component reliability (the diffusion bonded modular concept divide the thermal stresses of the component, also proposing a structural integrity characteristic allowing to withstand of higher-pressure ratios, which provides reliability and long-life to the component).
- Flow maldistribution problem is solved (the cOSF core communication passages exempt the need of manifold intern structures to distribute the flow over the recuperator core, once the flow distributes itself as it passes through the core.
- Promising reduced manufacturing costs. (the use of stamped plates or automated CNC manufacturing processes allied to the diffusion bonding method allow a continuous and automated manufacturing process).
- Optimum design manufacturing (the manufacturing method of present geometry allows to precisely reproduce the optimum design of the flow passages, reducing losses due the non-design conformity).
- Increased working temperature capability (the manufacturing method, staggering plates in the axial direction allow the utilization of bi-metallic approach, where superalloys can be used only on the hot end of the recuperator core and stainless steel or other less expensive metals in the low temperature zone of the recuperator, which allows to increase the working temperature of the component without over
- increasing the cost).
- Easy maintenance (the modular configuration provides easy maintenance and allows module replacement when necessary).
- Easy, flexible, no bolt assembly. The diffusion-bonded recuperator modules are assembled by a metallic stripe tape around the recuperator outer diameter, which provides simple joining and allows the material thermal expansion.

In the present chapter, a completely novel recuperator concept is proposed, including the manufacturing process, component assembly and heat transfer surface used in the core. A mathematical model is suggested to access the thermal and hydrodynamic performance of the component. In addition, a design code with the mathematical model and an entropy generation minimization procedure is proposed to design the "optimum" flow passages dimensions and define the recuperator size for any turbine size with the minimum irreversibility generation. The design code was validated with a numerical study using Ansys Fluent software. The numerical analysis was also compared to experimental data to check the reliability of the results. Finally, four turbine study cases were investigated with the present concept and its effectiveness and recuperator core sizes are presented.

4.2 Concept description

In this section the diffusion bonded recuperator concept is described. First the modular component is introduced with its assembly and sealing in the gas turbine. In sequence, the modules manufacturing is detailed, with its steps and how the fluid passages are formed. The main dimensions and the recuperator details are also described in this section.

4.2.1 Modular axisymmetric recuperator concept

The wrap-around axisymmetric form has been present in architecture since the medieval period on the rose windows found in many cathedrals around the world, see the left-hand-side of Fig. 4.1. Another example is the arc or vault (arco di Mattoni), as is called the semicircular form frequently found in portals, used to distribute, and withstand the weight of the building over portal structural pillars (right-hand-side of Fig. 4.1). Both civil structures use the trapezoidal stones shape assemble to form an arc to distribute the weight of the construction with structural robustness in a simple method [12].

Figure 4.1 – "Rosone di chiesa" (left) and "arco di mattoni" (right).

The same concept was incorporated in the present recuperator configuration. The annular wrap-around recuperator type was divided into a defined number of identical and independent modules which are assembled as the trapezoidal bricks of the portal. Fig. 4.2 shows an example of the modular axisymmetric recuperator configuration concept. The representative model is composed by several identical modules, n_{mod}, defined by the angle α, where $n_{\mathrm{mod}} = 360/\alpha$. Each module contains two manifolds, responsible for the distribution of the flows at the entrance and exit, and one core, designed to promote the heat transfer between the flows. The air flow enters and exits the recuperator in a radial direction while the gas flows always in the axial direction of the turbine shaft. The recuperator volume is defined by the main dimensions; inner and outer diameters d_{inn}, d_{out}, and the length l, which is the recuperator length in the axial direction. All dimensions can be tailored depending on the turbine size.
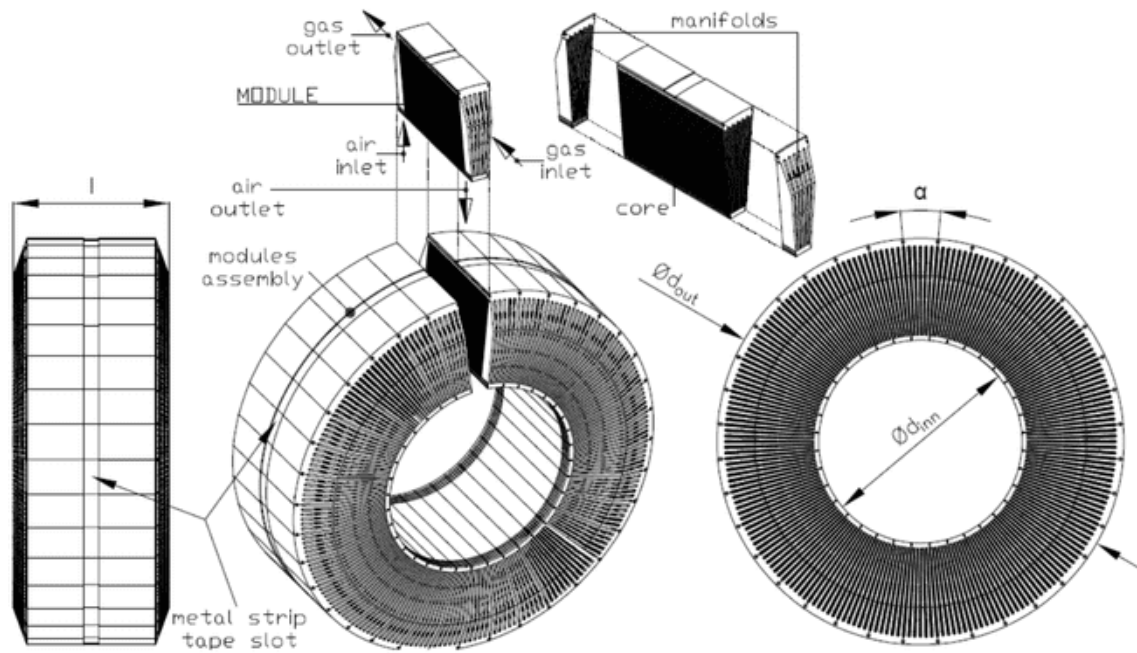
Figure 4.2 - Diffusion bonded modular wrap-around axisymmetric recuperator concept.

Fig. 4.3 shows an illustration of the modular assembly and sealing. The assembly and junction of the modules are made using a tensioned metal strap, that fits into a recessed channel on the outer periphery of the annulus. The tension on the strap can be adjusted to assure the recuperator sealing while providing thermal expansion flexibility. To avoid the gas leakage from the recuperator, both side faces of the modules, at the top and the bottom, contain longitudinal gasket slots where high-temperature strip gaskets are inserted to promote the heat exchanger sealing, as shown in the assembly sealing details at the left-hand-side of the figure. The module junctions are always in the gas side of the heat exchanger, which is subjected to pressures close to the atmosphere favoring the sealing.
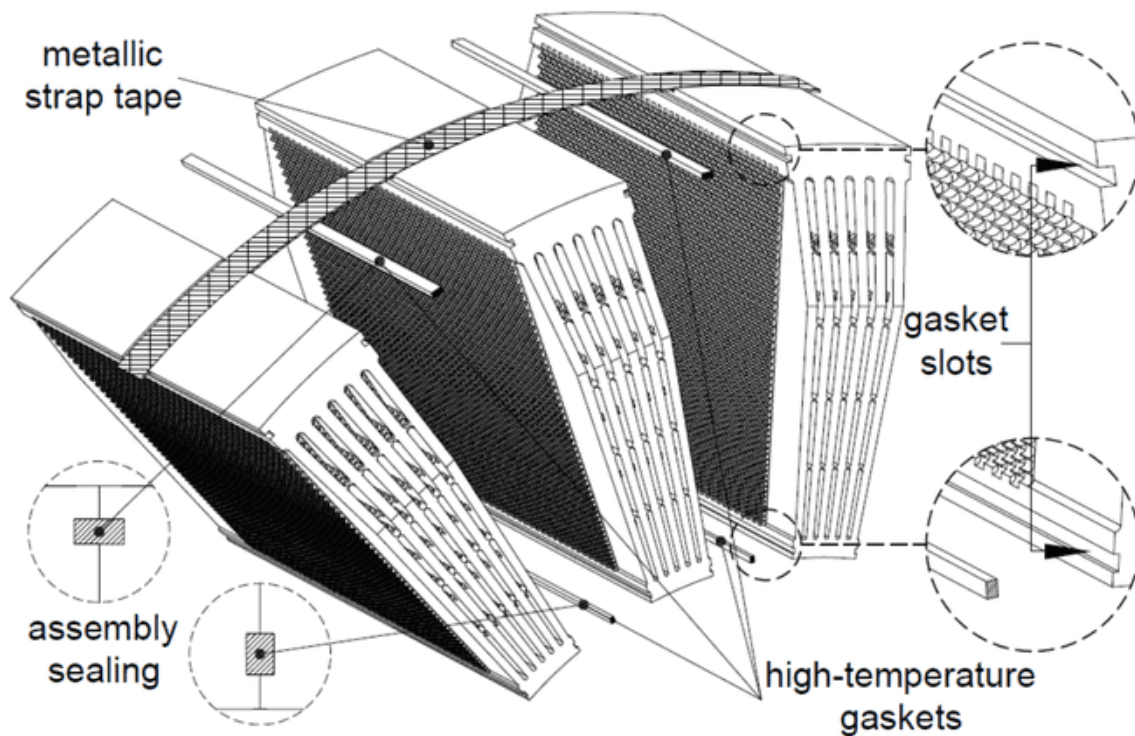
Figure 4.3 - Modules assembly sealing and fixation.

4.2.2 Module description

The modules used in the recuperator assembly are formed by a sequence of staggered machined plates joined by diffusion bonding. As mentioned before, each module has two manifolds and one core. The manifolds are placed at the front and back faces of the module, to drive the air and the exhaust gases flow to their respective paths through the core, while keeping them separated. The core, situated between the manifolds, houses the cOSF heat transfer geometry used to enhance the heat transfer between the incoming air and exhaust gases. Fig. 4.4 shows the manifold and core plate shapes, its sequences, and the module manufacturing step. The module is symmetric in the XY and YZ planes. The number of plates can vary depending on the plate thickness to provide the desired manifold and core lengths. The manifolds plates have machined channels to form the passages with low obstruction degree. Some structural reinforcements are necessary to provide rigidity to the manifold plates (see det.1 on the right-hand-side of the same figure). These reinforcements can be placed in different positions in the manifold plates to not obstruct the flow. Note that all the manifold plates except for plate 0 have open passages in the bottom to allow the air to enter and exit the recuperator (see det.1). These open passages are placed only in the air side to lead the radial airflow to the air side of the core. Analogously, plate 0 is opened only in the gas passage, to direct the gas only to the gas side in the core. The core is formed by two types of perforated plates with displaced holes, plate X and Y. The stacking of the interleaved core plates results in the circular offset strip fin geometry, which is an enhanced heat transfer surface with high heat exchange rates combined with a low pressure drop [Chapter 3]. For the plates manufacturing, any automated machining techniques can be used, from stamping to laser or water jet cutting machines, which are able to produce precise flow passages with hydraulic diameter of the order of 5×10^{-4}m. After diffusion bonding, the solid body has the edges of the manifolds trimmed to reduce mass and the lateral module faces can be flattened by a milling cutter to perfect match with the neighbor modules

(see the milling face in Fig. 4.4). After that the module is ready to be installed in the turbine. Is important to mention that the present module manufacturing method allows the use of different material plates throughout the module length. With that, high-cost superalloys can be used only on the hot end of the recuperator core, the region subject to the extreme temperatures, and then, lower grade materials are applied from the medium temperature toward the cold end of the heat exchanger, forming a bi-metallic recuperator [4][5]. Furthermore, the bonding between the common stainless steel and the super alloys is not a problem for the diffusion bonding process since the materials thermal characteristics and properties are very similar [13]. This proposal can increase considerably the component working temperature keeping moderate the recuperator material cost.
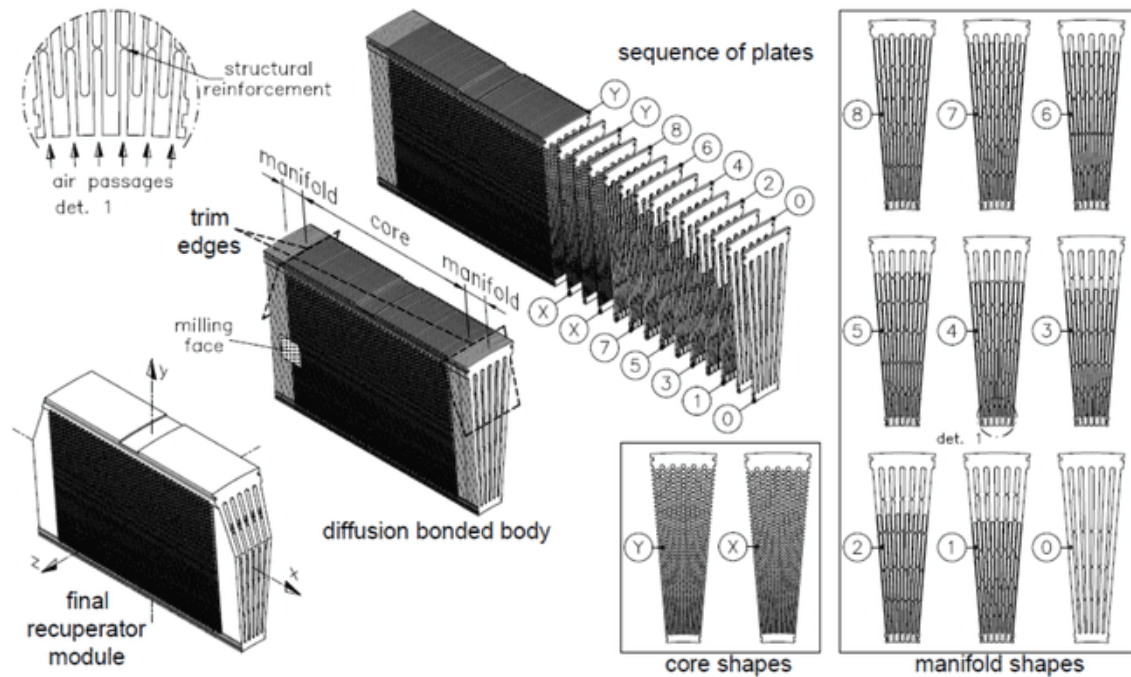
Figure 4.4 – Module manufacturing, plate shapes, stack sequence, and manufacturing steps.

Each recuperator module can be considered as an independent gas-to-gas printed circuit heat exchanger with air (cold) and combustion exhaust gases (hot) cells. The number of air and gas cells in the module depends on their respective flow passages dimensions. The modules always contain the same number of hot and cold cells, which are interspersed. The cells placed at the center of the module and on its side, faces are always gas cells, being the side faces half-cell gas. The half-cells make up a full gas cell with the neighbor module when they are assembled in the final orientation. In Fig. 4.5 illustrates the direction of the gas and air flows when enter and leave the recuperator, the main dimensions and the section views detailing the module configuration. As mentioned before, the air enters and exits the recuperator in the radial direction while the gas flows always in the axial direction. The axial view AX shows the "gas flow view" just before it reaches the recuperator. Note that the gas passages are open, and the air passages are closed in the manifold plate 0 (ref. Fig. 4.4). The section view BB illustrates the arrangement of cells inside the modules. The air and gas cells are interspersed establishing the counterflow configuration in the recuperator core. The air and gas cells are separated by a wall, with thickness w, through all the core length, including the manifolds and core. In the lower zoom of section BB is shown the gasket slot used for the gas-side recuperator sealing and the manifold airflow passages. These passages allow the airflow to enter and leave the recuperator. The cut views, section CC and DD, shows the air and the gas sides with their main dimensions

and flow conditions (temperature, pressure, and mass flow rate), respectively. The manifold length l$_{man}$ and the core length l$_{core}$ are defined by the number of plates and the plate thickness th used. The air passage lengths la,in and la,out are designed to provide the lowest pressure drop. The present work doesn't consider the manifolds pressure drops, which is expected to be low since it doesn't contain any kind of fill except some reinforcements. The design present here is focused only on the core design.
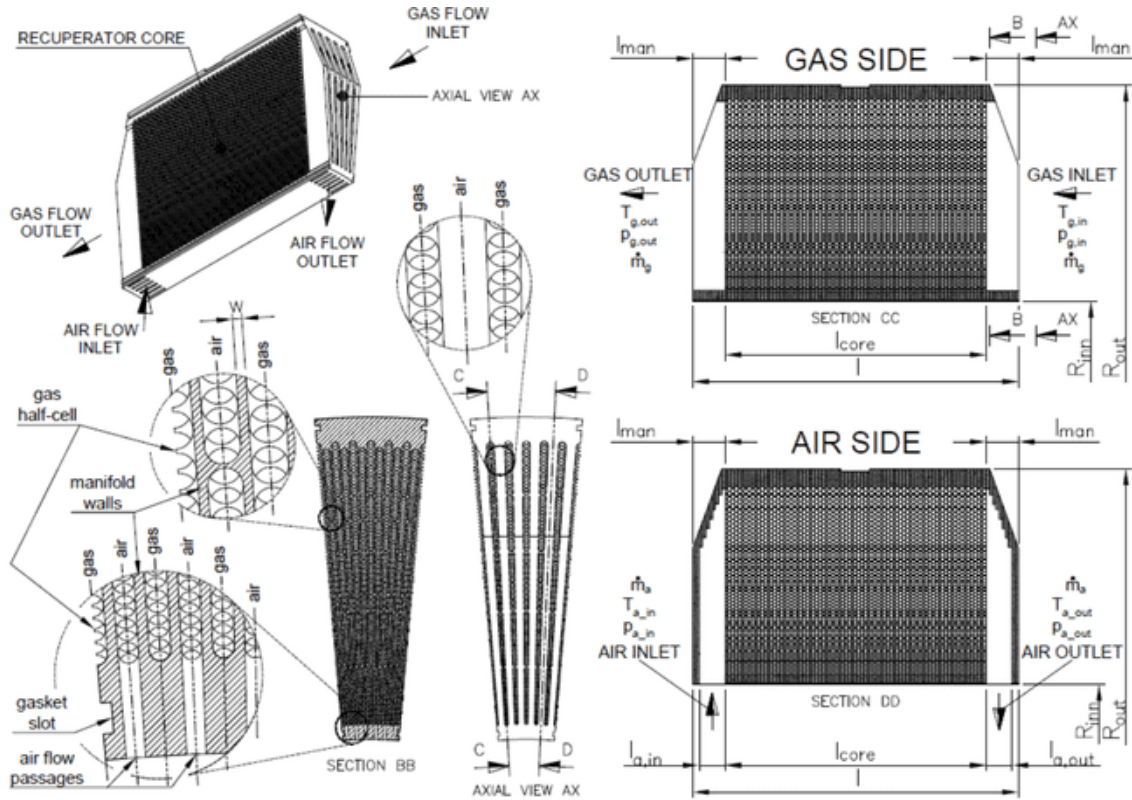
Figure 4.5 – Recuperator module description, flow direction (air and gas), main dimensions and flow conditions.

The recuperator core, design object of the present study is composed by a stack of interspaced machined plates X and Y. The plates stack always start and end with a plate type X. Fig. 4.6 illustrates the core solid and fluid volumes to facilitate the flow passages visualization. The perforated plates (X and Y) with displaced holes form the circular offset strip fins (cOSF) heat transfer geometry in the recuperator core [Chapter 3]. One of the main advantages of the cOSF is that all the flow passages of one side are communicating. This characteristic reduces the chance of clogging and eliminates the need of manifold fill to distribute the flows over the core passages. The communicating passages allow the flow to self-distribute over the core height. Both, air and gas cells have the same cOSF heat transfer geometry, composed by the repetition of the unitary cell with its dimension; diameter d, length th and obstruction degree s. The flow passages of both sides have different diameters through the core height, and consequently different unitary cells proportions, being the lower passages with smaller hydraulic diameter than the passages at the top heigh of the core. The different proportions lead to different pressure drop characteristics and consequently different mass flow rates passing through the channels at different levels. This analysis is further discussed in Section 4.3.3 and 4.5.3 (Hardy Cross method). Only one unitary cell length (plate thickness th) was considered at the present study. Furthermore, the cOSF configures high efficiency fins with circular profiles. These fins

also provide an important structural robustness connection between the air-gas separating walls, with no thermal stress concentration once the fins have filleted bases (circular profile).

Figure 4.6 – Diffusion bonded recuperator core, flow configuration and cOSF characteristic dimensions.

With the modular axisymmetric diffusion bonded recuperator defined a mathematical model is proposed in the next section to describe the geometrical parameters and the thermal and hydraulic performance of the component.

4.3 Mathematical modeling

In this section, the module dimensions are defined, including its trigonometrical relations and its free flow and heat transfer areas. The thermo-hydraulic models are used to describe the fluid distribution through the channels, the pressure drop, and heat transfer are also described.

4.3.1 Recuperator geometrical and dimensional characteristics

The recuperator core described in Section 4.4.1 has its geometrical characteristics detailed in sequence. Fig. 4.7 presents the geometrical scheme with the trigonometrical relations found in the modular recuperator core concept. The scheme shows the module geometrical dimensions, where the dimensions are overstated to facilitate the core geometry comprehension. As mentioned before, the module core is composed of interspaced air and gas cells in the angular direction of the cylindrical coordinate system centered at the origin. Note that the central and the lateral cells (half-cells placed in both core laterals) are gas cells. The

lateral half cells complete a full gas cell with the neighbor modules when the recuperator is assembled in the final configuration.
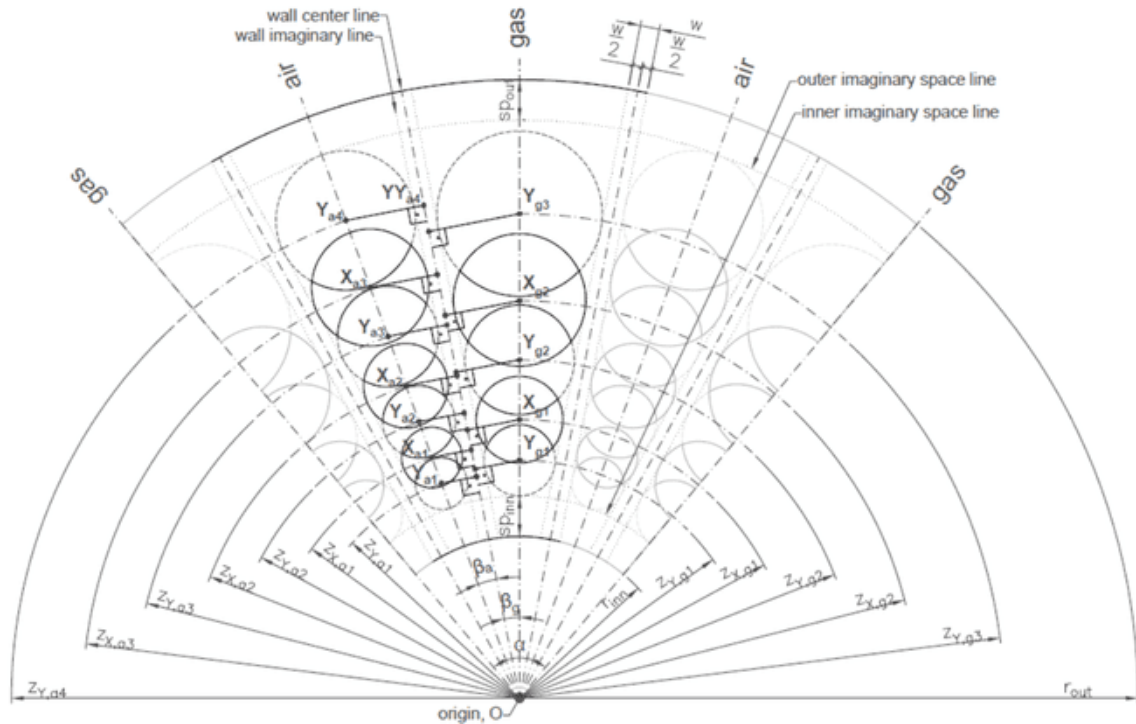
Figure 4.7 – Module core dimensional variables scheme.

The core geometry, referenced at the origin, is delimited by the inner and outer radius, r_{inn} and r_{out}, and by the angle α, that must be multiple of 360, used to define the number of modules in the recuperator, n_{mod}. The core always contains the same number of air and gas cells, $n_{cell,a} = n_{cell,g}$, being the total number of cells in a module the sum of both; $n_{cell,mod} = n_{cell,a} + n_{cell,g}$. The cells are separated by a wall with thickness w, represented by imaginary dotted lines in the scheme of Fig. 4.7. The walls are of constant thickness, and their centers coincide with a line passing through the origin. The wall thickness is a manufacturing dependent parameter, which is limited to the minimum thickness acceptable by the diffusion bonding process. The number of walls is equal to the number of cells in the module. In addition, two imaginary margin spaces (sp_{inn} and sp_{out}) offset by the inner and outer radius, respectively, are set to provide space to the gasket slots and give robustness to the component.

Some dimensional design inputs should be given to define the core geometrical characteristics; recuperator inner and outer radius r_{inn} r_{out}, module angle α, the number of cells in a module $n_{cell,mod}$, inner space sp_{inn}, outer space sp_{out}, wall thickness w, the plates thickness th (unitary cell length), the obstruction degree factor k (which is described later) and the air side first hole radius at the plate Y $r_{Y,a1}$. All the other dimensions, such as air and gas cells holes diameters and the number of holes that "fits" in each cell height are defined by trigonometric relations at the right triangles found in the scheme of Fig. 4.7. The trigonometrical output dimensions are; gas side first hole radius at the plate Y $r_{Y,g1}$, the number of holes of each cell $n_{hole,a}$ and $n_{hole,g}$, and their radius $r_{X,a(n)}$, $r_{Y,a(n)}$ and $r_{X,g(n)}$, $r_{Y,g(n)}$, where the

subscript "n" is an counting number. The mathematical procedure to obtain the output variables is now described.

The air and gas cells have the cOSF configuration formed by a sequence of offset holes in the plates X and Y, with all hole's centers coinciding with a center line passing through the origin. The hole dimensions and its positions are defined first at plate Y, and then, its locations are used as reference for the holes of plate X. All dimensions of plate X are dependent on the holes of plate Y. The core geometry is defined in the angular and radial directions and has its length in the axial direction. The angular dimensions must also be defined first, by the module angle α, the recuperator inner radius r_{inn}, inner space sp_{inn}, wall thickness w, air side first hole radius on the plate Y $r_{Y,a1}$ and the gas side first hole radius on the plate Y $r_{Y,g1}$, for which the last is the only unknown variable. By nomenclature definition, the first hole counting of each cell is defined as the one closest to the origin, and the counting number increases from the inner to the outer radius sense. All first holes of the plate Y, $r_{Y,a1}$ and $r_{Y,g1}$, are tangent to the inner space imaginary line and walls imaginary lines. Starting from the air side, the distance of the first hole center from the origin $z_{Y,a1}$, shown in the Fig. 4.7 is defined by

$$z_{Y,a1} = r_{inn} + sp_{inn} + r_{Y,a1} \tag{1}$$

At the triangle Y$_{a1}$OYY$_{a1}$, the air side angle β_a is obtained by

$$tg\,\beta_a = \frac{r_{Y,a1} + w/2}{z_{Y,a1}} \tag{2}$$

Then, the gas side angle β_g and consequent the $r_{Y,g1}$ are found with the triangle Y$_{g1}$OYY$_{g1}$ using the relations

$$\beta_g = \frac{\alpha - n_{cell,a} 2\beta_a}{2 n_{cell,g}} \tag{3}$$

$$r_{Y,g1} = tg\,\beta_g z_{Y,g1} - w/2$$

Similar to Eq. 1, the distance of the center of $r_{Y,g1}$ from the origin is determined by

$$z_{Y,g1} = r_{inn} + sp_{inn} + r_{Y,g1} \tag{4}$$

With the angular dimensions defined (cells width) now the trigonometric relations are used again to define the number of holes of each cell in the radial direction. Still in the plate Y, in sequence at the radial direction, the second holes of the air and gas cells $r_{Y,a2}$ and $r_{Y,g2}$ are tangent to the imaginary walls lines and its centers are at a distance of $z_{Y,a2}$ and $z_{Y,g2}$ from the origin, respectively. These distances are given by

$$z_{Y,a2} = z_{Y,a1} + r_{Y,a1} + s_{a1} + r_{Y,a2}$$
$$z_{Y,g2} = z_{Y,g1} + r_{Y,g1} + s_{g1} + r_{Y,g2} \tag{5}$$

The terms s_{a1} and s_{g1} are the tangential distances between the first and second holes of the air and gas respectively. These distances are defined by

$$s_{a1} = \left(r_{Y,a1} + r_{Y,a2} \right) k$$

$$s_{g1} = \left(r_{Y,g1} + r_{Y,g2} \right) k \tag{6}$$

Where the factor k is the channel obstruction degree factor which can be set in the range of $0 < k < 1$. When k is zero, the Y plate holes of the same cell are tangent and consequently, the flow passages have the minimum obstruction degree. The opposite total channels obstruction is obtained when k is unitary. It is desired to keep the factor k with the lowest possible values to favors the thermal-hydraulic performance of the cOSF [Chapter 3]. This proximity between holes is constrained by the precision of the manufacturing method used to machine the plates. The unknown second hole radius $r_{Y,a2}$ and $r_{Y,g2}$ are then obtained by the cathetus relation of the right triangles with vertices $Y_{a1}OYY_{a1}$ and $Y_{a2}OYY_{a2}$ for the air side and $Y_{g1}OYY_{g1}$ and $Y_{g2}OYY_{g2}$ for the gas side

$$\frac{r_{Y,a2} + w/2}{r_{Y,a1} + w/2} = \frac{z_{Y,a2}}{z_{Y,a1}}$$

$$\frac{r_{Y,g2} + w/2}{r_{Y,g1} + w/2} = \frac{z_{Y,g2}}{z_{Y,g1}} \tag{7}$$

Note that the vertices YY coincide with the wall center line and are not shown in the schematic figure.

The Eqs. 5, 6 and 7 can be rewritten in a generic form to encompass all air and gas holes, by

$$z_{Y,(n)} = z_{Y,(n-1)} + r_{Y,(n-1)} + s_{(n-1)} + r_{Y,(n)}$$

$$s_{(n)} = \left(r_{Y,(n)} + r_{(n+1)} \right) k \tag{8}$$

$$\frac{r_{Y,(n)} + w/2}{r_{Y,(n-1)} + w/2} = \frac{z_{Y,(n)}}{z_{Y,(n-1)}}$$

The number of holes in the air and gas cells in the radial direction is delimited by the recuperator inner and outer radius r_{inn} r_{out}, and the offset spaces sp_{inn} sp_{out}. The next holes radius is found with the same procedure used to find the second hole radius. The procedure is repeated until no more holes can be added in the radial direction due to the space limitations restricted by the inner and outer radius and spaces.

Finally, with the holes dimensions of plate Y defined and used as reference, the holes of plate X are set. All holes of plate X are also tangent to the imaginary wall dotted lines of Fig. 4.7, and their centers are at the half distance between the successive holes at plate Y. In other words, the plate X holes centers are coincident with the air and gas center lines and are positioned at each half distance $s_{(n)}$ between two holes of the plate Y. For that, plate Y has one hole more in each cell than plate X. Also by trigonometric relations of right triangles X_aOXX_a and X_gOXX_g, the distances from the origin to the hole's centers of the plate X, $z_{X,a1}$, $z_{X,a2}$ ... $z_{X,a(n)}$ and $z_{X,g1}$, $z_{X,g2}$ ... $z_{X,g(n)}$ are computed using the following general correlations

$$z_{X,(n)} = z_{Y,(n)} + r_{Y,(n)} + \frac{s_{(n)}}{2}$$

$$\frac{r_{X,(n)} + \frac{w}{2}}{r_{Y,(n)} + \frac{w}{2}} = \frac{z_{X,(n)}}{z_{Y,(n)}} \tag{9}$$

As mentioned in Section 4.1, the core stagger plates sequence always starts and finish with plates type X. Thus, the core length is obtained by $l_{core} = n_Y th + n_X th$, where the number of plates X is obtained by $n_X = n_Y + 1$. The cOSF channels formed has its entrances at the plate X, where each air and gas hole of plate X correspond to a flow passage with its respective hydraulic diameter $D_{h,(n)}$. The channels assume different values of hydraulic diameter through the core height, since the holes radius change through the module height. The hydraulic diameter is calculated by its definition, $D_{h,(n)} = 4A_{o,(n)} th/A_{(n)}$, being A_o the minimum free-flow cross section area (sum of the two intersection circles, see Fig. 4.6) of the channel and A the channel wall contact area swept by the stream (wet surface). These areas are obtained for each channel by the following equations

$$A_{o,(n)} = r_{Y,(n)}^2 \cos^{-1}\left(\frac{u_{(n)}}{r_{Y,(n)}}\right) - u_{(n)}\sqrt{r_{Y,(n)}^2 - u_{(n)}^2} + r_{X,(n)}^2 \cos^{-1}\left(\frac{v_{(n)}}{r_{X,(n)}}\right) - v_{(n)}\sqrt{r_{X,(n)}^2 - v_{(n)}^2}$$

$$+ r_{X,(n)}^2 \cos^{-1}\left(\frac{uu_{(n)}}{r_{X,(n)}}\right) - uu_{(n)}\sqrt{r_{X,(n)}^2 - uu_{(n)}^2} + r_{Y,(n+1)}^2 \cos^{-1}\left(\frac{vv_{(n)}}{r_{Y,(n+1)}}\right) - vv_{(n)}\sqrt{r_{Y,(n+1)}^2 - vv_{(n)}^2}$$

$$u_{(n)} = \frac{r_{Y,(n)}^2 - r_{X,(n)}^2 + \left(z_{X,(n)} - z_{Y,(n)}\right)^2}{2\left(z_{X,(n)} - z_{Y,(n)}\right)}$$

$$uu_{(n)} = \frac{r_{X,(n)}^2 - r_{Y,(n+1)}^2 + \left(z_{Y,(n+1)} - z_{X,(n)}\right)^2}{2\left(z_{Y,(n+1)} - z_{X,(n)}\right)}$$

$$v_{(n)} = z_{X,(n)} - z_{Y,(n)} - u_{(n)}$$

$$vv_{(n)} = z_{Y,(n+1)} - z_{X,(n)} - uu_{(n)}$$

(10)

And,

$$A_{(n)} = 2\pi r_{X,(n)} th + 2\left(\pi r_{X,(n)}^2 - A_{o,(n)}\right) + \pi\left(r_{Y,(n)} + r_{Y,(n+1)}\right)th + \pi\left(r_{Y,(n)}^2 + r_{Y,(n+1)}^2\right) - 2A_{o,(n)} \tag{11}$$

At this point all the geometrical aspects of the recuperator are defined, including the dimensions, spacings, areas and channel hydraulic diameters. In sequence, the fluid flow and heat transfer in the recuperator are modeled.

4.3.2 Flow distribution over the core – Hardy Cross method

As previously described in Section 4.3.1, the core flow passages of each side are composed by cOSF channels with different hydraulic diameters $D_{h,(n)}$ disposed in the recuperator radial direction. All cOSF channels of the same side are communicating, and consequently, the flow is self-distributed over the channels, behaving similarly to a network of pipes. To calculate the mass flow rate in each cOSF channel the Hardy-Cross method was used [14][15]. This method applies the continuity of flow and continuity of potential to iterative solve the flows in a pipe network. The equilibrium between pressure and friction forces in steady and incompressible flow is assumed. The Hardy Cross technique requires that the head loss terms for each pipe in the system be expressed in the form of

$$h_{(n)} = i_{(n)} \dot{V}_{(n)}^2$$

$$i_{(n)} = \frac{\bar{\rho}}{g A_{ff(n)}^2} \left[2f \frac{1}{\rho_m} \left(\frac{l_{core}}{D_{h(n)}} \right) + \left(\frac{1}{\rho_o} - \frac{1}{\rho_i} \right) \right] \tag{12}$$

$$\dot{V}_{(n)} = \frac{\dot{m}_{(n)}}{\bar{\rho}}$$

where i is an equivalent resistance to channel for the entire recuperator core length and $\dot{V}$ is the volume flow rate in the channel. The absolute temperatures T_m and T_w are the fluid bulk mean temperature computed for the hot and cold sides and the wall temperature, respectively, by [16]

$$T_{a,m} = \frac{T_{a,i} + T_{a,o}}{2}$$

$$T_{g,m} = \frac{T_{g,i} + T_{g,o}}{2} \tag{13}$$

$$T_w = \frac{\left(T_{g,m}/R_g \right) + \left(T_{a,m}/R_a \right)}{\left(1/R_g \right) + \left(1/R_a \right)}$$

The Hardy-Cross method calculation procedure is not described for conciseness. A complete overview of the technique is described in detail by [15].

4.3.3 Heat transfer

The heat transfer in the counterflow recuperator core can be described by the well-known effectiveness-NTU relations present in the literature [17], with the effectiveness given by

$$\varepsilon = \frac{C_g \left(T_{g,in} - T_{g,out} \right)}{C_a \left(T_{g,in} - T_{a,in} \right)} \tag{14}$$

$$\varepsilon = \frac{C_a \left(T_{a,out} - T_{a,in} \right)}{C_a \left(T_{g,in} - T_{a,in} \right)} \tag{15}$$

$$\varepsilon = \frac{1 - \exp\left[-N_{tu}\left(1 - C_a / C_g\right)\right]}{1 - C_a / C_g \exp\left[-N_{tu}\left(1 - C_a / C_g\right)\right]}$$

(16)

Where,

$$C_a = \left(\dot{m}c_p\right)_a, C_g = \left(\dot{m}c_p\right)_g ; N_{tu} = UA / C_a$$

(17)

For the gas turbine recuperator, the air and gas mass flow rates are very similar and the specific heat of the gas (hot), are usually higher, leading to

$$C_a = C_{\min} ; C_g = C_{\max}$$

(18)

Using the Eqs. 13 and 14 it is now possible to calculate the two streams outlet temperatures

$$T_{a,out} = T_{a,in}\left(1 - \varepsilon\right) + \varepsilon T_{g,in}$$

(19)

$$T_{g,out} = T_{g,in} + \varepsilon\left(C_a / C_g\right)\left(T_{a,in} - T_{g,in}\right)$$

(20)

The overall heat transfer coefficient U_a based on the airside heat transfer surface area A_a is then evaluated from N_{tu}. The reciprocal of overall thermal resistance, is considered as having three components in series: (1) air-side thermal resistance, including the extended surface efficiency on the air side; (2) wall thermal resistance; and (3) steam-side thermal resistance, including the extended surface efficiency on the steam side:

$$\frac{1}{N_{tu}} = \sum_1^{n_g} \frac{C_a}{C_g}\left(\frac{\mathrm{Pr}^{2/3}}{\eta_o j}\frac{A_o}{A}\right)_{g,(n)} + \frac{w}{A_w k_w} + \sum_1^{n_a}\left(\frac{\mathrm{Pr}^{2/3}}{\eta_o j}\frac{A_o}{A}\right)_{a,(n)}$$

(21)

Where, A_w is the wall perpendicular heat transfer area $A_w = \left(r_{out} - r_{int}\right)l_{core}$ (heat conduction area), k_w is the wall material thermal conductivity. The Prandtl number $\mathrm{Pr}_{(n)}$, cOSF fin efficiency $\eta_{o,(n)}$, Colburn factor $j_{(n)}$ and the free-flow and heat transfer areas are obtained separately for each channel and the thermal resistance of each side is the sum in parallel of each channel thermal resistance. In sum, Eqs. 14 to 21 account for the effect of the duct geometry and flow properties on heat transfer performance.

4.3.4 Fluid flow

The outlet pressures $\left(p_{a,out} ; p_{g,out}\right)$ are determined from an analysis of the pressure drops experienced by the two streams,

$$p_{a,out} = p_{a,in} - \Delta p_a ; p_{g,out} = p_{g,in} - \Delta p_g$$

(22)

The pressure drop of each channel $\Delta p_{a,(n)}$ can be obtained with its entrance and expansion terms included, by

$$\Delta p_{a,(n)} = \frac{G_{a,(n)}^2}{2} \left[f \frac{A_{(n)}}{A_{o,(n)}} \frac{v_{a,m}}{v_{a,in}} + 2 \left(\frac{v_{a,out}}{v_{a,in}} - 1 \right) \right] \tag{23}$$

In the present case, once all channels of the same side are communicating, the pressure drop self equalizes resulting in equal values for all channels. Thus, the overall air side pressure drop Δp_a is computed by an average of the pressure drop across all channels, $\overline{\Delta p}_{a,(n)}$. The term $G_{(n)}$ is the mass velocity $\left(\dot{m}_{(n)} / A_{c,(n)} \right)$ and the average specific volume is $v_{a,m} = \left(v_{a,in} + v_{a,out} \right)/2$. The inlet and outlet specific volumes are based on the temperatures determined from Section 4.2.4. A similar expression holds for $\Delta p_{g,(n)}$. To calculate the Colburn factor and friction factors that appear in Eqs. 21 and 23 is used the circular offset strip fins model [Chapter 3].

4.3.5   Dimensionless number on the circular offset strip fins

The Reynolds number is obtained by its definition,

$$\mathrm{Re}_{a,(n)} = \frac{G_{a,(n)} D_{ha,(n)}}{\mu_a} \tag{24}$$

The cOSF Colburn factor and Fanning friction factor are represented respectively by, for the Reynolds range of 500<Re<3500

$$j = 0.02\,\mathrm{Re}^{-0.143} \delta^{0.02} \gamma^{-0.235} \tag{25}$$

$$f = 0.715\,\mathrm{Re}^{-0.331} \delta^{0.279} \gamma^{-0.149} \tag{26}$$

Where δ and γ are geometrical ratios given by

$$\delta = \frac{s_{(n)}}{th_{(n)}}; and \gamma = \frac{s_{(n)}}{d_{(n)}} \tag{27}$$

With the outlet conditions defined, a thermodynamic optimization is suggested to identify the proportions which minimize the losses.

4.3.6   Entropy generation minimization recuperator core design

A thermodynamic optimization method is used to design the architecture (shape, sizes) of the counterflow recuperator core, with the objective to minimize the entropy generation rate. The entropy generation minimization (EGM) thermodynamic optimization tool aims to identify trends and the existence of optimum geometrical relations [18].

Let's consider the recuperator core with the geometrical relations described in Sections 4.3.1. The air and gas streams are modeled as ideal gases, with their respective mass flow rates $\left(\dot{m}_a, \dot{m}_g \right)$ and inlet conditions $\left[\left(T_{a,in}, p_{a,in} \right) and \left(T_{g,in}, p_{g,in} \right) \right]$ given. The outlet conditions

$\left[\left(T_{a,out}, p_{a,out} \right) and \left(T_{g,out}, p_{g,out} \right) \right]$ are obtained by Eqs. 19, 20 and 22. The dimensionless entropy generation number is evaluated in terms of inlet and outlet temperatures and pressures ratios by

$$N_S = \frac{C_g}{C_a} \left[\ln \frac{T_{g,out}}{T_{g,in}} - \left(\frac{R}{c_p} \right)_g \ln \frac{\Delta p_g}{p_{g,in}} \right] + \ln \frac{T_{a,out}}{T_{a,in}} - \left(\frac{R}{c_p} \right)_a \ln \frac{\Delta p_a}{p_{a,in}} \tag{28}$$

The entropy generation number can be separated into two terms, one associated with the temperature gradients and the other with the pressure drop,

$$N_S = N_{ST} + N_{SP} \tag{29}$$

where

$$N_{ST} = \frac{C_a}{C_e} \ln \frac{T_{a,out}}{T_{a,in}} + \ln \frac{T_{g,out}}{T_{g,in}} \tag{30}$$

$$N_{SP} = -\frac{C_a}{C_{min}} \left(\frac{R}{c_p} \right)_a \ln \left(1 - \frac{\Delta p_a}{p_{a,in}} \right) - \frac{C_g}{C_{min}} \left(\frac{R}{c_p} \right)_g \ln \left(1 - \frac{\Delta p_g}{p_{g,in}} \right) \tag{31}$$

4.3.7   Recuperator design code

A design code was developed with Matlab® containing all the mathematical formulation previously described. Figure 4.8 presents the design code routine flowchart. In the code, the geometrical constraints and thermal conditions are fed as input variables. The heat transfer and fluid flow equations are solved iteratively, providing the recuperator performance for different configurations and conditions. The thermal input variables are: air and gas mass flow rates $\left(\dot{m}_a, \dot{m}_g \right)$ (hot and cold sides), with its respective inlet temperatures $\left(T_{a,in}, T_{g,in} \right)$ and pressures ($p_{a,in}$, $p_{g,in}$). The geometrical inputs are separated in optimizable and non-optimizable variables. The non-optimizable geometrical input variables are: the recuperator inner diameter d_{inn}, the minimum space sp, the wall thickness separating the streams w and the number of modules n_{mod}. The recuperator has 6 optimizable free degrees, which are: the number of air and gas cells contained in a module $n_{cell,mod}$, the cold and hot side channels hydraulic diameters (ratio between $d_{a,1}/d_{g,1}$), the outer diameter d_{out}, the core axial length l_{core} and the unitary cell length th. With the input geometrical variables, the code directly defines all the geometrical dimensions using the Eqs. 1 to 11. In sequence, an initial guess value of effectiveness is suggested, allowing to compute both of stream outlet temperatures. With the total mass flow rates, the fluid properties at the average inlet and outlet temperature and the hydraulic diameter of the channels, the flow distribution in the channels is obtained with its respective Reynolds number providing the total pressure drop. A new outlet temperature for both streams is then obtained applying the Reynolds number with the cell dimensions with the Eqs. 12 to 27. A new value of effectiveness is found using Eq. 16. If this value approaches the initial effectiveness guess value the code provides the variables output, otherwise it keeps on

integrating until the similarity criteria is reached. By varying a particular input variable in a range while keeping other dimensions constant, the influence of each freedom degree was accessed in terms of entropy generation, using the Eq. 28 to 31. The complete analysis of the code design procedure is presented in Section 4.5. The design code was validated with CFD and experimental data. The validation procedure is described in sequence.
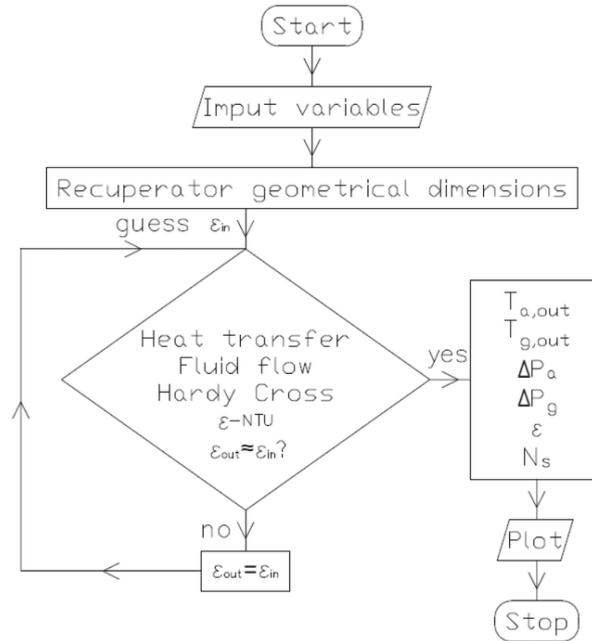

Figure 4.8 – Recuperator design code flowchart.

4.4 Numerical method and design code validation

The recuperator design code validation was done in two steps. First, a computational fluid dynamic (CFD) study using Ansys Fluent R.3 was done reproducing the experiments performed in Chapter 3. The mesh and Fluent settings which resulted in the lower error in respect to the experimental data were defined as standard. Then, using the same mesh and Fluent settings, a recuperator section was numerically evaluated, and the results were used to validate the designing code.

4.4.1 Numerical method validation with experimental data

The numerical method used to validate the recuperator design code was in turn validated with experimental data. For that, two of the five cores containing the circular offset strip fins geometry tested experimentally in Chapter 3 were reproduced numerically using the CFD software Ansys Fluent 2019 R3, V.19.5.0. The computational domain was modeled using the Ansys Design Modeler software, where only the fluid domain was reproduced. Figure 4.9 shows the numerical domain of the cores I and III simulated on Ansys Fluent with its respective assumed boundary conditions and flow section view on plate X. All the dimensions of the cores are presented in Chapter 3.
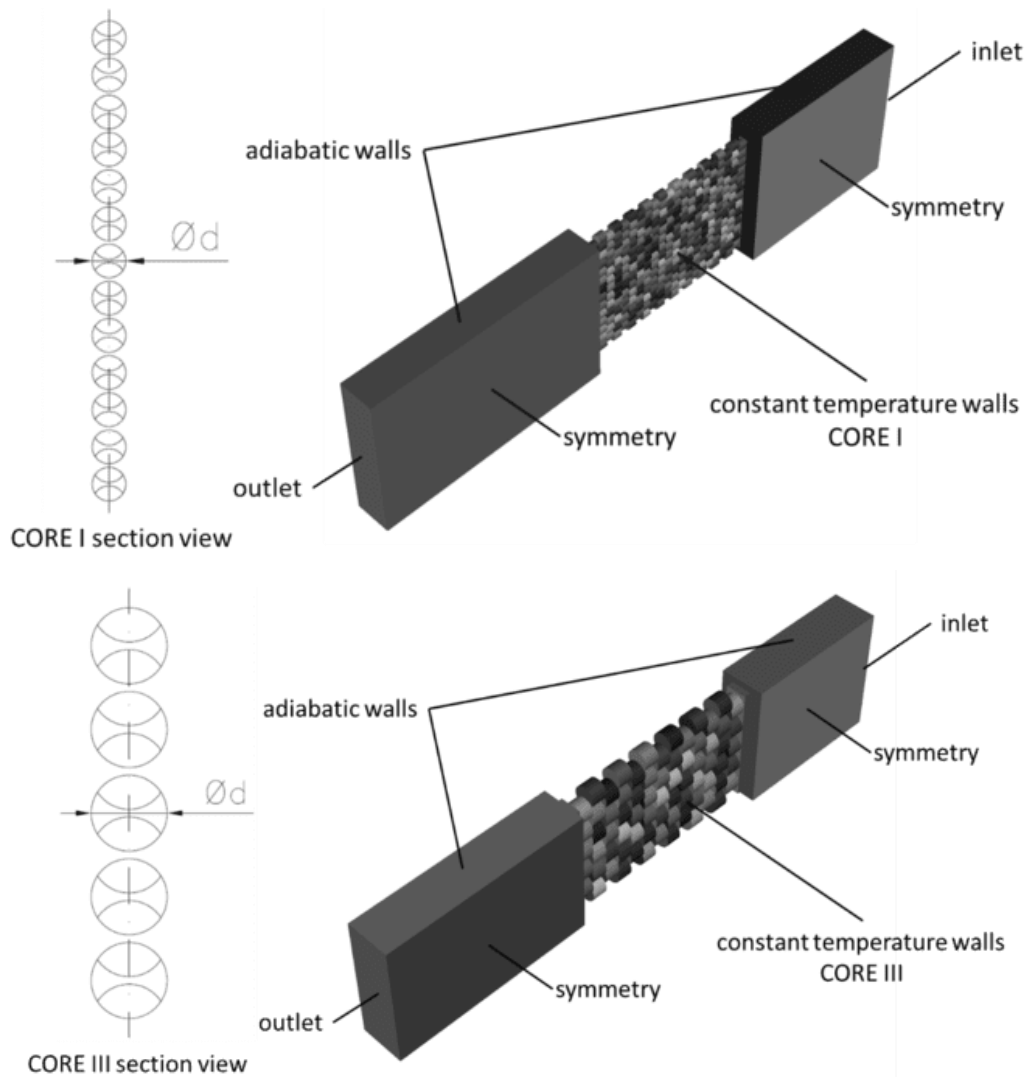
Figure 4.9 – CFD domain, cOSF cores I and III with its respective boundary conditions.

The cores dimensions, the temperature and pressure measurement points, lengths and the boundary conditions were set the same as the experiments described in Chapter 3. The core tested experimentally has 3 columns with cOSF. To reduce the computational cost, only the fluid volume of one column was simulated with different meshes to access the one which produced the lower numerical error, in comparison with the experimental data. The mesh was generated using the Fluent Meshing Watertight software. First, a mesh refinement study was done in CORE III to check the grid independence of the mesh. A flow with fixed Reynolds number of 1900 at 220° wall temperature was evaluated with different combinations of the mesh parameters in grid independence study. The grid independence study is presented in Section 4.5.1 with a scatter chart comparison between the numerical and experimental results for the temperature and pressure results. Table 4.4 shows the mesh settings for which the grid independence was achieved. The parameters not mentioned in the table were maintained as the software standard. This mesh was used to reproduce all the experiments of the core I and III and its results were compared with the experimental data on Section 4.5.2. As just one mesh was used, at different mass flow rates, different hydrodynamic boundary layer thickness was obtained with consequent different y+ values. The mesh region near the fluid walls was generated so that the

average y+ does not exceed the value of 0.5, independent of the Reynolds number flow. These mesh settings were also used for the simulations of the recuperator section.

Table 4.4 - Mesh settings used on the Fluent watertight

Mesh settings Fluent watertight	
Local sizing	no
Surface mesh	
Minimum size	0.1
Maximum size	0.5
Growth rate	1.2
Size functions	Curvature
Curvature normal angle	0.0001
Describe geometry	
Geometry type	Only fluid regions with no voids
Share topology	no
Volume mesh	
Boundary layer settings on fluid walls	
Offset method type	Uniform
Number of layers	12
Growth rate	1.2
First height	0.008
Volume settings	
Fill	Polyhedra
Growth rate	1.2
Max cell length	0.5

Different Fluent settings were also evaluated in order to identify the setup which provides the best agreement with the experimental data of the Cores I and III. The Fluent settings used in the CFD analysis is described in sequence: Steady state, pressure-based with absolute velocity solver and the model k-omega SST. The NIST real gas model for air was used to take into account the air properties variations with the temperature change through the heat exchanger. The calculations were performed with the solution method SIMPLE (Semi-Implicit Method for Pressure Linked Equations), with the following spatial discretization settings: Gradient – last squares cell based, pressure – second order and momentum, turbulent kinetic energy, specific dissipation rate and energy with second order upwind. The hybrid initialization was used to initialize the calculations.

The CFD results were compared with the experimental data in terms of heat transfer rate, pressure drop and mass flow rate. In sum, 31 tests were numerically reproduced with the results with an average error of 3.2% for heat transfer rate and 22.7% for the pressure drop predictions.

4.4.2   Design code validation domain

A recuperator section was numerically evaluated using the mesh and the Fluent settings defined in the Section 4.3.1. Fig. 4.10 shows the CFD domain with the assumed boundary conditions and the section view of the recuperator flow passages at plate X. The recuperator domain, generated using the relations described in Section 4.3.1, contains 20 cOSF flow channels with 41 stacked plates of 3 millimeters, resulting in 123mm length. Note that the recuperator

channels have different hydraulic diameters through its height, being the first channel with a diameter of d_1=2.0mm and the last d_{20}=4.43mm. The domain with large channels diameter difference was chosen to observe the channels influence in the flow, including the flow distribution, heat transfer and pressure variation. Heating and cooling at constant wall temperature boundary condition were evaluated at different air flow rates in the CFD study. To reproduce the constant wall temperature boundary condition in the design code, one of the mass flow rates was increased to reduce the thermal resistance of that side and promote the condition of constant wall temperature on the other recuperator side. The main geometrical dimensions, thermal and hydrodynamic conditions and mesh characteristics are presented in Table 4.5. In all simulations the Reynolds number on the channels remained in the range of 500 to 3500, which is inside the range for which correlations (Eqs. 25 and 26) are valid. The simulations were considered converged when, after 1000 iterations, the simulation was conservative with the outlet mass flow rate difference lower than 0.03%, and the inlet and outlet pressures and temperatures residuals were below 10^{-4}. The numerical results are evaluated in terms of temperature and pressure difference from the inlet and outlet and the mass flow rate distribution through the channels. These results are compared with the recuperator design code output in Section 4.5.3.

Table 4.5 - Recuperator CFD domain and boundary conditions.

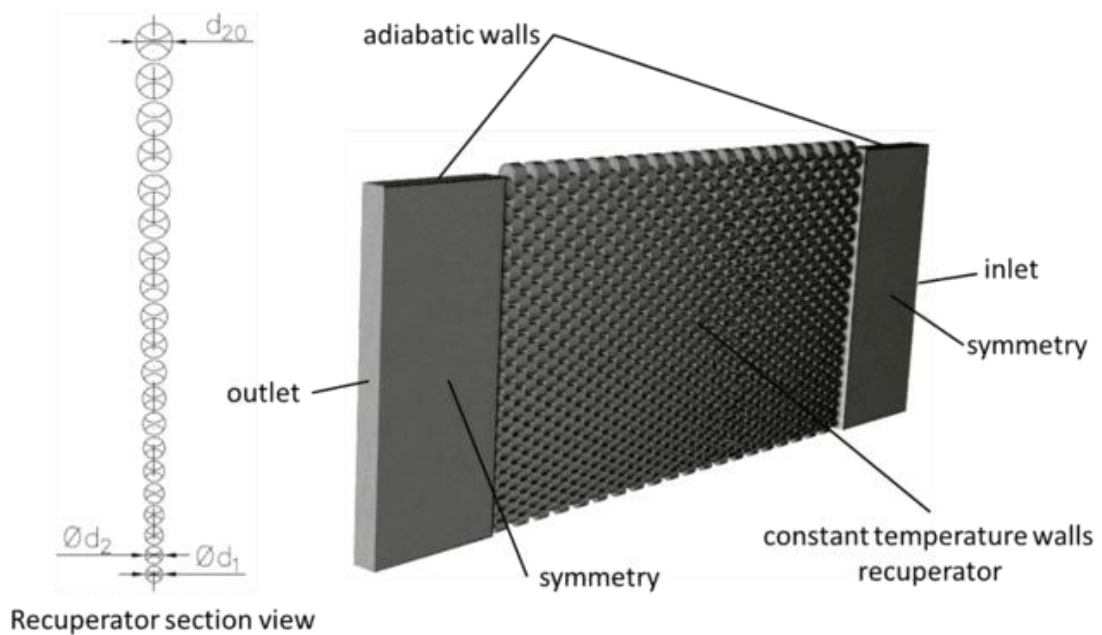| Recuperator CFD domain	
Geometrical	
Number of channels	20
Passages obstruction degree, k, Eq. (2.2)	0.1
d_1 [mm]	2
d_{20} [mm]	4.43
Number of unitary cells on axial direction	41
Unitary cells lentgh, th [mm]	3 mm
Total number of unitary cells in the domain	840
Thermal and hydrodinamic	
Heating	
Inlet temperature [K]	533.15
Outlet pressure [Pa]	661,000
Wall temperature	781,15
Air mass flow rate range [kg/s]	0.00185 to 0.00388
Cooling	
Inlet temperature [K]	781.15
Outlet pressure [Pa]	101,325
Wall temperature	533.15
Air mass flow rate range	0.00185 to 0.00388
Mesh size	
Cells	39,033,727
Faces	181,269,539
Nodes	109,999,047

Figure 4.10 – Recuperator domain used to compare and validate the recuperator design code with the CFD simulations.

The results generated with the domains and procedures here described are discussed in the next section.

4.5 Results

In this section, first the grid independence study used to define the mesh and Fluent setting which best reproduce the experimental data is presented. In sequence, the numerical results at different Reynolds number are compared with the experimental data to validate the numerical method. The validated numerical method was used to validate the proposed recuperator design code. An entropy generation minimization analysis was carried out to evaluate the influence of each optimizable variable in the recuperator performance. Finally, the design code was used to design four recuperators for different turbine sizes: 100kW, 100kW_beta, 1250kW and 5000kW.

4.5.1 CFD mesh independence study

The CFD numerical tool Ansys R2019 R3 v.19.5.0 software was used to predict the thermal and hydrodynamic flow in the cOSF in the recuperator core. For that, to improve the accuracy of the numerical results, a mesh study was made to identify the mesh characteristics and the Fluent parameters that best describe the experimental data. The mesh study was performed varying the number of elements and the mesh refinement region on the cOSF flow passages. An experimental data point of CORE III (Re=1903 and Tw=220°C) was simulated with different mesh parameters and Fluent settings in the analysis. The numerical/experimental comparison was made in terms of experimental measured variables, i.e., pressure drop across the core and the heat transfer rate under steady mass flow rate. The k-w SST turbulence model was used in the simulations due to the high turbulence characteristics in the cOSF passages. Independent of the number of elements, all simulations have an y+ lower than 1, necessary condition for the k_w SST turbulence model. Fig. 4.11 and 4.12 show the heat transfer rate and the pressure drop through the core with different mesh sizes. It is possible to observe that after

19 million elements no significant improvements were observed, with the CFD results within the experimental uncertainty range. The mesh and Fluent settings selected to be used in the computational analysis match the experimental results within 1.9% and 2.9% error for pressure and heat transfer rate respectively. Ideally, each flow Reynolds number would have its own mesh study due to the thermal and viscous boundary layer changes. However, a complete analysis would become very timely and computationally expensive and was not performed. With the mesh and Fluent parameters defined in the mesh study, the experimental tests performed on CORE I and CORE III described in Section 4.4.1 were reproduced with Fluent for all Reynolds tested experimentally.
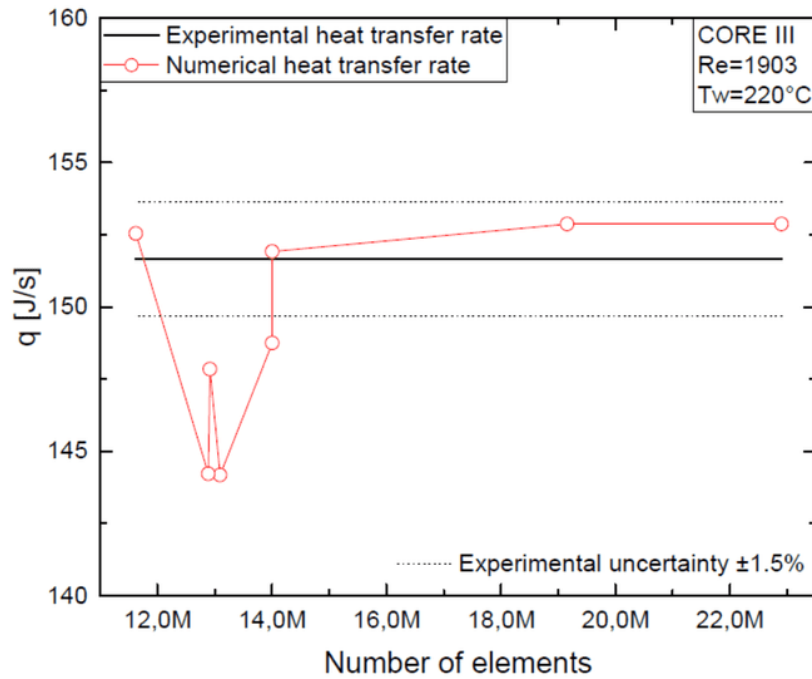

Figure 4.11 - Influence of the mesh number of elements on the numerical heat transfer rate on the CORE III.
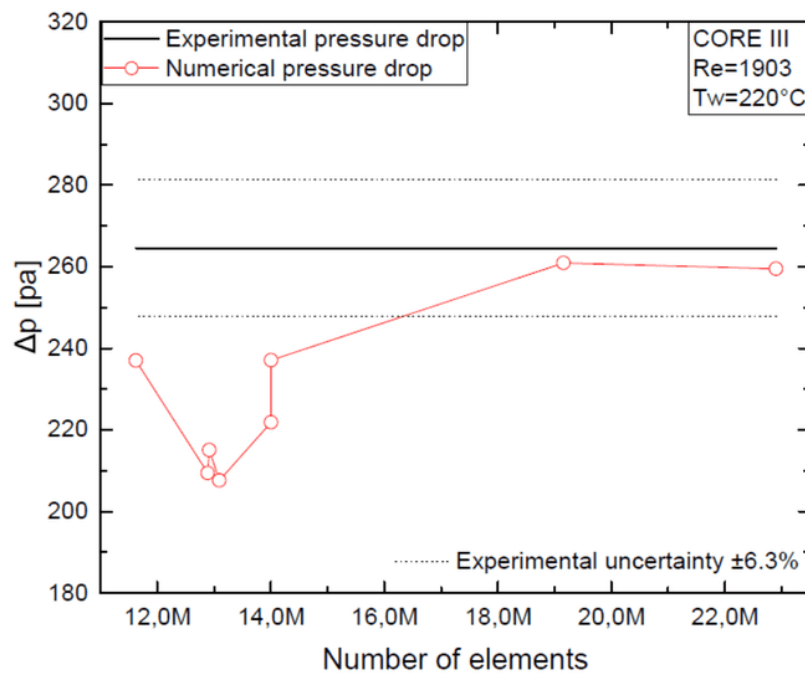

Figure 4.12 - Influence of the mesh number of elements on the numerical pressure drop on the CORE III.

4.5.2 Validation of the numerical results with experimental data

The mesh and Fluent settings defined in Section 4.5.1 were used to reproduce the entire Reynolds range data of cOFS CORE I and III at two different constant temperature walls (Tw=170°C and Tw=220°C). The scatter plots of Figs. 4.13 and 4.14 show the comparison of the numerical and experimental heat transfer rate and pressure drop data, respectively. The black line crossing the plot, in both figures, represents the perfect match of the numerical and experimental data, with the two doted lines indicating a variation in a percentual range. The scatters correspond to the experimental data of the two cores at different Reynolds numbers and constant wall temperatures. The numerical heat transfer rate agreed in average with the experimental data within 3.2%, while the pressure drop within 22.7%. The points out of the ±5% margin for the heat transfer rate and ±25% margin for the pressure drop were obtained at low Reynolds number ranges, where the experimental uncertainties are bigger. Furthermore, these data points may also be in a non-fully turbulent flow regime, reducing the accuracy of the numerical model k-w SST used to solve the viscous equations. The CFD numerical tool, with the selected mesh and Fluent parameters provide results that agreed well with the experimental data and is considered validated to be used for different cOSF dimensions at different flow and temperature conditions.
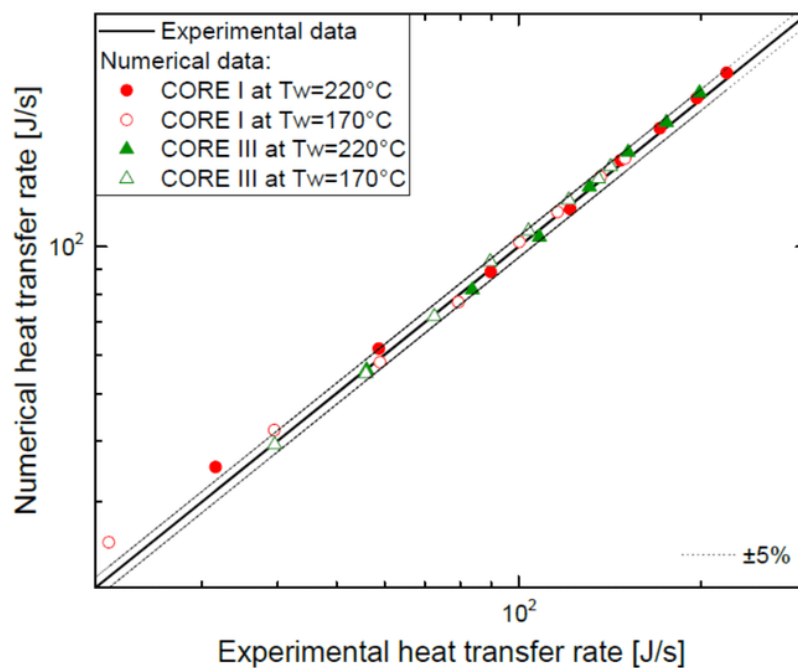

Figure 4.13 - Comparison of numerical predictions for heat transfer rate with experimental data for offset strip fin cores listed in Table 3.1.
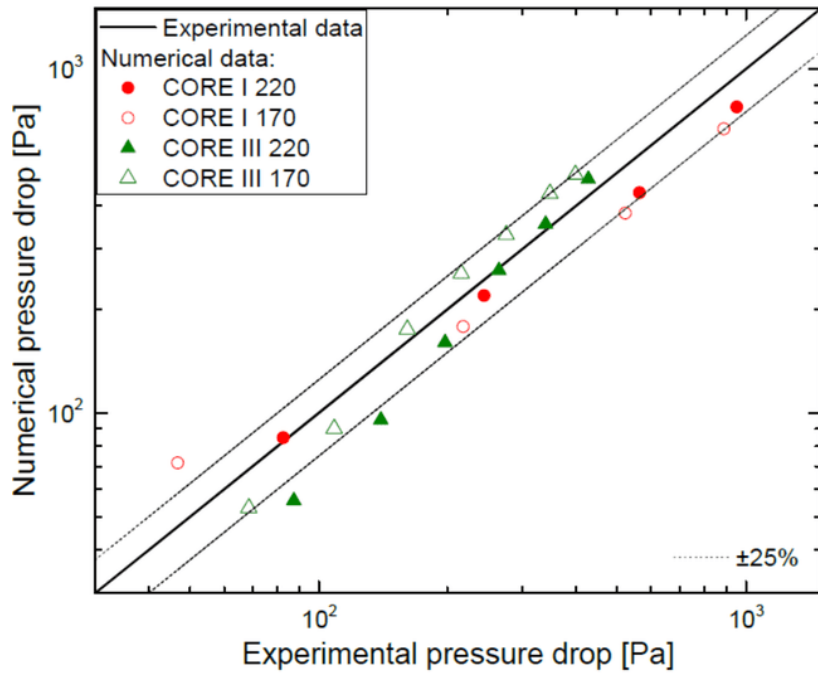
Figure 4.14 - Comparison of predictions for delta p given by Eq. (24) with experimental data for offset strip fin cores listed in Table 3.1.

4.5.3 Design code validation with numerical data

The design code which contains the mathematical model described in Section 4.3, used to predict the recuperator thermal hydraulic performance, is now compared, and validated with the validated CFD simulations. The evaluation was made for air heating and cooling at constant temperature walls boundary condition. The main dimensions and characteristics of the computational domain and thermal-hydraulic conditions used as input for the simulations and for the design code are detailed in Section 4.2.

The axisymmetric configuration of the cOSF recuperator results in channels with different hydraulic diameters through the radial direction. The communicating channels characteristic of the cOSF allow the flow to self-distribute through the recuperator core. Consequently, the mass flow rates in the channels vary according to their hydraulic diameter. The design code uses the Hardy-Cross method, described in Section 4.3.3, to calculate the mass flow rate of each channel. Fig. 4.15 shows the comparison of the numerical mass flow rate with the mass flow rate estimated by the Hardy-Cross method. Each scatter corresponds to the mass flow rate at each channel of the core. The Hardy-Cross method provides the channel average mass flow rate, while by the numerical method, the mass flow rates were taken at the entrance and exit of the recuperator core (full and empty scatter respectively). The Hardy-Cross method and the numerical mass flow rates estimations agreed by 4% on average. The best agreement is observed for higher mass flow rates channels, or the outer channels of the core. The mass flow rate difference at the smaller hydraulic diameter channels may be attributed to the transitional and laminar flow regimes observed in these channels, which are not well represented by the k-w SST turbulent model used in the numerical solver. A velocity contour plot that illustrates this effect is discussed further below. Furthermore, the channels with lower agreement have low mass flow rates and consequently have lower influence in the temperature and pressure results, since they are pondered by mass.
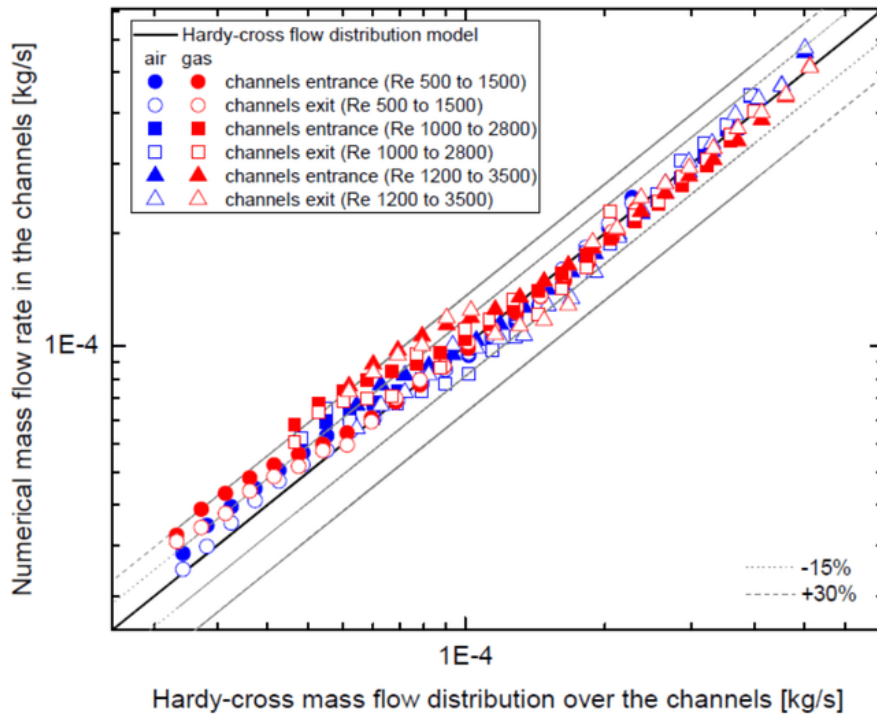
Figure 4.15 - Comparison of predictions for the Hardy-cross mass flow rate given by Eq. (12) with numerical data for cOSF core domain described in Section 4.2.

The scatter plot of Figs. 4.16 and 4.17 shows the comparison of the heat transfer rate and the pressure drop predictions for the simulations and the design code, respectively. The results are agreed with an average error of 0.9% for the heat transfer rate and ±11% for the pressure drop. It can be noted that there are discrepancies between the numerical and the code pressure drop results at high Reynolds, but mainly at low Reynolds numbers. As mentioned before, the flow at lower Reynolds numbers may not be at a fully turbulent condition, resulting in uncertainties for the k-w SST turbulent viscous model. The good agreement observed in this analysis validates the thermal and pressure drop prediction of the design code output, allowing it to be used to evaluate the different recuperator dimensions and conditions.
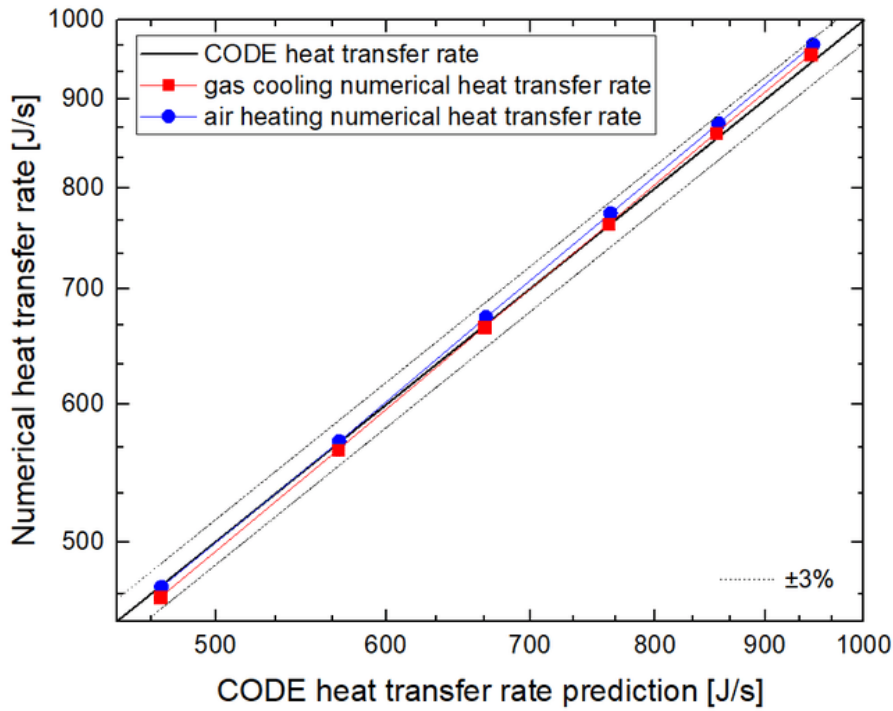
Figure 4.16 - Comparison of numerical predictions for heat transfer rate with numerical data for the recuperator domain described in Section 4.2.
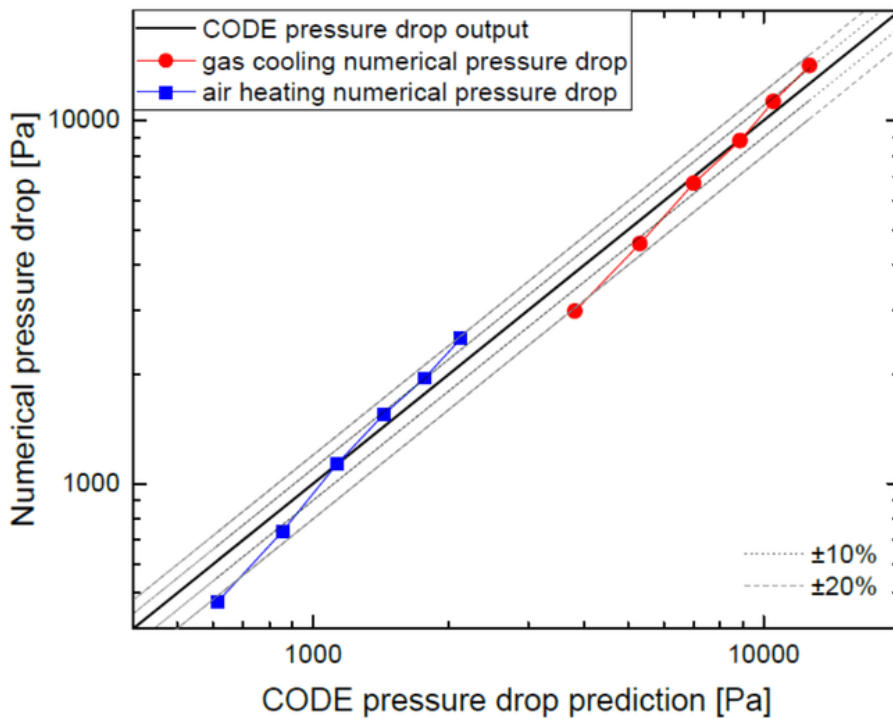
Figure 4.17 - Comparison of numerical predictions for pressure drop given by Eq. (24) with numerical data for the recuperator domain described in Section 4.2.

For illustration purposes, Fig. 4.18 shows the velocity, temperature, and pressure contours through the recuperator core domain. The simulation contours were generated for the heating condition at constant wall temperature with the Reynolds number at the channels varying from 850 to 2400 for the lower to the top channels. The flow is developed from the right to the left in all contour plots.

The velocity contours exhibit flow configurations through the core. At the entrance (right hand side of the figure) it is possible to visualize the laminar/transition flow in all channels. The flow seems to be developed to the fully turbulent faster at the outer portion of the core. The lower/middle region shows undefined velocities, which may represent the transition flow regime. At the bottom of the figure, the channels have smaller hydraulic diameters, having proportionally lower mass flow rates, resulting in low Reynolds number flow of the order of 850. In these channels it is possible to identify more constant velocities, which may characterize the fully laminar regime.

At the middle of the Fig. 4.18 the static temperature contours of the recuperator core domain is shown. The flow temperature seems to reach higher levels at the lower part of the core. This is expected to be due to the lower mass flow rates passing through this channel, in comparison with the channels placed at the top of the figure. The flow temperature looks homogeneous at the core exit.

The lower contour plot of the same figure shows the pressure distribution through the recuperator core. For a specific core length (axial distance x), the pressure seems to be higher at the lower hydraulic diameter than to the higher hydraulic diameter channels placed on the top of the core. At the core exit, the pressure tends to equalize, satisfying the flow distribution condition, where the flow is self-distributed to reach the same pressure drop in all the channels.
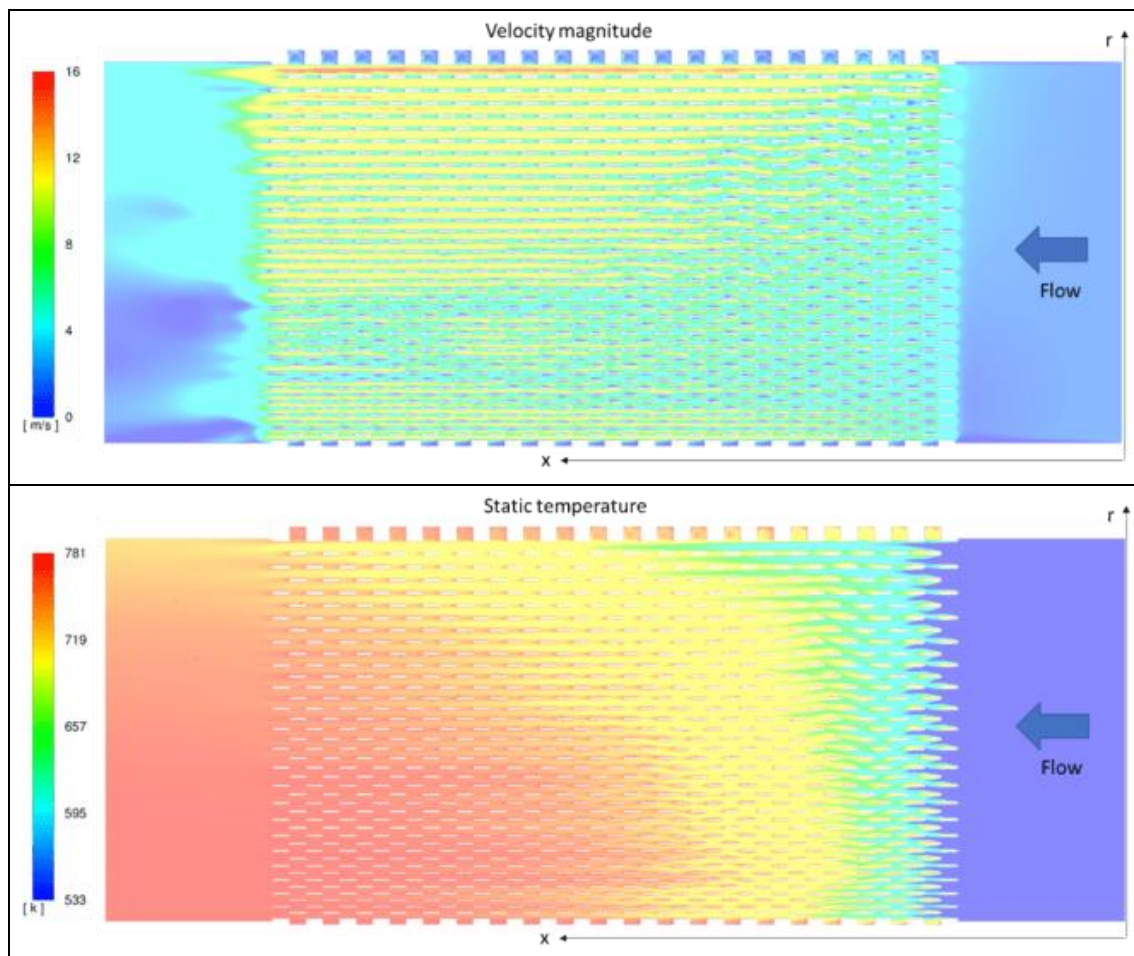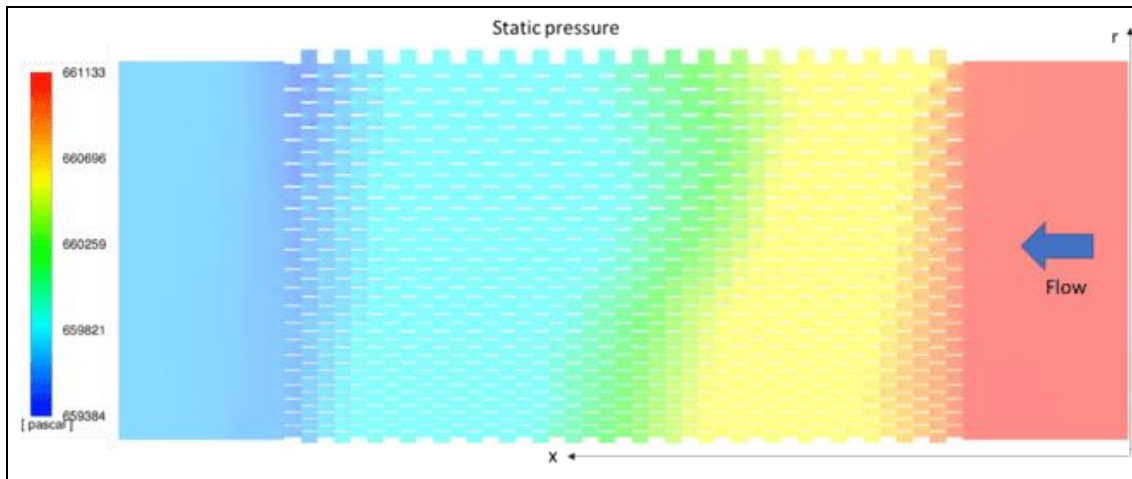
Figure 4.18 - From the top to the bottom, the velocity, temperature and pressure contours of the numerical simulation performed at the domain described on the Section 4.2 on heating condition at constant wall temperature (the flow direction is from the right to the left).

4.5.4 Diffusion bonded recuperator study cases

The counter-flow recuperator architecture (shapes, sizes) was designed by thermodynamic optimization (entropy generation minimization EGM) analysis. The cost minimization evaluation was not considered in the present study. The procedure described in sequence aims to identify tendencies and the optima structural characteristics. The design target is to define the recuperator complete dimensions which provide greater effectiveness by respecting the stipulated pressure drop limits. As mentioned in the Section 4.3.7, the flow passages in the present recuperator concept have six optimizable freedom-degrees: number of cells contained in a module, air/gas flow passage ratio, recuperator core length, recuperator core height, unitary cell length and the channel obstruction degree. The other parameters such as wall thickness, recuperator inner diameter, minimum space, number of modules contained in the recuperator are not optimizable and were kept constant in the analysis.

Four study cases of recuperators for different gas turbine sizes, 100kW (6.6 pressure ratio), 100KW (4.6 pressure ratio), 1250KW (6.6 pressure ratio) and 5000KW (6.6 pressure ratio) were evaluated with the present design procedure. The main flow conditions and dimensional constraints for each case are shown in Table 4.6. These parameters are used as input for the design procedure.

Table 4.6 – Recuperator input design parameters for four turbine sizes 100kW (6.6 pressure ratio), 100KW (4.6 pressure ratio), 1250KW (6.6 pressure ratio) and 5000KW (6.6 pressure ratio).

Thermal-hydraulic parameters		100 KW	100 KW_beta	1250 KW	5000 KW
compressor/turbine pressure ratio	-	6.6/6.0	4.6/4.135	6.6/6.0	6.6/6.0
material	-	SS-A304L	SS-A304L	SS-A304L	SS-A304L
m_dot_a	[kg/s]	0.584	0.6244	6.68	26.72
Ta,in	[°C]	266	208	260	260
Pa,in	[Pa]	661894	461320	661894	661894
air side maximum pressure losses	[%]	1.5	1.17(e80%) 1.5(e90%)	1.5	1.5
m_dot_g	[kg/s]	0.59	0.63	6.75	27.0
Tg,in	[°C]	518	591	508	508
Pg,in	[Pa]	105508	105508	105508	105508

gas side maximum pressure losses	[%]	4	4	4	4
m_dot_fuel	[kg/s]	0.006	0.0056	0.070	0.28
Targuet effectiveness	[%]	80/90	80/90	70	70
Dimensional parameters					
dinn	[m]	0.25	0.25	0.5	1.0
space_min	[m]	0.015	0.015	0.015	0.015
t_wall	[mm]	1(e80%) 0.7(e90%)	1	1	1
n_cell_mod	-	3(e80%) 4(e90%)	3(e80%) 4(e90%)	4	7
n_mod	-	36	36	36	36
k factor	-	0.1	0.1	0.1	0.1

4.5.5 Non-optimizable variables

The non-optimizable parameters of Table 4.6 are listed in sequence. The number of modules n_mod contained in the recuperator, which doesn't influence thermal performance, but it is relevant for the manufacturing, thermal-stress, and maintenance. The air/gas separating wall thickness (heat conduction wall) is an empirical parameter that is defined by the diffusion bonding process limitation. It should be defined as minimum as possible. Further research should be done to evaluate the minimum wall thickness acceptable for the diffusion bonding process. The channel obstruction degree also should be kept as small as possible, according to the analysis present in Chapter 3. The number of air and gas cells contained in a module should be kept as high as possible. The higher the number of cells contained in the modules the higher is the heat transfer area A_{HT}, Eq. (11), and consequently the more effective is the recuperator for a defined volume. However, the number of cells contained in each module is restricted by the manufacturing process, due to the plates machining method with the minimum manufacturable hole diameter. The minimum hole diameter considered on the present study is conservative, non-assuming hydraulic diameters smaller than 1.8E-3m. For reference purposes, some other recuperators present in the market, have channels with hydraulic diameter of a third of a millimeter [19][20]. The flow passage hydraulic diameter used in the recuperator is mandatory on the volume of the recuperator for a defined effectiveness. Smaller flow passages provide high heat transfer area and consequently require smaller volumes to reach the same effectiveness, when compared with bigger flow passages.

4.5.6 Optimizable variables (entropy generation minimization)

The optimizable variables are defined based on the minimum entropy generation design procedure described in Section 4.3.6. The recuperator design is made in four steps. First, the procedure identifies the air/gas hydraulic diameter relation which provides the minimum entropy generation. This step is very dependent on the fluid flow condition of each side, such as the pressures at inlet and outlet. The second step defines the core length to reach the target effectiveness. This parameter is limited by the design constraint such as restricted core length and the maximum acceptable pressure drop for each side. The third step defines the recuperator outer diameter. Varying the outer diameter controls the number of channels in the radial direction contained in the recuperator core. This is used to define the best Reynolds number flow regime for the recuperator operation. Finally, the four and last step evaluates the unitary

cell length, or the best plate thickness for the plates X and Y which provides the lowest entropy generation. The design process is iterative, after finding the minimum entropy outputs the design code is updated and all the steps are repeated until convergence is reached.

In the first step the air and gas first hole ratio, $r_{Y,a1}/r_{Y,g1}$, is varied while holding the other parameters fixed. The optimization of $r_{Y,a1}/r_{Y,g1}$ amounts to selecting the channel opening ratio, i.e., the optimum relation between the air and gas flow passages. As shown in Fig. 4.19, an optimal set of spacings is observed because the entropy generation rate associated the pressure drops increases in both extremes, $r_{Y,a1}/r_{Y,g1} \square 4$ and $r_{Y,a1}/r_{Y,g1} \square 4$ in all the study cases. The entropy generation rate contributed by imperfect thermal contact, N_{ST} , is relatively insensitive to varying the channel spacings. The recuperator effectiveness also shows itself to be relatively insensitive to the flow passages relation. In all cases, the optimum air/gas passage spacing showed to be around 1:4. The optimum value found for $r_{Y,a1}/r_{Y,g1}$ varies with the change of the other dimensions. Numerical optimization is iterative, thus, after the next phases of the numerical optimization, this step should be done again until convergence is reached. The "saw teeth" or the "jumps" observed in the pressure entropy curves are attributed to the number of channels contained in the cells. The change of the channel size may change the number of channels that fit in one cell at the radial sense, which affect directly the flow distribution and consequently the pressure drop, and pressure drop irreversibility.

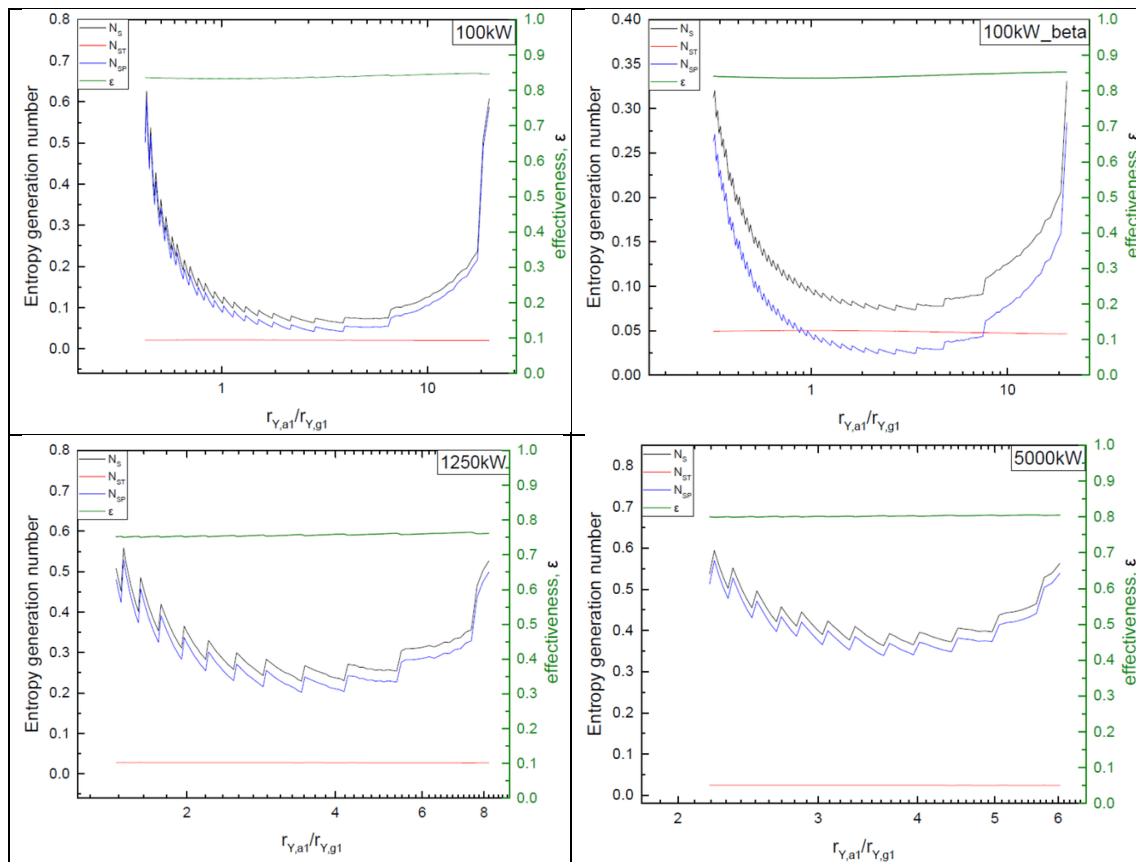*Figure 4.19 - The minimization of the entropy generation rate with respect to the ratio of channels diameters.*

The second step evaluates entropy generation number with the total recuperator heat transfer area. The recuperator core length l_{core} is evaluated in respect to the recuperator inner diameter $d_{inn,}$ which is kept constant during the analysis. Fig. 4.20 shows that for all study cases

this variable doesn't present an optimum minimum value, as the entropy generation rate N_S tends to increase with the core length. The irreversibility due to heat transfer decreases steadily with l_{core} increases. The opposite behavior is observed with the pressure-drop irreversibility N_{SP}. The corresponding effectiveness increases as more contact surface is built into the heat exchanger. The recuperator core length is beneficial for the effectiveness and generally constrained to the maximum acceptable length or due the maximum pressure drop defined for the component.
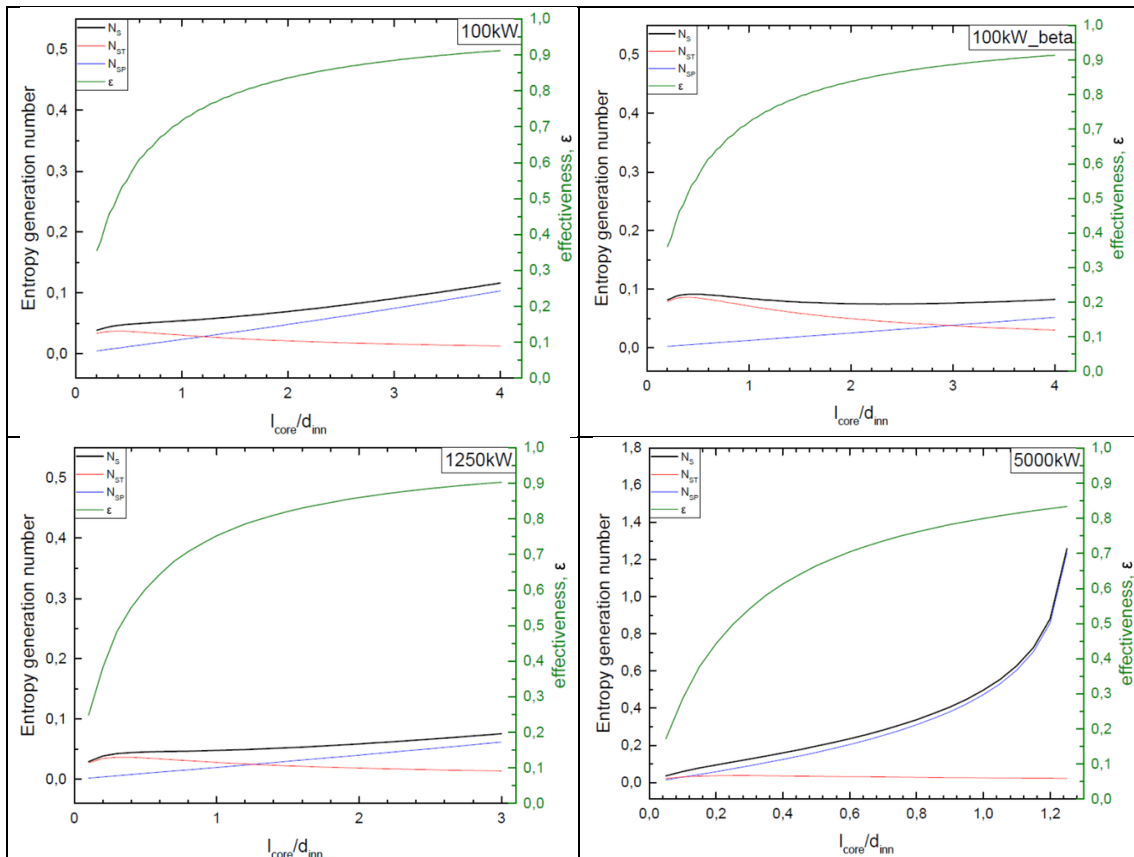

Figure 4.20 - The total entropy generation rate, pressure drop and heat transfer irreversibility and effectiveness with respect to the recuperator heat transfer area (core length).

The third step is to evaluate the optimum recuperator operation Reynolds number flow regime. The recuperator outer diameter, d_{out}, can control the flow velocities in the channels, where its bigger outer diameters increase the number of channels contained on the air and gas cells allowing the flow to be distributed and consequently reducing the average velocities and Reynolds numbers in each channel. Fig. 4.21 shows that in all cases, a preferable minimum outer diameter is observable to keep the pressure-drop irreversibility controlled. Lower values than this point increase substantially the pressure drop, and bigger values don't cause significant entropy generation reduction. The thermal irreversibility and the recuperator effectiveness are not much sensible to the variation of this parameter.
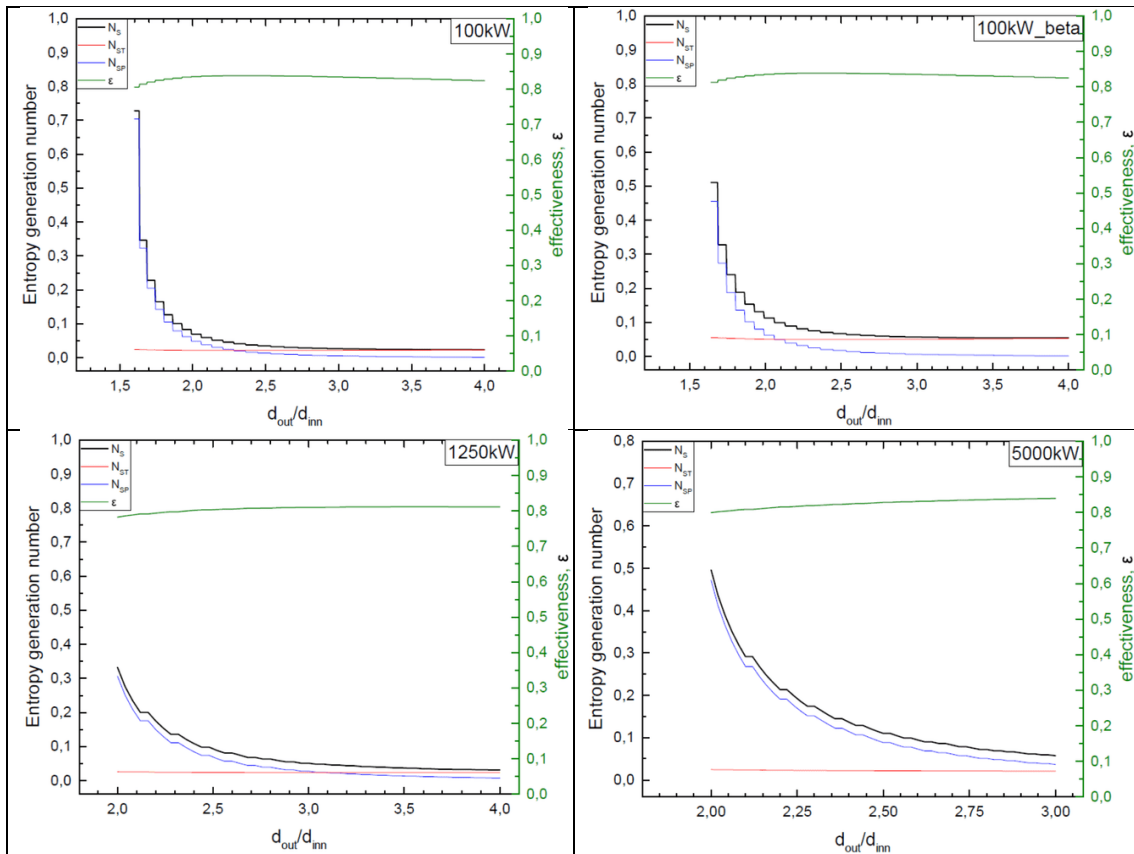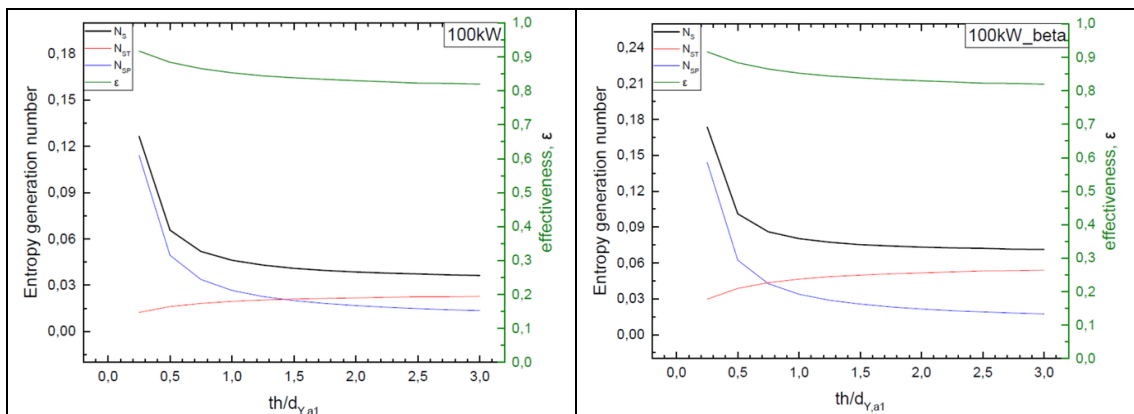
Figure 4.21 – The effectiveness, total entropy generation rate, and pressure drop and heat transfer irreversibility with respect to the recuperator outer diameter.

Finally, the four and last optimization step evaluates the optimum unitary cell length to be used in the recuperator core. This variable corresponds to the plate thickness of the plates X and Y of the recuperator core. As shown in Fig. 4.22, very short unitary cell lengths increase the number of flow interruptions, promoting turbulence, which aids the thermal exchange and consequently reduces the thermal entropy generation rate. In the other hand, the interruptions also cause high pressure drop entropy generation. The effectiveness of the exchanger, as well as heat transfer, is also favored with increasing flow interruptions. This step also does not present an optimal design point. However, it suggests a minimum plate thickness to be used to not over increase the pressure drop irreversibility. As observed, each case study presents a preferable unitary cell length, which depends on the boundary conditions. The 5000KW recuperator requires longer unitary cell lengths to control the pressure drop irreversibility, while the thinner plates seem to be better for the smaller recuperators such as the 100KW_beta.
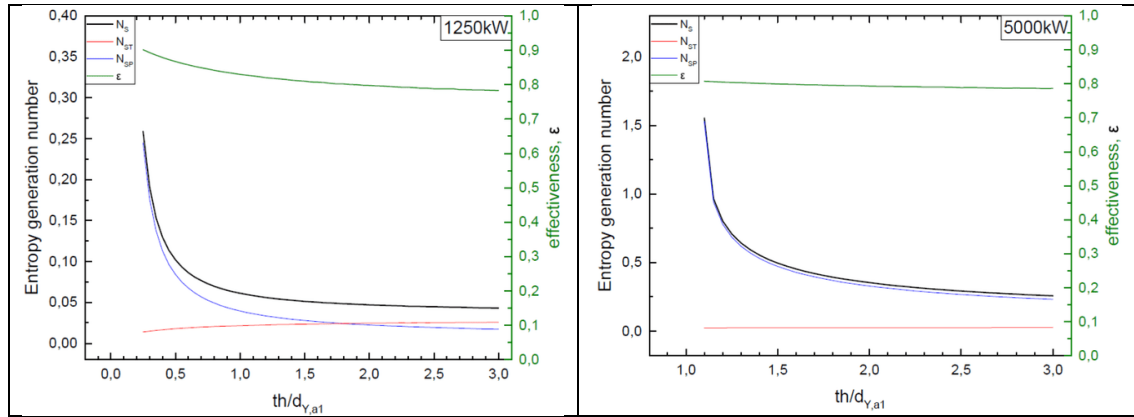
Figure 4.22 - The effectiveness, total entropy generation rate, and pressure drop and heat transfer irreversibility with respect to the recuperator unitary cell lengths.

4.5.7 Study cases recuperator results

Four study cases of wrap-around diffusion bonded recuperators, for 100kW (6.6 pressure ratio), 100KW (4.6 pressure ratio), 1250KW (6.6 pressure ratio) and 5000KW (6.6 pressure ratio) gas turbines, were designed with the interactive design code described in Section 4.3.7. The optimizable geometric aspects were defined by the minimum entropy generation analysis previously described. Table 4.7 shows the final main dimensions and the predicted effectiveness for each case. For the 100KW and 100KW_beta cases, two designs were made, for effectiveness of 80% and 90%. The terms $\overline{D_a}$ and $\overline{D_g}$ are the average hydraulic diameters of the air and gas sides, respectively.

Table 4.7 - Diffusion bonded recuperator dimensions and performance.

Recuperator Study cases		100 kW (ε=80%)	100 kW (ε=90%)	100 kW_β (ε=80%)	100 kW_β (ε=90%)	1250 kW (ε=70%)	5000 kW (ε=70%)
D_{in}	[m]	0.25	0.25	0.25	0.25	0.50	1.00
D_{out}	[m]	0.60	0.64	0.62	0.70	1.45	3.00
L_{core}	[m]	0.351	0.501	0.324	0.501	0.435	0.501
Δp_a	[%]	1.1	1.4	1.1	1.3	1.3	1.1
Δp_g	[%]	2.8	3.9	3.5	3.9	4.0	3.6
ε	[%]	80	89	80	89	70	68
$\overline{D_a}$	[mm]	2.2	1.8	2.9	2.2	3.9	4.8
$\overline{D_g}$	[mm]	7.3	5.9	7.0	5.3	13.5	15.6
th	[mm]	3	2	2	2	3	6

The recuperator study cases results, pressure drop, effectiveness and dimensions (volume), are compatible with the current recuperators applied in gas turbines. The diffusion bonded recuperator with cOSF heat transfer surface in the core can provide high effectiveness with low pressure drop with similar volume as the plate-fin recuperations in utilization today. Moreover, the present concept has several advantages and satisfies most of the short- and long-term requirements for gas turbines listed by Shah [5], showing to be a potential alternative for gas turbines. The recuperator concept advantages are listed in Table 4.8.

Table 4.8 - Diffusion bonded recuperator characteristics.

Performance	High recuperator effectiveness (> 90%) Low pressure loss (< 5%) Good part load performance
Surface geometry	cOSF surface geometry (no contact thermal resistance) High surface compactness Hi-efficiency fins Great thermal-hydraulic characteristics
Thermal effectiveness	The concept can provide an effectiveness up to 95%
Fabrication	Modular concept (ease manufacturing in comparison to the full recuperators). Continuous/automated fabrication process (the plates can be stamped). With the CAD machining methods, it is possible to faithfully reproduce the dimensions of the optimal design. Simple construction, the core has only two types of stamped stack plates. The module is formed by a stack of plates joined by diffusion bonding. Diffusion bonded (automated process robust and possible to manufacture several modules at the same time). Adaptable to high volume production methods.
Type of construction	Compact and light weight matrix. Integral manifolds/headers (no manifold flow distribution structure). Matrix envelope flexibility (annular).
Cost	Simple manufacturing parts (plate cutting or stamping). Minimum material waste, almost 100% utilization material. The diffusion bonding can produce several modules in just one run. Adaptable to bi-metallic construction; Is possible to use different materials trough the module (which would increase the component operation temperature without over increase the cost).
Integrity	Resistant to thermal cycling and fatigue failure (modular concept has lower thermal stress). Remain leak tight for engine life (the seals are replaceable).
Installation	Compact and light weight overall assembly. Eliminate inter-connecting ducts. Eliminate need for thermal expansion devices. The modules are fixed by a metal strip. The modules are assembled as bricks around the turbine.
Maintenance	Ease of recuperator removal/replacement. Plug-in matrix cartridge. Ease of leak detection testing. Ease of weld repair. Ease module replacement.

4.6 Conclusions and future works

A completely new concept of asymmetric wrap-around recuperator for gas turbines is proposed. The recuperator concept is modular, with the modules formed by a stack of machined plates joined by diffusion bonding. The modules contain air and gas cells with cOSF heat transfer surface in counter-flow configuration. A thermal hydrodynamic model is proposed to access the novel recuperator concept performance. A recuperator design code containing the mathematical model is also proposed to access the recuperator performance and design the component shape with minimum entropy generation rate. The mathematical modeling and the design code were validated in a numerical study using the software Fluent. First, the CFD adopted in the numerical study was validated with experimental data of the cOSF geometry to identify the mesh and the Fluent settings which provides the most accurate results. The simulations showed on average an error of 22.7% for pressure drop and 3.2% for heat transfer rate with the experimental data. In sequence, the CFD settings defined in the experimental/CFD study were used to simulate a slice of the recuperator with air at the heating and cooling condition. The simulations agreed with the design code output within an error of 11.9% for pressure drop and 0.9% for heat transfer rate. By using the entropy generation minimization method, four recuperators for different turbine sizes were designed aiming to identify trends and the "optimal" structure which provides the minimum thermodynamic irreversibility. The final design shows that the present concept can achieve high effectiveness $\left(\varepsilon \approx 0.9 \right)$ with contained pressure drop $\left(\Delta p_a \leq 1.5\%; \Delta p_g \leq 4.0\% \right)$ at a volume similar to the current recuperators present in the market. Moreover, the novel concept has some further advantages: Easy assembly; Easy maintenance; No channel clogging (communicating channels); No necessity of manifolds (the flow is self-distributed by the communicating cOSF channels); High thermal fatigue resistance; High pressure robustness (the turbine cycle pressure can be increased); High temperature capability. The turbine temperature can be increased by using different materials through the recuperator core; The recuperator is suitable to be produced in series. Thus, an alternative recuperator concept is proposed, and its performance prediction shows it has great potential to be applied in the microturbines market.

The future works should evaluate the manufacturing parameters in order to identify the limits of each constructional variable, such as the minimum wall thickness and the minimum channel spacing. A recuperator module should be manufactured and tested to compare the experimental data with the proposed mathematical model. A structural and thermal resistance evaluation should be done in the component to access its robustness and lifetime.

4.7 References

[1] McDonald, C. F. (1996). A Review on Heat Recovery Exchangers for Very Small Engines. International Journal of Turbo and Jet Engines, 13(4). doi:10.1515/tjj.1996.13.4.239

[2] McDonald, C. F. (1999). Emergence of Recuperated Gas Turbines for Power Generation. Volume 2: Coal, Biomass and Alternative Fuels; Combustion and Fuels; Oil and Gas Applications; Cycle Innovations. doi:10.1115/99-gt-067

[3] Kang et al., recuperator assembly and procedures, US Patent No. US 7,415,764 B2, Aug. 26, 2008.

[4] McDonald, C. F. (2003). Recuperator considerations for future higher efficiency microturbines. Applied Thermal Engineering, 23(12), 1463–1487. doi:10.1016/s1359-4311(03)00083-8

[5] Shah, R. K. Compact heat exchangers for microturbines. 2005.

[6] Kays, W. M., London, A. L., and Eckert, E. R. G. "Compact Heat Exchangers." ASME. J. Appl. Mech. June 1960; 27(2): 377. https://doi.org/10.1115/1.3644004

[7] Xiao, Gang, Tianfeng Yang, Huanlei Liu, Dong Ni, Mario Luigi Ferrari, Mingchun Li, Zhongyang Luo, Kefa Cen, and Mingjiang Ni. "Recuperators for micro gas turbines: A review." Applied Energy 197 (2017): 83-99.

[8] Do, K. H., Choi, B.-I., Han, Y.-S., & Kim, T. (2016). Experimental investigation on the pressure drop and heat transfer characteristics of a recuperator with offset strip fins for a micro gas turbine. International Journal of Heat and Mass Transfer, 103, 457–467. doi:10.1016/j.ijheatmasstransfer.

[9] Giugno, A., Cuneo, A., & Traverso, A. (2019). Analysis of uncertainties in compact plate-fin recuperators for microturbines. Applied Thermal Engineering, 150, 1243–1251. doi:10.1016/j.applthermaleng.2019

[10]   Treece, B., Vessa, P., & McKeirnan, R. (2002). Microturbine Recuperator Manufacturing and Operating Experience. Volume 1: Turbo Expo 2002. doi:10.1115/gt2002-30404

[11]   Kazakov, Nikolaĭ Fedotovich, ed. Diffusion bonding of materials. Elsevier, 2013.

[12]   Lepine, David. A brotherhood of canons serving God: English Secular cathedrals in the later Middle Ages. Boydell & Brewer Ltd, 1995.

[13]   Zhang Guoge, R. S. Chandel & H. P. Seow (2001) solid-state diffusion bonding of inconel alloy 718 to 17-4 ph stainless steel, Materials and Manufacturing Processes, 16:2, 265-279, DOI: 10.1081/AMP-100104305

[14]   Mott, Robert L.; Noor, Fatimah Mohd; Aziz, Azmahani Abdul. Applied fluid mechanics. 2006.

[15]   Cross, Hardy. Analysis of flow in networks of conduits or conductors. University of Illinois at Urbana Champaign, College of Engineering. Engineering Experiment Station., 1936.

[16]   Shah, Ramesh K., and Dusan P. Sekulic. Fundamentals of heat exchanger design. John Wiley & Sons, 2003.

[17]   Bejan, Adrian, and Allan D. Kraus, eds. Heat transfer handbook. Vol. 1. John Wiley & Sons, 2003.

[18]   Ordóñez, J.C. and Bejan, A., 2000. Entropy generation minimization in parallel-plates counterflow heat exchangers. International Journal of Energy Research, 24(10), pp.843-864. https://doi.org/10.1002/1099-114X(200008)24:10<843::AID-ER620>3.0.CO;2-M

[19]   Jeong, J. H., Kim, L. S., Lee, J. K., Ha, M. Y., Kim, K. S., & Ahn, Y. C. (2007). Review of Heat Exchanger Studies for High-Efficiency Gas Turbines. Volume 4: Turbo Expo 2007, Parts A and B. doi:10.1115/gt2007-28071

[20]   Pua, L. M., & Rumbold, S. O. (2003). Industrial Microchannel Devices: Where Are We Today? 1st International Conference on Microchannels and Minichannels. doi:10.1115/icmm2003-1101

5. Conclusion

In this thesis a novel recuperator for gas turbines is proposed, including the manufacturing method, component assembly in the turbine and the heat transfer surface used in its core.

In the first part, an experimental procedure is proposed to determine the heat transfer characteristics of unknown heat transfer surfaces for heat exchanger core application. Two well-known heat transfer surfaces, round tubes, and square cross-sectional channels were tested in the setup to validate the procedure. The obtained experimental data agreed well with the literature correlations of such geometries, with an average deviation within 15%, allowing to use the method to characterize the novel suggested heat transfer surface for the recuperator core application.

Using the procedure defined in Chapter 2, a novel heat transfer surface for heat exchangers was investigated. The novel geometry is based in the offset strip fins (OSF), where the main difference is the channels shape, which are circular instead of rectangular, being named as circular offset strip fins (cOSF). Five heat exchanger cores containing the proposed geometry were tested and the data were used to devise the cOSF heat transfer and pressure drop correlations. The Colburn factor j and Fanning friction f are valid for the range of $500 < Re_{Dh} < 3000$, within an error of 6% and 8%, respectively.

Finally, in the last chapter of the thesis, the axisymmetric diffusion bonding recuperator is proposed. The component concept is fully described, including the manufacturing method, assembly/sealing, and its characteristics dimensions. The cOSF correlations obtained in Chapter 3 were used in a mathematical model to predict the thermal hydraulic performance of the component. The model was validated with computational fluid dynamics simulations, which in turn were adjusted based on the cOSF cores experimental data. The mathematical model also includes the entropy generation minimization method to design the component dimensions which provide lower thermal-hydraulic irreversibility generation. Four diffusion bonded axisymmetric recuperators study cases for different turbine sizes were designed, showing that the present concept can achieve high effectiveness $\left(\varepsilon \approx 0.9\right)$ with contained pressure drop $\left(\Delta p_a \leq 1.5\%; \Delta p_g \leq 4.0\%\right)$ at a volume similar to the current recuperators present in the market. Moreover, the novel concept has some further advantages: Easy assembly; Easy maintenance; No channel clogging (communicating channels); No necessity of manifolds (the flow is self-distributed by the communicating cOSF channels); High thermal fatigue resistance (diffusion bonded part characteristic); High pressure robustness (the turbine cycle pressure can be increased); High temperature capability. The turbine temperature can be increased by using different materials through the recuperator core (bi-metallic approach); It can be produced in series (stamped plates). Hence, a completely new alternative recuperator concept is proposed, and its performance prediction shows it has a great potential to be applied in the microturbines market, due to its characteristics it suffices basically all the desired requirements of recuperators for gas turbines.